UC San Diego
UC San Diego Electronic Theses and Dissertations

Title
Distortion of low-frequency acoustic signals by interaction with the moving ocean surface

Permalink
https://escholarship.org/uc/item/8sd2n1pn

Author
Lynch, Stephen Dennis

Publication Date
2008

Peer reviewed|Thesis/dissertation

eScholarship.org
Powered by the California Digital Library
University of California

UNIVERSITY OF CALIFORNIA, SAN DIEGO

Distortion of low-frequency acoustic signals by interaction with the moving ocean surface

A dissertation submitted in partial satisfaction of the
requirements for the degree
Doctor of Philosophy

in

Oceanography

by

Stephen Dennis Lynch

Committee in charge:

Professor Gerald L. D'Spain, Chair
Professor Michael J. Buckingham
Professor William Coles
Professor Peter J.S. Franks
Professor William A. Kuperman
Professor Robert Pinkel

2008

Copyright
Stephen Dennis Lynch, 2008
All rights reserved.

The dissertation of Stephen Dennis Lynch is approved, and it is acceptable in quality and form for publication on microfilm:

Chair

University of California, San Diego

2008

DEDICATION

To Dad.

EPIGRAPH

Beware of the man who works hard to learn something, learns it, and finds himself no wiser than before... He is full of murderous resentment of people who are ignorant without having come by their ignorance the hard way.

—Kurt Vonnegut

TABLE OF CONTENTS

LIST OF FIGURES

LIST OF TABLES

ACKNOWLEDGEMENTS

I would like to thank my committee. Thanks also to Heidi Batchelor, Dave Ensberg, Galina Rovner, Pam Scott, Jeff Skinner, and the principal investigators of the ABM program: Grant B. Deane, Leroy M. Dorman, William A. Gaines, William S. Hodgkiss, W. Kendall Melville, and Eric Terrill. And thanks to the Coastal Data Information Program.

Chapter 3 was submitted for publication in the Journal of the Acoustical Society of America in July 2008. The title of the submitted manuscript is “Temporal variability of narrowband tones in a very shallow coastal waveguide”, and the authors are Stephen D. Lynch, Gerald L. D’Spain and Michael J. Buckingham.

VITA

2001	B. S. in Physics, University of California - San Diego
2001	B. A. in Mathematics / Applied Science, University of California - San Diego
2001-2008	Graduate Research Assistant, University of California - San Diego
2008	Ph.D. in Oceanography, University of California - San Diego

PUBLICATIONS

M. H. Denton, M.F. Thomsen, H. Korth, S. Lynch, J.C. Zhang and M.W. Liemohn, “Bulk plasma properties at geosynchronous orbit”, *Journal of Geophysical Research*, **110**, 2005.

Dan Lubin, Stephen Lynch, Rory Clarke, Esther Morrow and Steven Hart Increasing reflectivity of the Antarctic ocean-atmosphere system, “Analysis of Total Ozone Mapping Spectrometer (TOMS) and passive microwave data for 1979 - 1994”, *Journal of Geophysical Research*, **108**, 2004.

Gerald L. D’Spain, Eric Terrill, C. David Chadwell, Jerome A. Smith and Stephen D. Lynch, *Journal of the Acoustical Society of America*, **120**, “Active control of passive acoustic fields: Passive synthetic aperture/Doppler beamforming with data from an autonomous vehicle”, 2006.

PRESENTATIONS

Stephen D. Lynch, Gerald D’Spain and Eric Terrill, “Internal- and surface-wave-induced fluctuations and frequency spreading in shallow water acoustic propagation over short ranges”, *148th Meeting Acoustical Society of America*, San Diego, California, USA, 2004.

Stephen D. Lynch and Gerald D’Spain, “Temporal variability of narrowband tones in very shallow coastal waveguides”, *153rd Meeting Acoustical Society of America*, Salt Lake City, Utah, USA, 2007.

ABSTRACT OF THE DISSERTATION

Distortion of low-frequency acoustic signals by interaction with the moving ocean surface

by

Stephen Dennis Lynch
Doctor of Philosophy in Oceanography

University of California San Diego, 2008

Professor Gerald L. D'Spain, Chair

During multiple experiments in shallow water, low-frequency, narrowband acoustic tones were transmitted from stationary sources to hydrophone arrays about 1 km away. The spectrum of the received field depended strongly on ocean surface wave conditions. Doppler-shifted sidebands invariably are observed in the received spectra, with spectral content and levels depending on the prevailing ocean surface wave spectrum. Moreover, through the use of horizontal hydrophone arrays, the directionality of these scattered sidebands is also shown to depend on the directional surface wave spectrum. At times when the ocean surface waves were small, increased levels of higher order sidebands were observed.

First-order and higher-order perturbation theories based on normal mode propagation are explored in an effort to understand the observed dependence dependence on ocean surface waves. Bragg scattering from first-order perturbtation theory is shown to predict the deviations in angle of arrival of the scattered sidebands. Higher order perturbation is explored as a possible explanation of the higher order sidebands, but it is shown to be insufficient to predict all the features observed in the measured spectra. A simplified model is developed that reproduces the increased levels of the higher order scattering by modeling the the phase deviation that arises from path-length time-dependence caused by motion of the upper, reflective surface. This model is useful for predicting the effects of multiple

interactions with a moving reflective ocean surface.

Chapter 1

Introduction

1.1 A moving upper boundary in ocean acoustics

The study of ocean acoustics is made simulataneously complicated and interesting by the fluctuation of propagation characteristics over a wide range of temporal and spatial scales. Temporal variability in the propagation environment can distort the received acoustic field and create fundamental performance limits on acoustics-based communications or tomography systems. The relative importance of various sources of variability in the ocean on the received acoustic field is determined in part by the relative temporal and spatial scales of the ocean phenomena and the acoustic band of interest. Wave propagation theory links temporal frequency to spatial scales through the speed of propagation and dispersion relation, thereby linking the temporal and spatial scales of seemingly disparate phenomena. Perhaps more importantly, details of the acoustic propagation environment and relative arrangement of the acoustic instrumentation also determine what aspects of ocean variability will have the greatest effect on received acoustic fields. For example, in a deep ocean environment with a source and receiver deployed near the deep sound channel axis, ocean surface waves will have little impact on recorded signals while internal gravity waves and undersea currents will have a greater effect. Conversely, in a shallow environment with a well mixed water column, surface roughness and motion will play a significant role in distorting the received acoustic signal, while internal waves may be absent entirely.

During an experiment off the San Diego coast in 2001, low-frequency (< 1 kHz), narrowband acoustic tones were transmitted from a source deployed from R/V Acoustic Explorer to a 64-element hydrophone array deployed along an undersea ridge of nearly uniform depth (170 m) about 1 km away. The array's data were recorded by a computer aboard R/P FLIP, which was moored atop the same ridge. Though there was diverse instrumentation measuring environmental variability of many types – ocean surface waves, internal gravity waves, wind, temperature and salinity profiles – in the vicinity of the experiment, one of the greatest impacts on the measured acoustic signals was made by the ocean surface waves. Spectral analysis using long Fast Fourier Transforms (FFT's) of the pressure field recorded by the array reveals strong temporal variation of the received spectra. During a period of several hours, when measurements an Acoustic Doppler Current Profiler (ADCP) mounted below the surface on R/P FLIP's hull showed that a strong, 16-second period swell was propagating through the experiment site from the south (Fig. 1.1), the spectra of the received signals divided into multiple, distinct peaks centered about the original transmitted tone. During other times, when the surface wave conditions were different (Fig. 1.2), the received acoustic spectra changed accordingly (Fig. 1.3).

The acoustic environment during this experiment consisted of a uniformly shallow (~ 170 m) waveguide with a roughly 10 m thick warm, mixed layer over cooler water with a downward refracting sound speed profile. Ray- and normal mode-based models demonstrate that the multi-path nature of the waveguide included considerable interaction of the acoustic waves with the surface. While there is clear evidence that the surface waves greatly influenced the received acoustic spectrum, the experiment's execution was such that the influence of other factors (e.g., motion of the ship-suspended source) could not be ruled out, and more specific and detailed information about the acoustic waves' interaction with the moving surface was impossible to obtain. Nonetheless, these observations bring to question, Through what mechanisms do ocean surface waves influence low frequency acous-

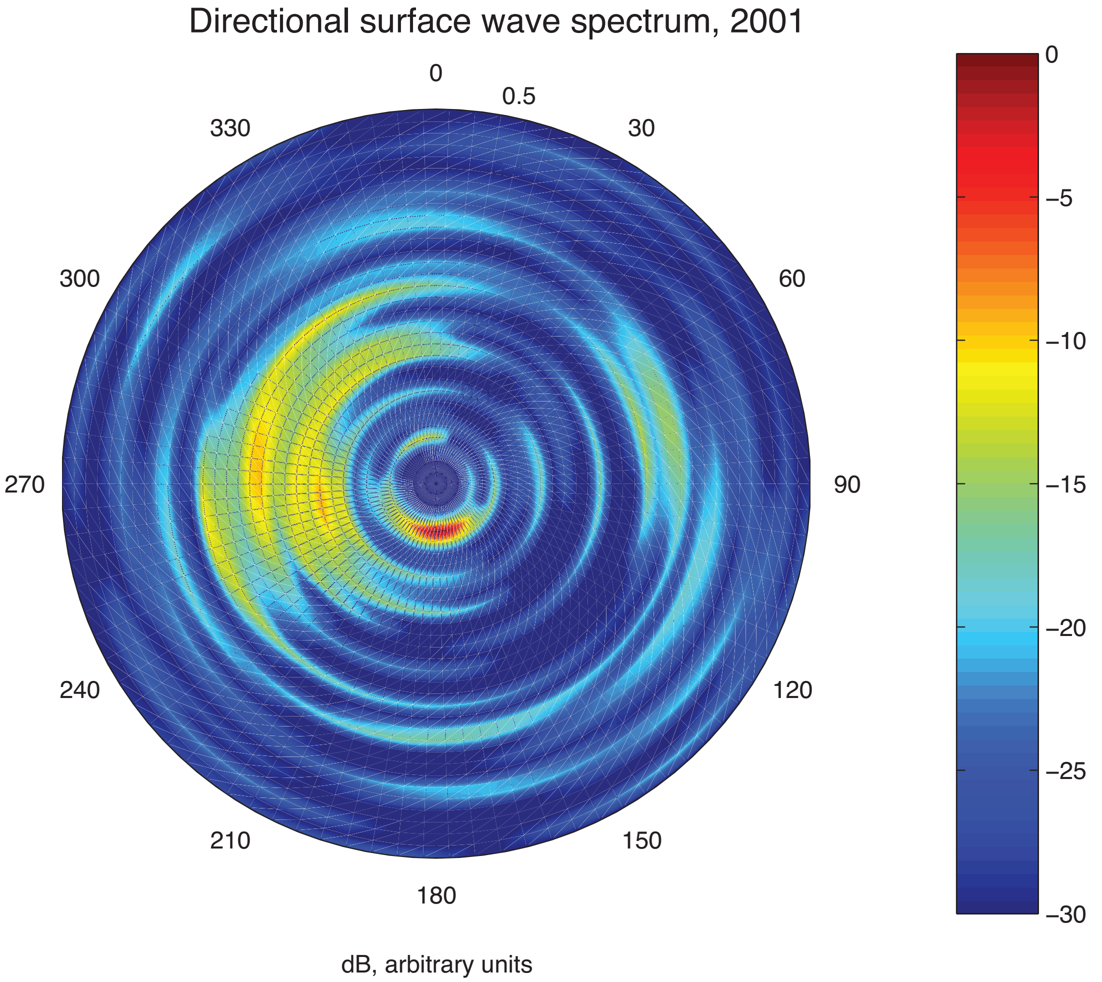

Figure 1.1: Measured surface wave directional spectrum during an experiment in 2001 off the coast of southern California using an ADCP. This spectrum was recorded at approximately hour 10 in Fig. 1.3. Frequency (0 to 0.5 Hz) and angle of origination are the radius and angle in this polar plot.

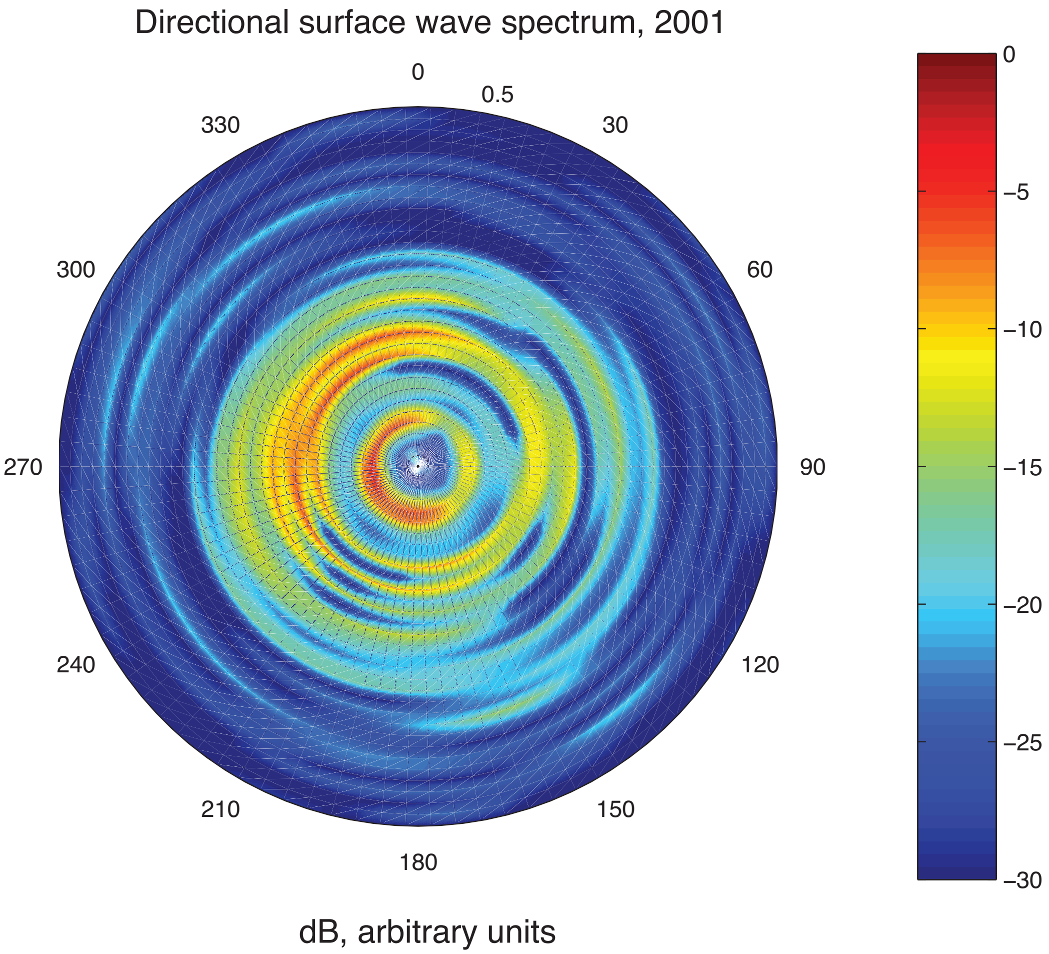

Figure 1.2: Measured surface waves during an experiment in 2001 off the coast of southern California using an ADCP. This spectrum was recorded at approximately hour 18 in Fig. 1.3. Frequency (0 to 0.5 Hz) and angle of origination are the radius and angle in this polar plot.

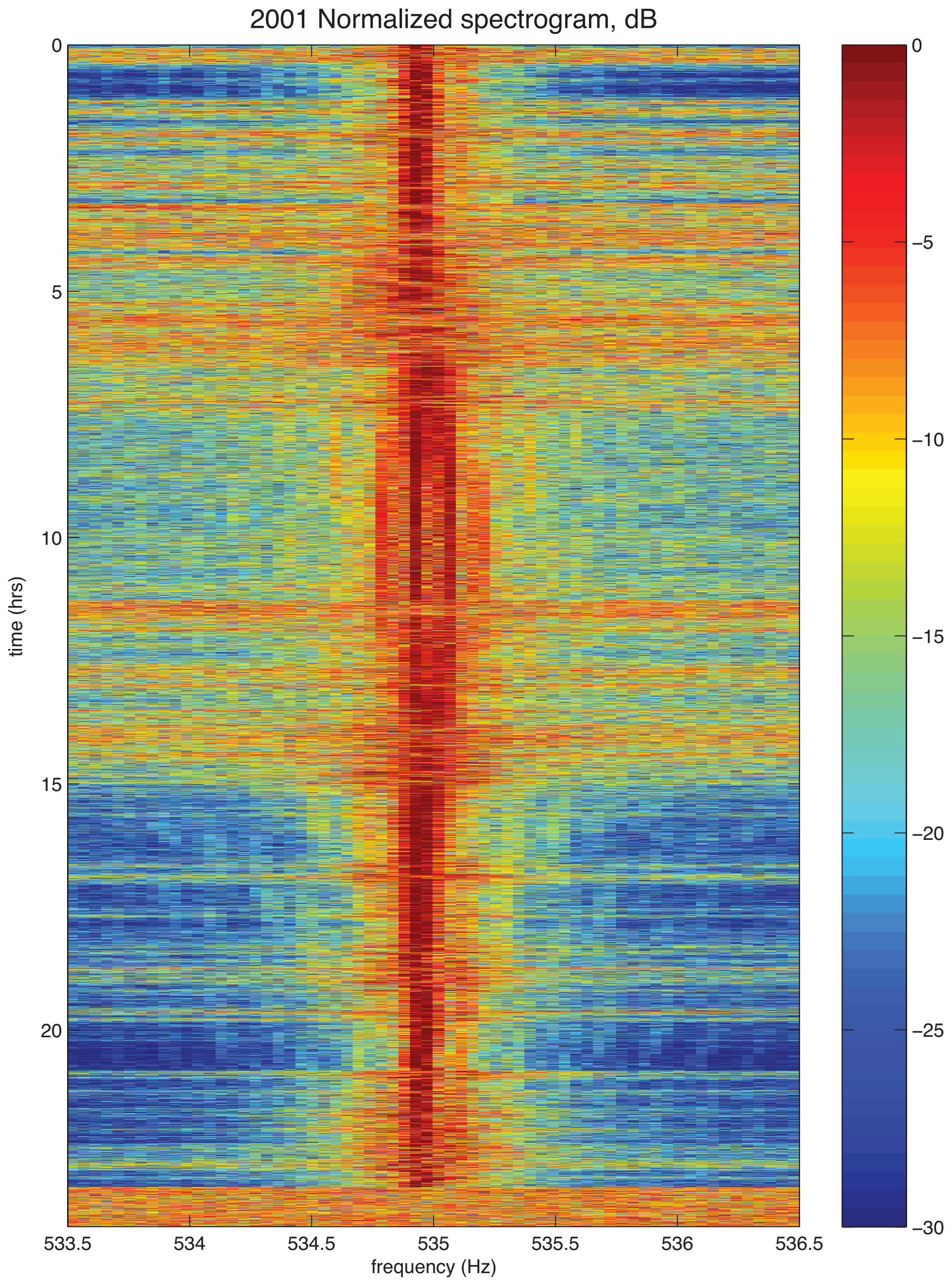

Figure 1.3: Measured spectrum over 24 hours at 535 Hz (one of 7 narrowband tones transmitted) during an experiment in 2001 off the coast of southern California. The surface wave spectra in Figs. 1.1 and 1.2 were recorded at hours 10 and 18, respectively.

Figure 1.4: The coast off Camp Pendleton Marine Corps Base, north of San Diego, where the 1996 experiment was conducted. The bottom point of the red triangle denotes the location of the acoustic source.

tic propagation, and how can surface waves lead to such strongly varying received acoustic spectra when viewed at extremely high spatial- and frequency-resolution? To this end, this work is devoted to the investigation of the mechanisms by which ocean surface waves distort propagating acoustic signals, and what the observed effects will be.

Given the limitations of the experiment conducted in 2001, the remainder of this study focuses on data that originated from an experiment that took place in 1996. This experiment was conducted just outside the surf zone off the coast off Camp Pendleton Marine Corps Base in southern California (Fig. 1.4). The water depth at the experiment site was uniform (approximately 10 m), and the sound speed was constant throughout the water column (1510 m s^{-1}). Whereas in the 2001

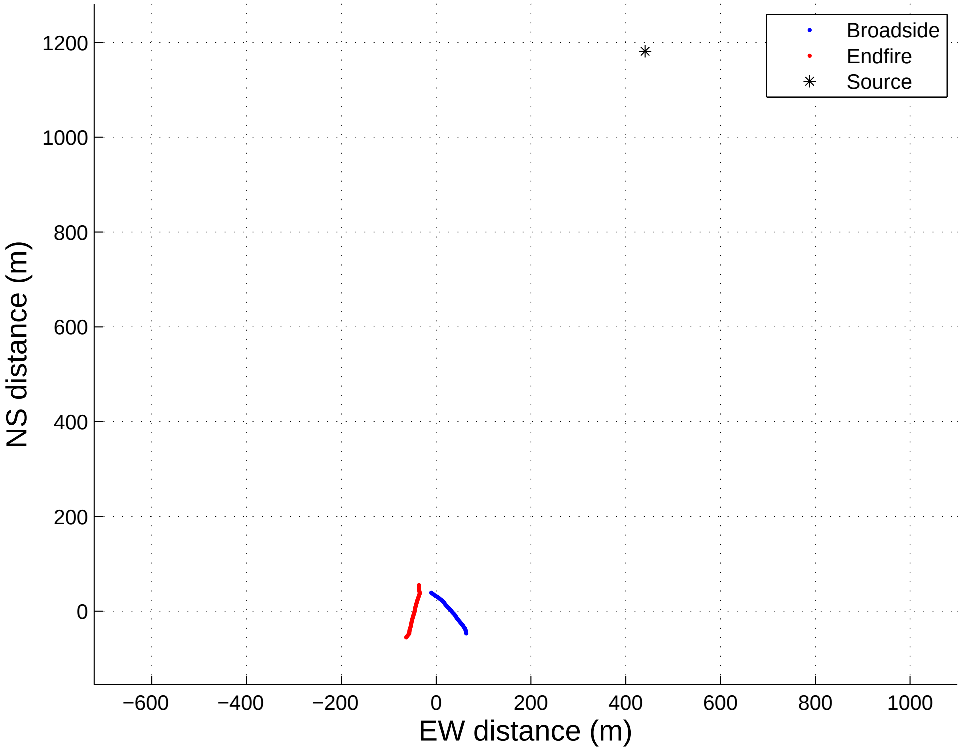

Figure 1.5: The hydrophone array and acoustic source configuration during the experiment conducted in 1996.

experiment the acoustic source was deployed from a surface ship, during the 1996 experiment the source was moored on the bottom, and was thus truly stationary. The two hydrophone arrays deployed in this experiment consisted of 64 elements each, with 1.875 m inter-element spacing. The arrays were each deployed in a roughly linear configuration on the bottom, with one oriented roughly broadside and the other roughly endfire to the acoustic source, which was approximately 1.25 km away (Fig. 1.5). Additionally, surface wave measurements were obtained throughout the 1996 experiment using both a pressure sensor array deployed and maintained by the Coastal Data Information Program (CDIP), and a pressure and 2 horizontal water velocity component (PUV) sensor deployed approximately 200 m away from the source. More detailed information of the experiment configuration and data follow in Chapters 2 and 3.

1.2 Expanding on the Doppler shift problem

The observed acoustic spectra recorded in the 2001 experiment clearly varied significantly in their frequency content in response to the changing ocean surface wave conditions. Moreover, given the shallow and isospeed character of the 1996 experiment, mechanisms by which the surface waves impart the Doppler shift on the propagating acoustic waves are explored in this investigation. A common example of Doppler shift is the observed change in pitch of an approaching ambulance's siren, in which a stationary observer hears the siren's frequency drop as the ambulance passes. The motion of the ambulance causes the acoustic path between the ambulance and observer to change in time, with the ambulance's advancement causing an up-shift in frequency through a shortening of the acoustic path, and the ambulance's retreat causing a down-shift in frequency through a lengthening of the acoustic path.

The Doppler shift has been implemented extensively at high frequencies (> 2 kHz) as part of many ocean acoustic tools for investigating properties of the ocean and for undersea navigation. Acoustic Doppler velocimeters (ADV) are a large variety of monostatic sonar tool that employ range gating on received echoes off scatterers suspended in the water column or at the surface to measure the one component of fluid motion over a range of radial distances from the instrument. The Doppler shift of these signal returns contains information about the velocity of the fluid volume, given certain assumptions about local sound propagation characteristics. These ADV instruments and concepts have been employed extensively in myriad configurations in physical oceanography to investigate surface waves, internal waves, turbulence and larger scale currents[VT98]. Typically they are configured with multiple transducers projecting pencil-beams in different, known directions.

A variation on the ADV concept is the phased-array Doppler sonar system (PADS). PADS systems use curved arrays of transducers to project fans of beams, using relative phasing of the individual transducers to shape and steer the beam. While the ranges of these instruments are much shorter than those of the more typical ADV's, their spatial coverage and high sampling rates (pulses every 0.5 s) allow for high resolution wavenumber-frequency decomposition of the measured velocity field, especially when 2 instruments are used in together, separated slightly in space[Smi02]. In this case, fully 3-dimensional, high-resolution wavenumber decompositions of the velocity field are possible. PADS systems have been employed to study internal and surface wave fields, turbulence, and various aspects of near-shore dynamics[Smi08], among other oceanographic phenomena.

A Doppler velocity log (DVL) turns the problem around, and uses velocities inferred from Doppler-shifted returns from a static surface or scatterer to measure the motion of the platform on which the DVL instrument is mounted. Rather than measuring the velocity of a volume of water over a range, DVL's typically measure the velocity of a single scatterer at a single distance using the Doppler shift. With an initial coordinate fix and a record of motion obtained from integrating a time-series of velocities relative to the sea floor obtained using a DVL, a submarine or underwater autonomous vehicle (AUV) can confidently keep track of its position without continuous surface contact [WYS99].

The Doppler shift has been integrated as part of a useful set of acoustics-based tools at lower frequencies, as well. Matched Field Processing (MFP) is a method of doing the inverse problem in acoustics, wherein a propagation model's parameter space is searched for the best fit to measurements. While this process typically requires extensive, accurate, *a priori* knowledge of the acoustic environment for the numerical model, it has been implemented with some success using data-derived normal modes[HHK01]. Using a formulation for Doppler shifted normal modes[SK94], it has been proposed to utilize the Doppler shift as a tool to separate and extract normal modes (depth functions) in a shallow waveguide[WRK07], which would be useful in data-derived MFP.

There is tremendous interest in knowing the acoustic properties such as shear and compressional sound speeds and attenuation of sediments and other seafloor and sub-bottom materials. While efforts to investigate the properties of sediments at higher frequencies ($>$ 2 kHz) using time-of-flight and amplitude measurements between a source and receiver have been largely successful, low frequency investigations are complicated by the need to have greater distances between the source and receiver, and the greater distances introduce complications related to inhomogeneities in the sediments [BGSH02]. However, the Doppler shift offers the opportunity to investigate the desired sediment properties using only a single hydrophone buried in the sediments, and a moving sound source. The problem of low-frequency sediment wave properties is difficult because the Doppler shift is proportional to both the acoustic frequency and the Mach number (the ratio of the source or receiver motion to the sound speed in the medium). High sound speeds in the ocean and bottom environments require large source speeds to engender a Doppler effect sufficiently large to be useful for investigation of these bottom properties. Investigations of sediment acoustic properties using the Doppler shift have been successfully implemented using as a sound source the propeller noise from an aircraft flying over the water[BGSH02].

If the example of the Doppler shift described above is expanded to include a frequency shift of waves due to a time-dependence of the propagation time between two points, then several other examples warrant mentioning, including some examples where fluctuations in the propagation medium itself induce frequency distortions in the propagating waves. Temporal frequency broadening has been observed in shear spectra in the upper ocean, and the phenomena is attributed to modulation by time-dependent background currents such as tides and inertial waves [Pin08].

All of the examples of Doppler shift so far have involved waves that are tied to their propagation medium. Environmental fluctuations have given rise to observable frequency distortions of electromagnetic waves, as well. Frequency distortions of inter-planetary electromagnetic radiation have been attributed to spatial variations in solar wind that advect through the path between an electromagnetic source and receiver. Amplitude modulations result from time-dependent refraction, which can be formulated as a Doppler shift due to time-dependence of the ray paths between source and receiver. These fluctuations have been used to ascertain properties of the solar wind [Col78].

Some of these examples, while not strictly related to acoustics, are worth mentioning because of the aspect of fluctuations giving rise to signal distortions, much like in the 2001 experiment. And, similar to the 2001 experiment, an important factor is the mechanism(s) by which the medium causes the distortion. In these cases, however, in contrast to those occurrences of the Doppler shift that become a deliberately integrated part of a tool, distortion of a signal by medium-induced Doppler shift has in the past been dubbed a ‘nuisance parameter’ of the received field [MWW95]. In the case of underwater acoustics, there are various mechanisms by which ocean surface waves can cause frequency distortions in received acoustic signals, and thus multiple ways that interaction with the moving surface will manifest in acoustic measurements, and discerning these is central to the work in this dissertation.

Time-dependent flow is known as potential mechanism for spectral distortion. This can be shown, for example, through a Lagrangian fluid mechanics approach to acoustic propagation [Sal98], or by the propagation of shocks through a flowing medium [Kor53]. Turbulence also affects sound propagation, and can lead to a refractive profile and even frequency distortion [DF98].

However, in a shallow waveguide, where multi-path propagation is prevalent, and the acoustic waves interact extensively with the ocean surface, distortions in the received acoustic field will be much more affected by surface interactions than by any volumetric mechanisms of distortion (except, perhaps, where there are bubbles involved). The focus of this work, then, is to explore the effects of acoustic interaction with a rough, moving surface.

The examples of Doppler-shifted, scattered acoustic waves mentioned so far have been primarily high-frequency, monostatic cases involving back-scatter of the acoustic waves. Pertinent to this study, however, is the bistatic case involving forward scattering from a rough, moving surface. Scattering from a rough surface is a problem that has been addressed extensively in a wide array of fields, including ocean acoustics, a number of fields involving electromagnetic waves, and others. While computational resources continue to improve rapidly, to address a realistic, fully 3-dimensional, fully time-dependent problem involving forward scattering of acoustic waves from a rough, moving surface nonetheless requires approximation methods, due to the numerical complexity inherent to such a problem [EG04].

Many such approximation methods have been developed across many disciplines. In ocean acoustics, the three most prevalent methods are small wave height perturbation, Kirchoff , and small slope approximations. The oldest and most commonly used method is the small wave height approximation, or small perturbation approximation. This method is most relevant to this study, and is developed more fully in Chapters 2 and 3. The basic premise of this method is to expand the wave field solution in a series whose terms are scaled by increasing orders of a small expansion parameter, which is related to the surface roughness height scaled by the acoustic wavelength (kh). The limitation of this method is obviously that it is only valid where the surface roughness is small compared to the acoustic wavelength.

Like the small wave height approximation method, the Kirchoff approximation, also known as the tangent plane approximation, is an older method of studying scattering of waves from a rough surface. The Kirchhoff method provides an approximation for the wave field on the rough surface that depends on the incident wave and the plane wave reflection coefficients. The scattering surface is assumed to be locally flat, and thus this method is limited to cases where the roughness is gently sloping [Ogi87, McD92]. The small slope approximation is an expansion of the wave field in a series of terms of increasing order of the roughness slopes, as the name implies. The main limitation of these methods is numerical complexity, which prevents the expansion past 2nd order in most cases. However, first- and second-order small slope approximations have been studied extensively[Ogi87, TB95]. These methods have all been employed extensively in the study of scattering off rough, static surfaces, for example (in ocean acoustics) scattering from a rough bottom or from a rough, icy surface[LS96]. In the case of a rough, moving surface, time-dependence must be included explicitly.

1.2.1 Outline of the dissertation

The main thrusts of this study are divided between Chapters 2 and 3. Chapter 2 focuses on observations of scattering in the vertical plane and compares these measurements to predictions from first-order perturbation theory. Scattering in a propagation environment involving strong multi-path character, and diversity in the ocean surface wave spectral and directional content are accounted for in the modeling. Chapter 3 examines scattering in the horizontal plane through first-order perturbational scattering theory. It then explores the effects of multiple interactions with a rough, moving sea surface through the development of a simplified model that approximates the acoustic frequency distortion as a phase deviation induced by reflection off a heaving, reflective surface. The predictions of this simple model are shown to agree quite well with observations in omnidirectional spectra. Higher order scattering from perturbation theory is presented, but it is shown that even higher order scattering cannot explain observed received acoustic fields when only one interaction with the sea surface is allowed in the modeling. A summary of the conclusions of this work, including statements of this work's contribution to ocean acoustics, is presented in Chapter 4. Additionally in Chapter 4, aspects of the relationship between acoustical and ocean surface waves that did not fit into the scope of this study and that are well worth being addressed in future investigative endeavors are proposed. In order to fully develop the ideas in these chapters, a strong foundation of acoustic wave equation solution techniques, ocean surface wave observation and analysis, and acoustic data processing concepts is required.

These topics are reviewed throughout the rest of this chapter, with emphasis placed on those methods that pertain directly to this study.

1.3 Foundations for studying ocean surface wave influence on acoustic propagation

Investigation of Doppler frequency spreading of acoustic signals through interaction with ocean surface waves requires a diverse set of tools. Time-dependent rough surface scattering of first- and higher-orders, and phase distortion by path-length modulation are all mechanisms by which received acoustic spectra can be affected by ocean surface waves. An analytical framework must be constructed to guide each numerical modeling or experimental data analysis effort. Outlined in this section are the basic foundation of ocean acoustics, ocean wave propagation, and digital array signal processing. Several of these ideas are expanded upon in subsequent chapters with extensions that lead to predictions of some of the phenomena observed in data, while others are employed in specific ways so as to illuminate certain aspects of the acoustic propagation or interaction with the ocean surface.

1.3.1 Acoustic propagation models

Acoustic propagation in the ocean is a challenging area of physics and efforts to address these challenges have progressed along several distinct avenues. For example several methods of describing acoustic propagation have been developed: ray and normal mode-based approaches, spectral methods and parabolic equation solutions. Because of the specific assumptions and mathematical approximations that are necessary to develop them, each method has its own set of strengths and weaknesses, and thus is appropriate to certain settings but not others. This study focuses on ray- and normal mode-based approaches to acoustic propagation.

Acoustic ray theory and computation

The acoustic ray method is similar to that used in optics in electromagnetic theory, in that the computed rays describe propagation paths, and as such are perpendicular to the iso-phase contours of the wave field. Development of rays in their basic form requires a "high frequency" approximation, and this requirement is one of the limits of ray theory, because it can lead to inaccuracies of predictions using the model. However, the computation time requried for ray models is generally considerably less than for other models [JKPS94], and the approach has the obvious advantage of presenting an intuitive picture of the propagation.

Acoustic rays are derived from the Fourier-transformed acoustic wave equation with delta function-forcing, or the Helmholz equation.

$$\bigtriangledown^2\widetilde{\psi}(\boldsymbol{x},\omega)+\frac{\omega^2}{c^2(\boldsymbol{x})}\widetilde{\psi}(\boldsymbol{x},\omega)=\delta(\boldsymbol{x}-\boldsymbol{x_\circ}) \tag{1.1}$$

where $\widetilde{\psi}$ is a scalar field, ω is temporal frequency, c is the sound speed, $\boldsymbol{x}$ and $\boldsymbol{x_\circ}$ are the receiver and source location vectors, respectively, and $\bigtriangledown^2$ is the Laplacian operator. The tilde will be used more extensively to denote transform pairs of functions, and in this case indicates the Fourier tranform of $\psi(\boldsymbol{x},t)$ into $\widetilde{\psi}(\boldsymbol{x},\omega)$. A series solution for $\widetilde{\psi}$ is proposed for Eq. 1.1:

$$\widetilde{\psi}(\boldsymbol{x},\omega)=e^{i\omega\tau(\boldsymbol{x})}\sum_{n=0}^{\infty}\frac{A_n(\boldsymbol{x})}{(i\omega)^n} \tag{1.2}$$

where τ is the travel time parameter, and describes the acoustic wavefronts.

The ray approximation for $\widetilde{\psi}$ (Eq. 1.2) is a high-frequency approximation, in that frequency ω must be sufficiently large for the higher-order terms in the ray series to vanish. Solution next involves computing derivatives with respect to $\boldsymbol{x}$ of $\widetilde{\psi}$ in terms of derivatives of the series terms in Eq. 1.2, and grouping by order of ω^{-n}. The resulting ω^2-ordered equation is called the Eikonal equation:

$$|\bigtriangledown\tau|^2=\frac{1}{c^2} \tag{1.3}$$

And the other ordered equations are known as the transport equations.

With the gradient of the wavefront function, Eq. 1.3 describes ray paths. Solution of the Eikonal equation involves parameterizing $\boldsymbol{x}$ in terms of a path length variable s so that

$$\frac{d\tau}{ds} = \frac{1}{c(s)} \tag{1.4}$$

In integral form this becomes

$$\tau = \int ds \, \frac{1}{c} \tag{1.5}$$

While the propagation paths are described by Eq. 1.3, the ray amplitudes are computed from the first transport equation:

$$2 \bigtriangledown \tau \cdot \bigtriangledown A_0 + (\bigtriangledown^2 \tau) A_0 = 0 \tag{1.6}$$

The solution to Eq. 1.6 accounts for geometrical spreading, $\sim \frac{1}{s}$, as well as refractive effects of the rays: the divergence of rays with similar take-off angles corresponds to lower amplitudes, and tightening of ray bundles corresponds to higher acoustic amplitudes.

In the time domain, the total pressure at a receiver is the summed contribution of many rays:

$$\psi(t) = \sum_{n=1}^{N_{rays}} A_n p(t - \tau_n) \tag{1.7}$$

where the travel times τ_n are given by the integral in Eq. 1.5 for each of the contributing arrivals. While computing ray paths over an arbitrary range given an initial angle for each is readily done using Snell's law, it is slightly trickier to compute rays that intersect two specific points. Such paths are often referred to as "eigenrays". Though their name may imply that they are related to eigenvalues of a matrix, and as such can be computed exactly and easily, the name is somewhat misleading. Eigenrays are found basically through a process of trial and error: a take-off angle whose ray comes close to intersecting the two points of interest is adjusted slightly until the desired tolerances are achieved.

Ray theory has been implemented numerically and extensively tested and benchmarked in several available numerical model packages, including CASS/GRAB [WK96]. The CASS/GRAB program is capable of incorporating environmental variability of many types, and outputting a wide range of quantities. For the purposes of this study, eigenrays are computed between a source and receiver for a shallow water environment, and their paths and relative amplitudes are input into numerical models developed in Chapter 3 to predict ocean surface wave-induced frequency distortions of propagating acoustic signals.

Normal mode theory and computation

Multiple approaches exist to model ocean acoustic propagation, and while these approaches are fundamentally different from one another, they also possess similarities. Without the ability to correctly predict basic phenomena, one theory would be quickly discarded. In this vein, normal mode and ray theories are equivalent: a family of rays can be computed that correspond to a given mode.

Normal mode theory is a far-field approximation, in that the continuous portion of the acoustic wavenumber spectrum, which decays rapidly and is not a significant contribution to the field far from the source, is neglected completely. While the earlier work in normal mode theory assumed range independence, modifications to the theory such as the adiabatic approximation, have reshaped the theory to address some cases of range dependence.

Normal mode theory applied to ocean waveguides describes the acoustic field in terms of a sum of vertical standing waves in the water column that propagate in range. The individual normal modes are subject to the upper and lower boundary conditions, such that the total summed acoustic field also satisfies the boundary conditions. This construction is similar to the modes of a vibrating guitar string, including the relative amplitudes' or excitiations' dependence on source and receiver location: strumming the guitar at one mode's null will result in little-to-no excitation of that mode. One key difference between the modes of the guitar and the ocean waveguide is that ocean acoustic modes can propagate an infinite distance in range whereas the guitar string is a medium that is finite in all 3 dimensions. This difference causes a discretization in the frequencies created by a guitar string through the dispersion relation ($\omega^2/c^2 = k_x^2 + k_y^2 + k_z^2$), where the wavenumbers of the guitar string are confined to a single dimension, whereas the continuum of frequencies can propagate in an ocean waveguide of infinite horizontal dimension.

Mode theory begins with the unforced version of the Helmholz equation in cylindrical geometry, with range-independent soundspeed $c(z)$ and density $\rho(z)$:

$$\frac{1}{r}\frac{\partial}{\partial r}(r\frac{\partial\widetilde{\psi}(\boldsymbol{x},\omega)}{\partial r}) + \rho(z)\frac{\partial}{\partial z}(\frac{1}{\rho(z)}\frac{\partial\widetilde{\psi}(\boldsymbol{x},\omega)}{\partial z}) + \frac{\omega^2}{c^2(z)}\widetilde{\psi}(\boldsymbol{x},\omega) = 0 \tag{1.8}$$

As before, $\widetilde{\psi}$ is a scalar function (pressure), with the tilde denoting the frequency domain. The spatial variables r and z ($\boldsymbol{x} = [r, z]$) are range and depth, respectively, and azimuthal symmetry is assumed.

Equation 1.8 can be solved using separation of variables:

$$\widetilde{\psi}(\boldsymbol{x},\omega) = \Phi(r,\omega)\Psi(z,\omega) \tag{1.9}$$

Substituting Eq. 1.9 into Eq. 1.8 and dividing through by $\widetilde{\psi}(\boldsymbol{x},\omega)$ results in

$$\frac{1}{\Phi}\frac{1}{r}\frac{\partial}{\partial r}(r\frac{\partial\Phi}{\partial r}) + \frac{1}{\Psi}\rho(z)\frac{\partial}{\partial z}(\frac{1}{\rho(z)}\frac{\partial\Psi}{\partial z}) + \frac{1}{\Psi}\frac{\omega^2}{c^2(z)}\Psi = 0 \tag{1.10}$$

The reasoning behind the separation of variables is that the first term in the unforced Helmholz equation involves only range, while the second term entirely pertains to depth. Thus, they must both be constant. This constant is designated $k_{m_r}^2$, and is the horizontal wavenumber corresponding to a mode function

$$\widetilde{\psi}_m(\boldsymbol{x},\omega) = \Phi_m(r,\omega)\Psi_m(z,\omega) \tag{1.11}$$

that satisfies Eq. 1.8 and the corresponding boundary conditions. Inserting $\widetilde{\psi}_m$ into Eq. 1.10, an eigenvalue problem is created:

$$\rho(z)\frac{d}{dz}\frac{1}{\rho(z)}\frac{d\Psi_m(z,\omega)}{dz} + [\frac{\omega^2}{c^2(z)} - k_{m_r}^2]\Psi_m(z,\omega) = 0 \tag{1.12}$$

The functions $\Psi_m(z,\omega)$ are orthonormal, with the normalization definition

$$\begin{aligned} \int_0^\infty dz\,\frac{1}{\rho(z)}\Psi_m(z,\omega)\Psi_n(z,\omega) &= 0,\ m \neq n \\ &= 1,\ m = n \end{aligned} \tag{1.13}$$

Any solution to a linear, second-order partial differential equation can be expressed as the sum of the general solution to the homogeneous (unforced) case, plus a specific solution to the inhomogeneous (forced) case. The general homogenous solution is the sum of linearly independent solutions. The issue of forcing (in acoustics, the presence of a source) is addressed by applying the solution Eq. 1.11 to the inhomogeneous Helmholz equation and applying orthonormality condition (Eq. 1.13).

$$\frac{1}{r}\frac{\partial}{\partial r}r\frac{\partial \Phi_m(r,\omega)}{\partial r} + k_{m_r}^2 \Phi_m(r,\omega) = -\frac{\delta(r)\Psi_m(z_s,\omega)}{2\pi r \rho(z_s)} \tag{1.14}$$

Here there is an acoustic source located at $r = 0$ and $z = z_s$, and azimuthal symmetry is assumed. The solution to Eq. 1.14 is well known:

$$\Phi_m(r,\omega) = \frac{i}{4\rho(z_s)}\Psi_m(z,\omega)H_0(k_{m_r}r) \tag{1.15}$$

where H_0 is the Hankel function of the first kind of order 0, and it has been assumed that as $r \to \infty$, all acoustic energy is outgoing. Equations 1.11 and 1.15 indicate that the received acoustic amplitude depends on modal excitation at both the source and receiver – if either one is located at a mode's null, that particular mode will be absent from the total received field.

Boundary conditions are a very important aspect of normal mode theory that has not yet been thoroughly discussed. Often the acoustic setting is such that the functions Ψ_m only exist between the surface ($z = 0$) and the ocean bottom $z = D$, and the integral in Eq. 1.13 is only computed over the interval $0 \le z \le D$. In general the upper boundary condition is defined as a "pressure release" boundary:

$$\widetilde{\psi}(z = 0, \omega) = 0 \tag{1.16}$$

This boundary condition is the same for all mode functions $\Psi_m(z,\omega)$, as well. In this thesis, the pressure-release aspect is always true, but in some cases the boundary itself is allowed to move, and this condition is therefore not true at $z = 0$. For example, in perturbation theory, which is addressed more fully in Chapters 3 and 2, the upper pressure release boundary is maintained through a Taylor approximation about $z = 0$. The bottom boundary condition is in general more complicated, even before boundary roughness is considered, and in fact there are many types of environments each with their own distinct boundary conditions. A half-space, or deep water approximation, is one where the bottom is taken at $z \to \infty$, but for the problem to be well behaved and physical, the acoustic pressure field must vanish at infinity: $\widetilde{\psi}(z \to \infty, \omega) = 0$.

In shallower waveguides with depth D, properties of the bottom determine the bottom boundary condition, which in turn affects the shape and even the number of normal modes. A "rigid" bottom allows no vertical fluid particle motion through it:

$$\frac{\partial}{\partial z}\widetilde{\psi}(z=D,\omega)=0 \tag{1.17}$$

In the case of the rigid bottom, the modes Ψ_m form a complete set, and the acoustic pressure field can be described completely in terms of them:

$$\widetilde{\psi}(\boldsymbol{x},\omega)=\sum_{m=1}^{\infty}\Phi_m(r,\omega)\Psi_m(z,\omega) \tag{1.18}$$

However, acoustic waveguides often have bottoms with boundary conditions such that the entire acoustic field cannot be described completely by the discrete sum of contributions as in Eq. 1.18, but rather includes a sum of finite discrete components, as well as a continuous spectral component. For such a waveguide with a source located at $\boldsymbol{x}_s=[0,z_s]$, the received pressure field at $\boldsymbol{x}$ is

$$\widetilde{\psi}(\boldsymbol{x},\omega)=\sum_{m=1}^{N}\Phi_m(r,z_s,\omega)\Psi_m(z,\omega)+\int_{-\infty}^{\infty}d\zeta\,\bar{\Phi}(r,z_s,\zeta,\omega)\bar{\Psi}(z,\zeta,\omega) \tag{1.19}$$

Just as the functions making up the discrete portion of the total received field are, the continuous functions $\bar{\Psi}(z,\zeta,\omega)$ are also subject to an orthonormality condition:

$$\begin{aligned}\int_{-\infty}^{\infty}d\zeta\,\frac{1}{\rho(z)}\bar{\Psi}(z,\zeta,\omega),\,\bar{\Psi}(z,\zeta',\omega)&=0,\ \zeta\neq\zeta'\\ &=1,\ \zeta=\zeta'\end{aligned} \tag{1.20}$$

Since it is of concern primarily in the near field, in many cases the continuous portion of the received wavenumber spectrum can be neglected. Spectral methods of solving the wave equation incorporate the full wavenumber spectrum, and are equivalent to Eq. 1.19.

One limitation of normal mode methods involves accounting for range dependence. One practice is to compute modes at the source and receiver ranges, and assume that the propagation is "adiabatic" – that the energy in each mode remains in that mode. This technique works well for weakly range-dependent environments, but leads to discrepancies when, for instance, when coupling between modes is significant. In these cases parabolic equation solvers predict the acoustic field more reliably. Several numerical modeling packages are available that implement normal mode algorithms, such as KRAKEN, which is available freely online (http://oalib.hlsresearch.com/). It is important to have a solid grasp of normal mode theory in order to extend it into a regime with a moving, rough surface. The ability to describe the ocean surface wave effects on the propagating acoustic modes is a powerful tool for understanding acoustic and surface wave measurements, and even predict the relationships between the two.

1.3.2 Ocean surface wave propagation and measurement

Ocean surface gravity waves are important from the standpoint of acoustics research for many reasons, including, for example, the complicated processes of wave breaking and bubble entrainment[FDV01]. However, for the topics explored in this work, only the theory and measurements of linearly propagating waves are considered. Linear propagation theory assumes no rotation (i.e. Coriolis frequency is 0), time-independent vorticity, incompressibility, and a uniformly flat bottom (no nonlinear coupling through interactions with changes in bathymetry). There is also an amplitude restriction, in that surface displacement can be no greater in magnitude than the wavelength of the disturbance, and a band limitation, in that only those surface waves whose wavelengths are great enough to ignore surface tension effects are considered[Lig78].

Expressions for the horizontal velocity components of flow u and v induced by the passing surface waves can be written in terms of a scalar velocity potential A.

$$\boldsymbol{u}(\boldsymbol{x},t) = -\bigtriangledown A(\boldsymbol{x},t) \tag{1.21}$$

where $\boldsymbol{x} = [\boldsymbol{r}, z]$ is the 3-dimensional spatial coordinate vector defined under the ocean surface, and t is time, and $\bigtriangledown$ is the spatial gradient operator. The continuity equation for an incompressible fluid is $\bigtriangledown\cdot \boldsymbol{u} = 0$, where $\boldsymbol{u}$ is the fluid velocity, so that the propagating part of the velocity field is Laplace's equation:

$$\bigtriangledown^2 A = 0 \tag{1.22}$$

In linear ocean surface wave theory the solution to Eq. 1.22 is subject to the boundary conditions at the mean surface $z = 0$

$$\begin{aligned}\frac{\partial \eta}{\partial t} &= \frac{\partial A}{\partial z} \\ \frac{\partial A}{\partial t} &= -g\eta\end{aligned} \tag{1.23}$$

where η is the surface displacement and g is the gravitational constant. Linear ocean surface waves are dispersive – group speed is frequency dependent – because of a frequency dependence to the depth to which waves are felt. The dispersion relation for surface waves arises from the boundary conditions at the free surface and the bottom.

$$\sigma^2 = g\kappa \tanh(\kappa D) \tag{1.24}$$

where σ is the surface wave frequency, κ is the wavenumber magnitude, and D is the ocean depth.

The velocity potential $A(\boldsymbol{x}, t) = A_\circ \cosh(\kappa(D - z))e^{-i(\sigma t - \boldsymbol{\kappa}\cdot\boldsymbol{r})}$, where $A_\circ$ is the value of A at the mean surface ($z = 0$). In terms of the surface wave frequency σ, wavenumber κ and height $\eta_\circ$, and the ocean depth D, the horizontal component of the surface wave-induced flow is

$$\boldsymbol{u}_h(\boldsymbol{x}, t) = -\frac{\boldsymbol{\kappa}}{\kappa}\frac{\eta_\circ \sigma}{\sinh(\kappa D)} \cosh(\kappa(D - z))e^{-i(\sigma t - \boldsymbol{\kappa}\cdot\boldsymbol{r})} \tag{1.25}$$

The excess pressure under a propagating ocean surface wave (excluding the hydrostatic and atmospheric pressure contributions to the total pressure) can similarly be written in terms of the velocity potential.

$$p_e = -\rho\frac{\partial}{\partial t}A(\boldsymbol{x}, t) \tag{1.26}$$

which becomes

$$p_e = -\rho\eta_\circ g\frac{1}{\cosh(\kappa D)} \cosh(\kappa(D - z))e^{-i(\sigma t - \boldsymbol{\kappa}\cdot\boldsymbol{r})} \tag{1.27}$$

where the dispersion relation (Eq. 1.24) has been substituted in. The excess pressure p_e and surface wave-induced horizontal flow $\boldsymbol{u}_h$ then depend not only on the wave height, but also on the depth z of measurement and the frequency σ (or, equivalently, the wavenumber κ). While Eq. 1.27 excludes the hydrostatic and atmospheric pressures, the wave pressure sensor can be often be used to measure tidal fluctuations, as well as higher frequency surface movement.

While Eqs. 1.27 and 1.25 describe surface waves of a single amplitude, frequency and direction, real, linear surface wave fields will consist of a continuous spectrum in frequency, direction and amplitude, which often can be approximated as a sum of discrete components.

For most of this study, information about the temporal frequency and directional content of prevailing surface wave fields is needed, and two different sources of data are used. One of the most common measurement types is a simple pressure sensor, such as a piezo-electric device, deployed below the surface. By simple extension through Eq. 1.27, an array of pressure sensors can be used to get directional spectral measurements of surface waves, where the relative phase between sensors in the array gives the directionality of the surface waves. The Coastal Data Information Program (CDIP), has deployed and maintained several arrays of this type, and the processed data from these arrays are freely available from the CDIP website (http://cdip.ucsd.edu/). Fully processed pressure sensor array data were downloaded for this study. For a full description of processing techniques, the reader is referred to the CDIP website.

Alternatively, devices that can measure pressure and individual horizontal flow vector components (PUV) can be used to record directional spectral information for surface gravity wave fields. This type of measurement requires no spatial separation of the instruments. Equations 1.25 and 1.27 describe the relationship between the horizontal velocity components $u(\boldsymbol{x})$ and $v(\boldsymbol{x})$ and pressure $p(\boldsymbol{x})$.

Whereas the relative phase of individual spectral components across the pressure sensor array describes directionality of the surface wave field, the relative amplitudes (including sign) of the horizontal flow components and at each frequency of surface waves measured by a PUV sensor describes the direction of propagation, with the phase relationship of each component to the pressure breaking the ambiguity. After transformation into the frequency domain by the Fourier transform, the angle of propagation ϕ_w is computed from the cross-spectra of pressure with the orthogonal horizontal flow components:

$$\tan \phi_w(\sigma) = \frac{Re[\widetilde{p}(\sigma)\widetilde{u}^*(\sigma)]}{Re[\widetilde{p}(\sigma)\widetilde{v}^*(\sigma)]} \tag{1.28}$$

where $\widetilde{p}(\sigma)$, $\widetilde{u}(\sigma)$ and $\widetilde{v}(\sigma)$ are defined as the Fourier transforms of $p(t)$, $u(t)$ and $v(t)$, the pressure and East-West and North-South flow amplitudes, respectively, at temporal frequency σ. In Eq. 1.28 the phase $\widetilde{p}$ relative to the phases of the velocity components $\widetilde{u}$ and $\widetilde{v}$ is used to solve the 180° ambiguity.

In general, ocean surface waves are modeled as a random process. Therefore, in order to gain statistical reliability, long time series of p and $\boldsymbol{u}_h$ are recorded, and quantities of interest (η, ϕ_w) are computed multiple times for each frequency σ and wavenumber κ, and ensemble averages are computed. The PUV sensor that was deployed during the experiment of focus in this study was moored approximately 0.5 m above the bottom in 9 m of water, approximately 200 m away from the acoustic source. The data were recorded at 2 samples s^{-1} for 20 minutes continuously every hour throughout the experiment. Though the Nyquist frequency of the instrument was 1 sample s^{-1}, the data were low-pass filtered using a 4-pole Butterworth filter with a cut-off frequency of 0.5 samples s^{-1} to reduce instrument noise. This cutoff frequency coincides with the Nyquist frequency of the data obtained from CDIP, whose sensor array was recorded at 1 sample s^{-1}.

Other post processing done on the PUV surface wave data was designed to reduce the χ^2 bounds of the measured quantities. Each 20-minute recording was divided into approximately 40, 128-point, 50%-overlapping snapshots, and was windowed with a Kaiser-Bessel window ($\alpha = 2.5$) before being Fourier-transformed into the temporal frequency (σ) domain. The values ϕ_w (Eq. 1.28) are then computed for each logarithmically spaced frequency bin. Finally, ensemble averages of the surface wave height spectral density and direction across frequency bins are computed.

1.3.3 Digital array signal processing in acoustics

Given the emphasis on observation in this study, a full understanding of data analysis techniques is of vital importance. Many tools have been developed for discrete signal processing [JD90, Hay96, OS99], and the task of choosing the proper tool for a given application can be a daunting one. The data analysis issues involved with measurement of ocean surface waves is discussed in Sect. 1.3.2. Here, the issues of the analysis of acoustic hydrophone array data are presented. The analysis of the acoustic time series in this work falls into two general categories: incoherent and coherent processing. The difference between these two categories involves the discarding (incoherent) or inclusion (coherent) of relative phase information. Though more detailed information about specific processing methods is given in the subsequent chapters, an overview of the techniques employed and why these methods were chosen is outlined here.

Spectral estimations are computed using fast Fourier transforms (FFT's). The Fourier transform pair for well behaved functions $a(t), \widetilde{a}(\omega)$ is defined as

$$\begin{aligned} \widetilde{a}(\omega) &= \int_{-\infty}^{\infty} dt\, e^{-i\omega t} a(t) \\ a(t) &= \frac{1}{2\pi} \int_{-\infty}^{\infty} d\omega\, e^{i\omega t} \widetilde{a}(\omega) \end{aligned} \tag{1.29}$$

However, it is impossible to integrate over all time, so in practice a windowed approximation is made. Because of this windowing in the time domain, and since digital sampling results in discrete time series rather than continuous functions, summations are performed in place of integrals. For sampling frequency $f_s = 1/\Delta t$ and snapshot length N, the discrete Fourier transform pair $b(n), \widetilde{b}(m)$ is

$$\begin{aligned} \widetilde{b}(m) &= \sum_{n=0}^{N-1} e^{-i\frac{2\pi mn}{N}} b(n) \\ b(n) &= \frac{1}{N} \sum_{m=0}^{N-1} e^{i\frac{2\pi mn}{N}} \widetilde{b}(m) \end{aligned} \tag{1.30}$$

where N is the snapshot length[OS99]. Often a snapshot is zero-padded beyond the content of actual data. While this does not add any more information, nor increase the frequency resolution of the FFT, it does change the frequency bin size. Because the FFT requires considerably less computation time when it is being applied to a time series whose length is a power of 2, it is beneficial to zero-pad snapshots of arbitrary length N out to the nearest power of two.

The complex results of the FFT's are then multiplied by their complex conjugates and averaged together incoherently. Since multiplication in the frequency domain is the same as convolution in the time domain, this is equivalent to taking the Fourier Transform of the autocorrelation function, thus yielding the acoustic auto-spectrum. In some cases normalization may be implemented between the transform and the averaging, depending on the desired outcome. Incoherent processing produces results that can be thought of as omnidirectional, since relative phase at a given frequency will depend on hydrophone spacing and propagation properties, and discarding the phase information and averaging temporal spectra incoherently serves the purpose of examining only the mean temporal frequency content measured by the array.

Except where otherwise specified, temporal window functions (Kaiser-Bessel, $\alpha = 2.5$) are used for all spectral analysis, including in coherent processing (beamforming). Because such a window function "pinches" the ends of the snapshot and reduces the effective snapshot length, the main lobe width increases, resulting in coarser frequency resolution. However, sidelobes are reduced and inter-null spacing is altered, such that side-lobe leakage is reduced, especially for non-bin-centered signals [CZO87].

Since all the incoherent time series analysis performed in this study is "conventional", the frequency resolution is determined by the snapshot length: $\delta f \sim 1/T$. However, since the auto-spectral estimate is only an estimation of the true underlying spectrum, there is a trade-off between resolution and statistical variance. In general, the resolution needed is determined by independent phenomena – for example, in Chapter 3, the acoustic spectral resolution must be sufficiently fine to decipher ocean surface wave frequencies ~ 0.06 Hz – and the shortest possible snapshot that will allow for this type of resolution is chosen, so that as many snapshots as possible may be averaged together to reduce confidence intervals on the estimate.

Most of the acoustic transmissions made during the experiment on whose data this study is based were 5 minutes in duration, and 6, 50%-overlapping snapshots were extracted from these segments and averaged incoherently for the higher resolution portion of the study in Chapters 2 and 3. These incoherently averaged spectra for each hydrophone were then divided further into frequency bands centered on the 8 transmitted narrowband tones' frequencies (70, 95, 145, 195, 280, 370, 535 and 695 Hz). Each band was then normalized to the value of the peak at the center frequency in order to emphasize the relative sideband levels and discard waveguide-related amplitude effects. These normalized, averaged spectra for each hydrophone were then incoherently averaged across most of the hydrophones in the array. Hydrophones that recorded erratic or noisy data were omitted from analysis. Typically the number of hydrophones whose recordings were included in the analysis was about 60 for each of the two 64-element hydrophone arrays deployed in the experiment. Thus, the maximum number of snapshots included in any of the incoherent spectral estimates was potentially as many as 360. Given windowing and overlapping, the effective snapshot count was most likely reduced from this number by a factor of 0.98[Har78]. In any case, the 90% confidence intervals for any of the measured spectra were as small as 0.1 dB.

For the coherent processing – the beamforming – done in this study, on the other hand, data-adaptive techniques are employed, as well as the conventional approach. Beamforming is a method of searching through angles of arrival for the acoustic energy incident on the array by matching the data against a set of replica vectors. In this study, the replica vectors are computed assuming plane-wave propagation. While there are beamforming techniques that operate in the time domain as well as the frequency domain, the methods employed in Chapters 2 and 3 are narrowband frequency domain techniques. The conventional (Bartlett) beamformer is implemented at frequency ω as the multiplication of the steering or replica vector $\boldsymbol{d}(\theta, \omega)$, a column vector, with a data covariance matrix $R(\omega)$. The Bartlett beamformer output $b_B(\theta, \omega)$ for arrival angle θ at frequency ω is

$$b_B(\theta, \omega) = \boldsymbol{d}'(\theta, \omega) R(\omega) \boldsymbol{d}(\theta, \omega) \tag{1.31}$$

where the j^{th} element of $\boldsymbol{d}$ is $e^{i\boldsymbol{k}(\theta,\omega)\cdot\boldsymbol{x}_j}$, $\boldsymbol{x}_j$ is the location vector of the j^{th} hydrophone, and $\boldsymbol{k}(\theta, \omega)$ is the wavenumber vector for the plane wave with frequency ω arriving from angle θ, and $\boldsymbol{d}'$ is the conjugate transpose of $\boldsymbol{d}$. The magnitude of $\boldsymbol{k}(\theta, \omega)$ is related to frequency ω through the acoustic dispersion relation: $|\boldsymbol{k}| = \omega/c$.

The covariance matrix estimate $R(\omega)$ is computed from the outer product of the vector of complex values of the measured pressure field in the frequency domain. In conventional processing, R can be estimated from the FFT of a single snapshot in time across the hydrophone array, but since this results in a matrix of unity rank, any processing that will involve inversion of R will require at least as many independent snapshots in time as there are elements in $\boldsymbol{d}(\theta, \omega)$.

A data-adaptive beamformer works in the same basic way as the Bartlett beamformer, except that the steering vectors are weighted using information from the data, through some computation involving the covariance matrix R. The minimum variance, distortionless response (MVDR) beamformer is constrained to unity gain in the direction of the signal, and it seeks to minimize the output variance in all other directions. The result of this optimization problem is a weighted steering vector $\boldsymbol{w}(\theta, \omega)$:

$$\boldsymbol{w}(\theta, \omega) = \frac{R^{-1}(\omega)\boldsymbol{d}(\theta, \omega)}{\boldsymbol{d}'(\theta, \omega)R^{-1}(\theta)\boldsymbol{d}(\theta, \omega)} \tag{1.32}$$

Once the weighted replica vectors $\boldsymbol{w}(\theta, \omega)$ are computed, the MVDR beamformer output $b_{MVDR}(\theta, \omega)$ is found just the same way as the Bartlett beamformer:

$$b_{MVDR}(\theta, \omega) = \boldsymbol{w}'(\theta, \omega)R(\omega)\boldsymbol{w}(\theta, \omega) \tag{1.33}$$

As was mentioned, in order to invert $R(\omega)$ without any instability issues, it must be computed using at least as many statistically independent snapshots of the pressure field as there are hydrophones involved in the processing (which equals the dimension of $R(\omega)$). If the vector $\widetilde{\boldsymbol{z}}(m)$ is defined as the vector of the m^{th} bin of the FFT of a snapshot of the pressure time-series recorded on all hydrophones, then the covariance $\hat{R}(\omega)$ is estimated

$$\hat{R}(\omega_m) \simeq \langle \widetilde{\boldsymbol{z}}(m)\widetilde{\boldsymbol{z}}'(m) \rangle = \frac{1}{M}\sum_{l=1}^{M} \widetilde{\boldsymbol{z}}_l(m)\widetilde{\boldsymbol{z}}'_l(m) \tag{1.34}$$

where $\widetilde{\boldsymbol{z}}_l(m)$ is the FFT of the l^{th} snapshot, M is the number of hydrophones included in the search, $\omega_m = m\Delta\omega = 2\pi f_s/N$, N is the number of points in the snapshot and and f_s is the sampling frequency.

It is useful at this point to introduce the term “white noise gain” (WNG), which is mathematically defined as the square of the magnitude of the steering vector, and conceptually is a measure of the robustness of a processor to phase error, or mismatch. The white noise gain of the Bartlett beamformer G_B is independent of frequency or arrival angle, and depends only on the number of hydrophones M included in the beamformer processing:

$$\begin{aligned} G_B(\theta,\omega) =& \boldsymbol{d}'(\theta,\omega)\boldsymbol{d}(\theta,\omega) \\ =& M \end{aligned} \tag{1.35}$$

Similarly, the expression for the white noise gain G_{MVDR} for the MVDR processor is not so simple.

$$\begin{aligned} G_{MVDR} =& \boldsymbol{w}'(\theta,\omega)\boldsymbol{w}(\theta,\omega) \\ =& (\frac{R^{-1}(\omega)\boldsymbol{d}(\theta,\omega)}{\boldsymbol{d}'(\theta,\omega)R^{-1}(\theta)\boldsymbol{d}(\theta,\omega)})'(\frac{R^{-1}(\omega)\boldsymbol{d}(\theta,\omega)}{\boldsymbol{d}'(\theta,\omega)R^{-1}(\theta)\boldsymbol{d}(\theta,\omega)}) \end{aligned} \tag{1.36}$$

While the MVDR processor works extremely well for situations with large SNR at sharpening the beamformer's resolution so that it is considerably finer than the Bartlett beamformer, it is also extremely susceptible to errors. Phase discrepancies that may be the result of error in locations $\boldsymbol{x}_j$, error in sound speed estimation, or deviation from the plane wave assumption will quickly degrade the performance of the MVDR beamformer. Additionally, MVDR processing is prone to introduce bias into the results, not just degrade when there is mismatch in the input parameters. To account for this, several modifications have have been developed that make it a much more robust algorithm. Most common among these is the technique of "diagonal loading" of the covariance matrix, which increases stability for the inversion, and diminishes the effect of phase errors.

$$R_*(\omega) = R(\omega) + \gamma I \tag{1.37}$$

where γ is a constant and I is the identity matrix. The trick in this type of technique is to choose the appropriate level of diagonal loading, such that the high resolution properties of the data-adaptive technique remain intact, while some of the robustness of the Bartlett algorithm is gained.

The white noise constraint (WNC) beamforming algorithm is an attempt to do just that: to put bounds on the diagonal loading of the robust adaptive beamformer, measuring the WNG "on the fly" so that the best of both processing worlds is achieved. To accomplish this, the value of γ is chosen so that the WNG of the beamformer does not exceed a certain level, usually chosen in relation to G_B. For example, in many applications, the WNC is chosen such that the white noise constraint G_{WNC} does not exceed $10\log G_B - 3$ dB. Unfortunately, since this value depends largely on the covariance matrix R through its influence on the weighting vector, there is no analytical way to compute the appropriate value for γ, and it must be computed iteratively for every look direction θ and every frequency ω, using as a check the relative values of the white noise gain for the diagonal loaded beamformer and the specified WNG constraint. The weight vector $\boldsymbol{w}_W(\theta,\omega)$ for the WNC beamformer then becomes

$$\boldsymbol{w}_W(\theta,\omega) = \frac{R_*^{-1}(\omega)\boldsymbol{d}(\theta,\omega)}{\boldsymbol{d}'(\theta,\omega)R_*^{-1}(\theta)\boldsymbol{d}(\theta,\omega)} \tag{1.38}$$

and the WNC beamformer output is computed the same way as the Bartlett and MVDR beamformers.

$$b_{WNC} = \boldsymbol{w}'_W(\theta,\omega)R(\omega)\boldsymbol{w}_W(\theta,\omega) \tag{1.39}$$

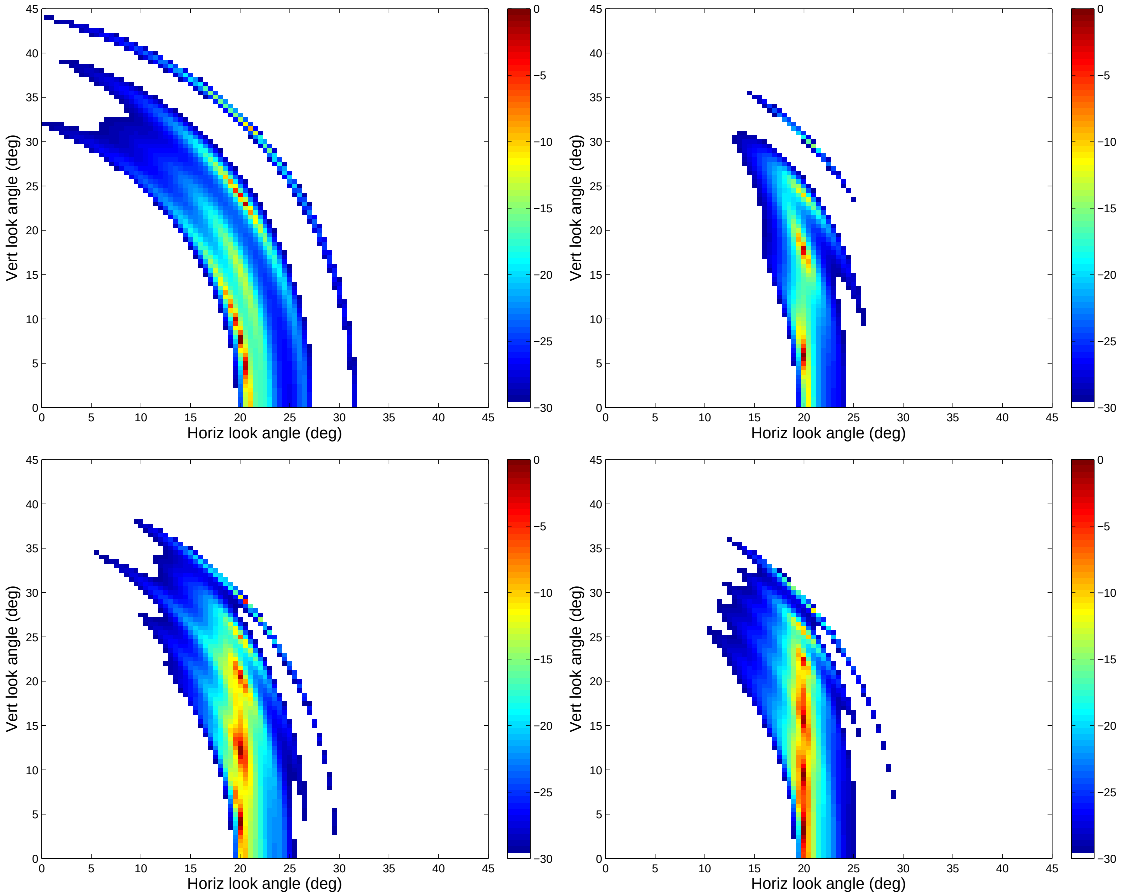

Figure 1.6: Narrowband beamformer search through azimuthal (horizontal axis) and vertical (vertical axis) for simulated multipath arrivals at 4 frequencies (clockwise from upper left: 280, 370, 695 and 535 Hz), with added uncorrelated noise. Beamformer algorithm uses white noise constraint of -3 dB.

Chapter 2

Evidence of Doppler-shifted Bragg scattering in the vertical plane from interaction with a rough, moving surface

2.1 Abstract

Vertical plane beamformer output for several received narrowband acoustic tones (280, 370, 535 and 695 Hz) shows evidence of Doppler-shifted Bragg scattering of the transmitted acoustic signal by the ocean surface waves. The received, scattered signal shows dependence on the ocean surface wave frequencies and wavenumber vectors, as well as on acoustic frequencies and acoustic mode wavenumbers. Sidebands in the beamformer output are offset in frequency by amounts corresponding to ocean surface wave frequencies, while deviations in vertical arrival angle agree with those predicted by the Bragg condition through first-order perturbation theory using measured directional surface wave spectra and acoustic modes measured by a horizontal hydrophone array on the ocean bottom.

2.2 Introduction

A common method of studying Doppler shifting and scattering of acoustic signals by ocean surface waves is to model the received omnidirectional spectrum, integrating the received signal over spatial frequency and studying only the temporal frequency deviations introduced through interaction with the moving surface[WJ93]. Studies of the directional characteristics of scattered acoustic signals often examine the phenomena in a 2-dimensional plane. Most commonly, scattering in the vertical plane has been examined numerically by limiting the problem to two dimensions, i.e. the surface waves are propagating in one direction along the vertical plane between the acoustic source and receiver(s)[WJ95].

Experimental results showing clear evidence of Doppler-shifted Bragg scattering by ocean surface waves are less common. Lebedev and Salin[LS04] and Lynch et al. [LBD08] successfully related measured horizontal beamformer output over a 1 Hz band centered on received, low-frequency ($f_\circ < 1500$ Hz) narrowband acoustic signals to measured ocean surface waves using first-order perturbation, verifying the Bragg condition in the horizontal plane. While several authors have used numerical models to predict the received pressure field resulting from scattering in the vertical plane from a moving surface[WJ95], few have presented similar measured results relating acoustic frequency and wavenumber deviations arising from interaction with ocean surface waves.

In this paper measurements are presented that show a clear dependence of acoustic frequency shift and vertical angle of arrival of scattered acoustic sidebands on measured surface wave frequencies and directions of surface wave propagation. These results were recorded using a stationary source and receiving hydrophone array during an experiment outside the surf zone off the southern California coast. Over the course of the experiment surface wave and tidal conditions varied, and this variability is reflected in the acoustic measurements. The relationship between the acoustic and environmental measurements is explained using first-order, time-dependent perturbational scattering theory and normal mode theory of acoustic propagation. This theory is coupled with measurements of the non-frequency shifted, non-scattered acoustic spatial spectrum to predict the angle deviations in the vertical plane and frequency shifts associated with the dominant frequencies and wavenumber vectors of the measured ocean surface waves. The acoustic spatial spectra are computed two ways: directly, from a Hankel transform pressure measurements spanning the entire array, and from vertical plane-wave beamformer output. Observed angle- and frequency- acoustic spectra show clear dependence of the scattered and Doppler-shifted pressure signal on the non-distorted acoustic modes, which agrees with perturbational scattering theory.

Most studies of Doppler-shifted Bragg scattering from a rough, moving ocean surface employ statistical models relating surface wave spectra to measured wind velocities[LS04, WJ95, Gra03, BT97]. This paper instead employs measured surface wave spectra. The reason for this approach is that the experiment site was too close to shore for the assumptions on which the surface wave models are typically based to be valid. The observed surface wave conditions changed significantly continously throughout the experiment, and these variations did not always correspond to changes in local wind.

In Sect. 2.3 measured, spatial acoustic spectra and beamformer results for two times during the study are presented, following a brief overview of the experiment site and instrument set-up. Horizontal acoustic mode numbers are inferred from the wavenumber spectra estimates and plane-wave vertical beamformer results at each of the transmitted acoustic frequencies. Predictions of Doppler-shifted scattering in the vertical plane using the measured acoustic mode numbers are compared to vertical beamformer output over a range of frequencies centered on the transmitted narrowband tones in Sect. 2.3.3. Section 2.4 contains a summary of acoustic normal mode propagation, including a derivation of the scattered modes and their dependence on the ocean surface waves using first-order perturbational theory, as well as estimation of acoustic wavenumber spectra using a spatially windowed Hankel transform. Finally, the implications of these measurements in the context of first-order scattering theory are discussed in the context of the possibility of using the results in this paper to invert received acoustic spectra for ocean surface wave directional spectra in Section 2.5.

2.3 Experiment and results

2.3.1 Instrumentation and processing methods

The experiment was conducted in a shallow (10 m), iso-speed (1510 m s^{-1}) waveguide. The low-frequency acoustic source was moored 0.5 m above the bottom approximately 500 m offshore, and transmitted narrow-band tones (280, 370, 535 and 695 Hz) for 5 minutes continuously every half-hour or hour to a hydrophone array whose data were digitized at 1500 samples s^{-1} per channel. The hydrophone array was deployed on the bottom approximately 1.25 km away from the source and 1.5 km offshore. The source was approximately 20° true bearing from the array. The array consisted of 64 hydrophones spaced 1.875 m apart, and was oriented roughly endfire to the source (Fig. 2.1). The sturdy mooring of the source and the partial burial of the hydrophone array under sediments deposited by ocean currents and surface waves at the beginning of the experiment ensured that both the source and receiving array were stationary throughout the experiment. All frequency shifts observed in the acoustic data can therefore be attributed to motions in the environment and not in the acoustic transmitting and recording system.

Data from an instrument measuring ambient pressure and two horizontal components of water velocity (PUV) deployed near the source were used to compute directional ocean surface wave spectra throughout the experiment (Fig. 2.2). Frequencies and wavenumber amplitudes for ocean surface waves are related through the dispersion relation for linear surface waves:

$$\sigma^2 = g\kappa \tanh(\kappa D) \tag{2.1}$$

where σ and κ are the ocean surface wave frequency (Hz) and wavenumber magnitude (rad m^{-1}), respectively, g is the gravitational constant (9.8 m s^{-2}), and D is the depth (m) of the ocean bottom. Directional spectral analysis of PUV data for surface waves, as implemented in this study, assumes that waves propagate from a single direction at each frequency. The PUV sensor recorded 2 samples s^{-1} per channel continuously for 20 minutes every hour throughout the experiment. Significant wave height H_s, defined as four times the square root of the variance

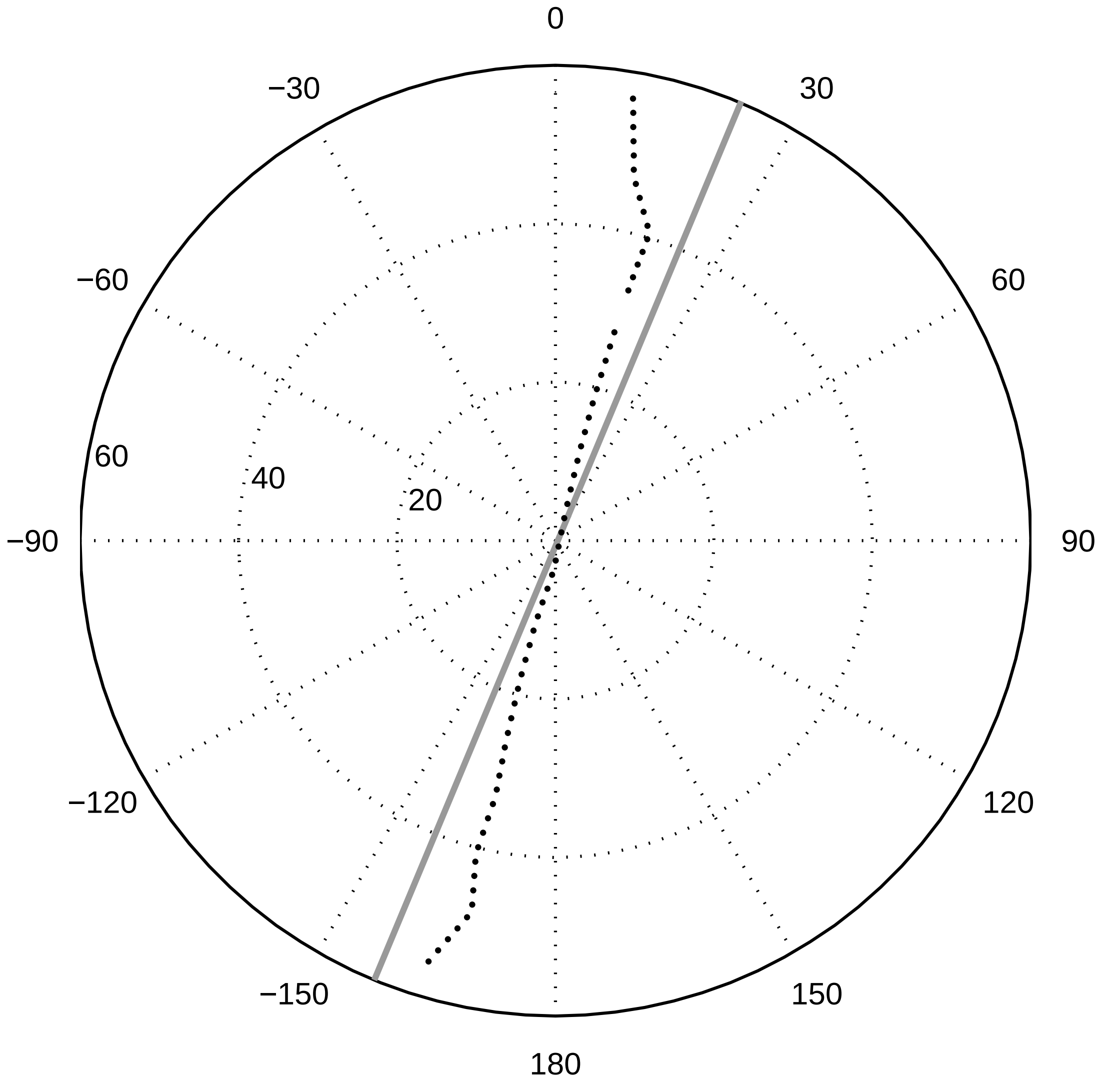

Figure 2.1: Geometry of the horizontal hydrophone array. The solid line through the origin and 20° marks the direction towards the source. While the whole array consisted of 64 elements, only those 61 that operated reliably throughout the experiment are depicted.

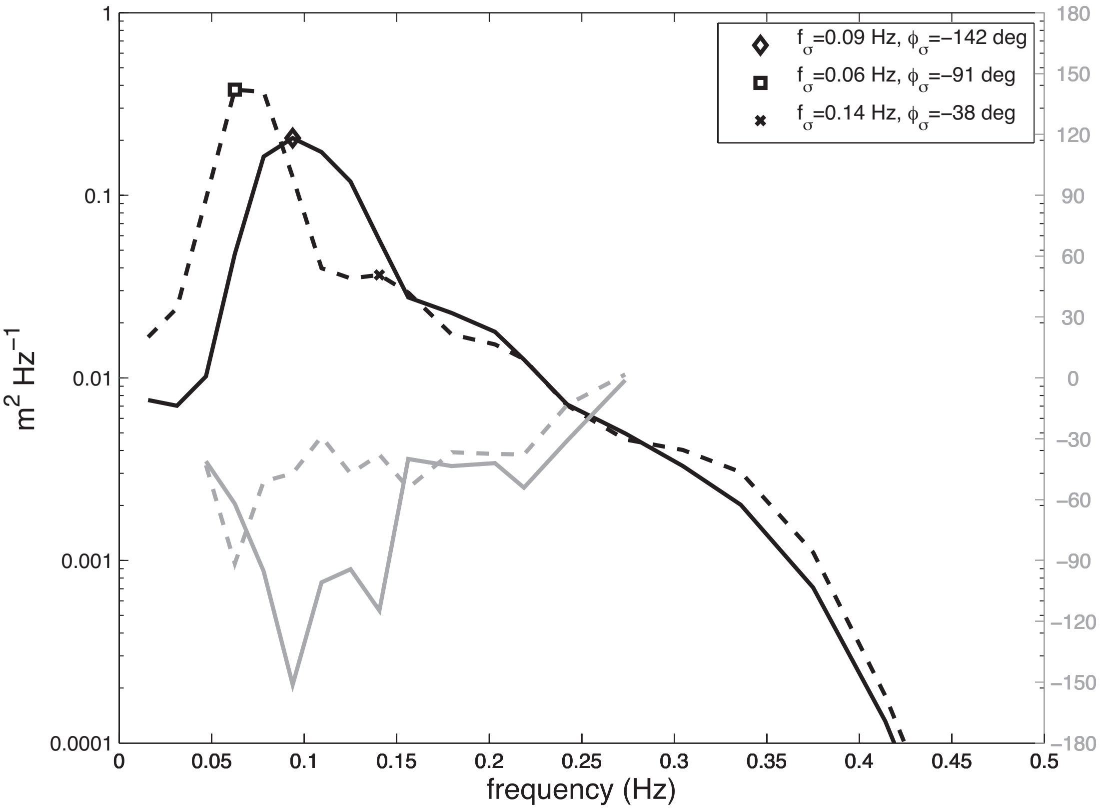

Figure 2.2: Directional surface wave spectra measured by the PUV sensor. Significant wave heights for the two s time periods shown are 0.49 m (solid traces) and 0.56 m (dashed traces). Black traces are surface displacement (left-and vertical scale) and gray traces are direction of origin (right-hand vertical scale).

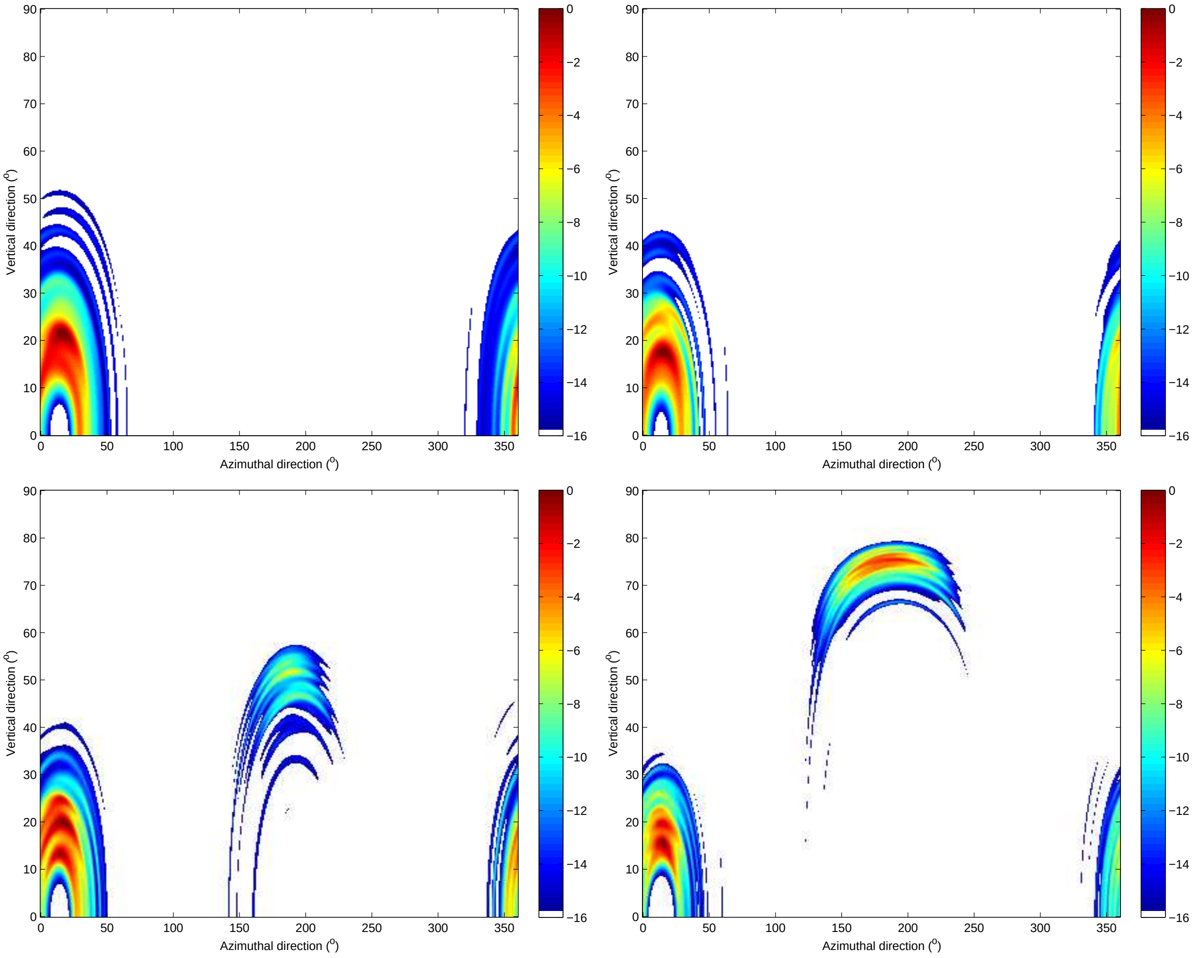

Figure 2.3: Narrowband beamformer, sweeping in azimuthal and vertical angles. Vertical axis units are dB, normalized by the peak value in the known source direction (20° azimuth). The four images correspond to four acoustic frequencies (clockwise from upper left: 280, 370, 695 and 535 Hz). The steeper arrivals at 535 and 695 Hz are grating lobes.

of the surface height, and directional spectra are computed for each surface wave time-series. Wavenumber vectors $\boldsymbol{\kappa}$ for surface waves at each spectral frequency component σ are computed using the measured propagation direction ϕ_σ.

$$\begin{aligned}\boldsymbol{\kappa} &= -\kappa \sin\phi_\sigma \hat{x} - \kappa \cos\phi_\sigma \hat{y} && (2.2)\\ &= \kappa_x \hat{x} + \kappa_y \hat{y} && (2.3)\end{aligned}$$

Here ϕ_σ is the angle from north of the direction of origin of the surface wave component with frequency σ, and $\hat{x}$ and $\hat{y}$ are the east-west and north-south unit vectors, respectively. These measured ocean wavenumber vectors are projected into the vertical plane of acoustic propagation between the source and the center of the hydrophone arrays. If ϕ_{ac} is the angle from North of the direction from source to receiver, then

$$\boldsymbol{\kappa} = \kappa_\parallel \hat{r} + \boldsymbol{\kappa}_\perp \hat{\phi} \tag{2.4}$$

where

$$\kappa_\parallel = |\boldsymbol{\kappa}_\parallel| = \kappa_x \sin\phi_{ac} + \kappa_y \cos\phi_{ac} \tag{2.5}$$

is the projection of the ocean surface wavenumber into the vertical plane between the acoustic source and receiving array. The unit vector $\hat{r}$ is horizontally oriented outward from the source, and the angle ϕ increases clockwise out of the vertical plane connecting the source to the receiving array (Fig. 2.1).

The Bragg condition for scattering of acoustic waves from a rough surface is

$$\boldsymbol{k}_s = \boldsymbol{k}_i \pm \boldsymbol{\kappa} \tag{2.6}$$

where $\boldsymbol{k}_s$ and $\boldsymbol{k}_i$ are, respectively, the scattered and incident acoustic wavenumber vectors, and $\boldsymbol{\kappa}$ is the wavenumber vector of the surface roughness. If the vectors of Eq. 2.6 are broken into components parallel and perpendicular to the vertical plane of acoustic propagation between the source and receiving array, then the scattered acoustic wavenumber in the vertical plane becomes

$$\boldsymbol{k}_{r,s} = (k_{r,i} \pm \kappa_\parallel)\hat{r} - k_z \hat{z} \tag{2.7}$$

Thus, by first-order perturbation, the vertical component k_z of the incident surface wavenumber $\boldsymbol{k}_i$ is unchanged by interaction with the rough ocean surface. According to Eq.2.7, the Bragg condition for the 2-dimensional scattering problem, the scattered acoustic arrival angles $\theta_n^{\pm}$ are altered from the non-perturbed arrival angles $\theta_n = \arctan \frac{k_{zn}}{k_{rn}}$ by addition and subtraction of the parallel components $\kappa_{\|}$ of the surface wavenumber vectors with the horizontal acoustic wavenumbers k_{r_n}:

$$\theta_n^{\pm} = \arctan \frac{k_{z_n}}{k_{r_n} \pm \kappa_{\|}} \tag{2.8}$$

The temporal frequencies of these scattered acoustic arrivals are likewise Doppler-shifted from the transmitted frequency by an amount equal to $\pm\sigma$, the surface wave frequency. The origins of Eqs. 2.6 and 2.7 are described more thoroughly in Section 2.4.

In order to relate the received scattered signal to the measured directional surface wave spectra, ambiguities in the acoustic directional spectra arising from hydrophone array geometry must be reduced. This is especially important for a search that is restricted to two dimensions, since scattering is spatially a 3-dimensional problem (Eq. 2.6). The manner in which the hydrophone array was deployed resulted in a less-than perfectly linear geometry (Fig. 2.1), thereby giving the array not only endfire aperture useful for resolving horizontal acoustic wavenumbers, but also limited broadside aperture useful for reducing conical ambiguities that arise when using a perfectly linear array in an isospeed propagation medium. Moreover, directional acoustic spectra are estimated using a data-adaptive technique with a white-noise constraint (WNC) of -6 dB. Such techniques can offer much better resolution than their conventional counterparts. Narrowband beamformer results for a search in vertical and azimuthal angles (Fig. 2.3), when using the array's full 2-dimensional aperture, show clear evidence of acoustic multipath, as well as diminished conical ambiguity surfaces. When the same search was performed using only the central, nearly perfectly linear segment of the array (omitting the portions adding broadside aperture), the vertical angle resolution and ambiguity surfaces worsened considerably.

Because adaptive processing algorithms such as this require the cross-spectral density matrix (CSDM) to be full rank for stable inversion in their incorporation into the steering or replica vectors [Hay96], there is a natural trade-off between spatial and temporal resolutions. In order to achieve the ability to resolve acoustic temporal frequency deviations caused by the surface waves that are small (.06

Hz) compared to the acoustic carrier frequencies (280, 370, 535 and 695 Hz), long, zero-padded FFT's ($N_{data} \sim 30000$ points, $N_{FFT} = 2^{15}$ points) are used to estimate the temporal spectrum of the signal received on each hydrophone. It was found that a maximum of 52 hydrophones could be used for this processing when two consecutive, 5-minute recordings of the CW tones are processed without sacrificing temporal resolution, while including sufficient snapshots to ensure statistically reliable results, and while confining the processing to times when the surface waves were steady throughout. These 52 hydrophones are chosen to span the entire length of the array to optimize the vertical and azimuthal angle resolutions in processing. The hydrophone array was constructed to offer optimal resolution at 400 Hz when the sound speed uner water is 1500 m s^{-1}. Therefore, all acoustic signals with frequency conent $>$ 400 Hz will be spatially aliased by this array when it is stretched to its full length. However, since the location of the source relative to the arrays is well known, and because of the effectiveness of the WNC beamforming algorithm, grating lobes arising from spatial aliasing of the 535- and 695-Hz tones is not of major concern (Fig. 2.3).

2.3.2 Measured acoustic modes

During the experiment, in addition to the acoustic instrumentation and the PUV sensor, which could also be used to measure depth fluctuations throughout the experiment, Conductivity and Temperature vs. Depth (CTD) profiles were taken. These profiles showed that the acoustic environment was a shallow (10 m), iso-speed (1510 m s^{-1}) waveguide. The bottom consisted of a layer of sediments (1 m thick, $c_s = 1575\,\mathrm{m\,s^{-1}}, \alpha_s = 0.9\,\mathrm{dB}/\lambda$) overlying a hard bottom ($c_b = 1680\,\mathrm{m\,s^{-1}}$, $\alpha_b = 0.3\mathrm{dB}/\lambda$)[McA02]. Over the course of the experiment, surface wave conditions varied widely in amplitude, and in frequency σ and direction ϕ_σ of the dominant spectral components (Fig. 2.2). At times, multiple, independent surface wave systems were present, with multiple simultaneous peak frequencies and directions of arrival. These changes are reflected in the acoustic vertical beamformer output. This study focuses on two time periods during the experiment. During the first, the significant wave height was 0.66 m, and the dominant component had a frequency of 0.09 Hz and originated from -142° from North. The water depth was 9.7 m. Later in the experiment, during the second time period of focus, the significant wave height was 0.56 m, and there were two dominant frequencies, 0.06 and 0.14 Hz, originating from two different directions, -91° and -38°, respectively (Fig. 2.2), and the water depth was 9.5 m.

Table 2.1: Vertical Bragg scattering: $f_w = 0.09$ Hz, $k_w = 0.063$ rad m^{-1}, $\phi_w = -142°$, $H_s = 0.66$ m, $D = 9.7$ m

$f_\circ$ (Hz)	k_{r_n} (m^{-1})	θ_n (°)	$k^+_{r_n}$ (m^{-1})	θ^+_n (°), "△"	$k^-_{r_n}$ (m^{-1})	θ^-_n (°), "▽"
280	1.131	14.0	1.070	14.7	1.191	13.3
	1.088	21.0	1.027	22.1	1.149	20.0
370	1.464	18.0	1.403	18.7	1.525	17.3
535	2.123	17.5	2.062	18.0	2.184	17.0
695	2.834	11.5	2.773	11.7	2.895	11.3
	2.750	18.0	2.690	18.4	2.811	17.6

Table 2.2: Vertical Bragg scattering: $f_w = .06$ Hz, $k_w = 0.04$ rad m^{-1}, $\phi_w = -91°$, $H_s = 0.56$ m, $D = 9.5$ m

$f_\circ$ (Hz)	k_{r_n} (m^{-1})	θ_n (°)	$k^+_{r_n}$ (m^{-1})	θ^+_n (°), "△"	$k^-_{r_n}$ (m^{-1})	θ^-_n (°), "▽"
280	1.105	18.5	1.088	18.7	1.121	18.2
370	1.456	19.0	1.439	19.2	1.472	18.8
	1.384	26.0	1.367	26.2	1.400	25.7
535	2.145	15.5	2.129	15.6	2.162	15.4
	2.092	20.0	2.075	20.1	2.108	19.9
	2.026	24.5	2.009	24.7	2.042	24.3
695	2.709	20.5	2.692	20.6	2.725	20.4
	2.632	24.5	2.615	24.6	2.648	24.4

Horizontal mode numbers are found using a Hankel transform approximation using the pressure field measured by the entire endfire array (Fig. 2.1).

$$\tilde{p}(k_r, \omega) = \int_0^\infty dr\, r\, H_\circ(k_r r) p(r, \omega) \tag{2.9}$$

where $p(r, \omega)$ and $\tilde{p}(k_r, \omega)$ are a scalar function transform pair of distance r and wavenumber k_r (respectively), and freqency ω. $H_\circ$ is the Hankel function of the first kind (order 0). Here it has been assumed that the acoustic wave field at frequency ω is entirely outgoing, and that the geometry is radially symmetric. Equation 2.9 describes the complete spatial spectrum, including both the discrete

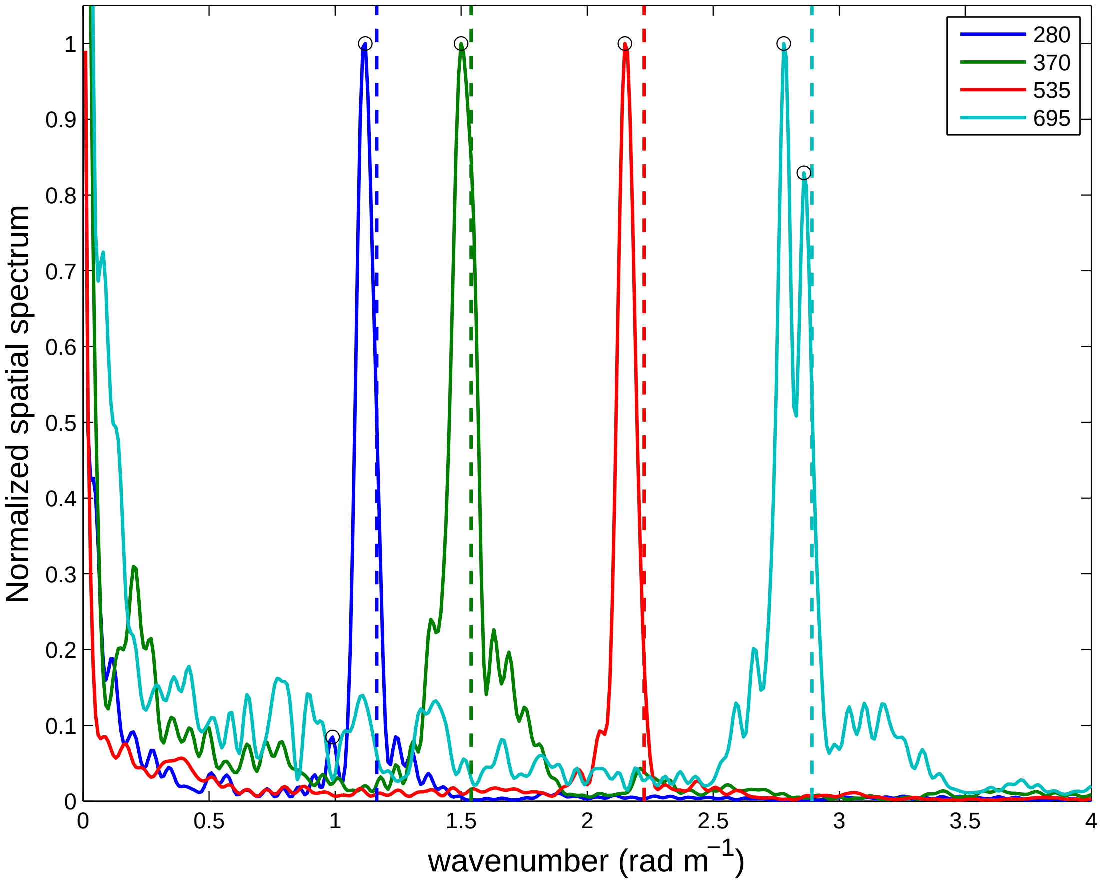

Figure 2.4: Acoustic horizontal spatial spectrum computed at four temporal frequencies using a Hankel Tranform of data measured on the endfire array. The water depth during this time period of the experiment was 9.7 m. Vertical dashed lines indicate acoustic wavenumber amplitudes at the 4 transmitted frequencies $k_\circ = 2\pi f_\circ / c$. Circles ("$\circ$") indicate modes included in predictions of Bragg scattering in Fig. 2.6.

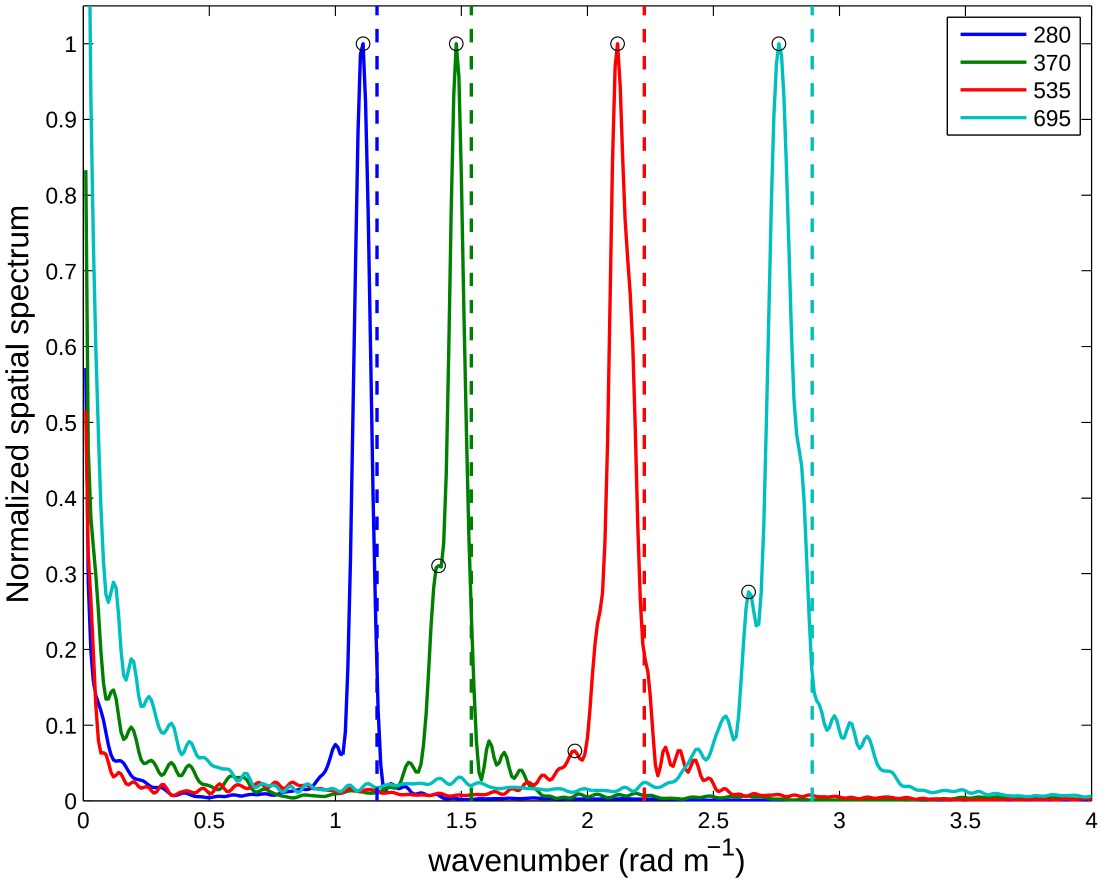

Figure 2.5: Acoustic horizontal spatial spectrum computed at four temporal frequencies using a Hankel Tranform of data measured on the endfire array. The water depth during this time period of the experiment was 9.5 m. Vertical dashed lines indicate acoustic wavenumber amplitudes at the 4 transmitted frequencies $k_\circ = 2\pi f_\circ / c$. Circles ("$\circ$") indicate modes included in predictions of Bragg scattering in Fig. 2.7.

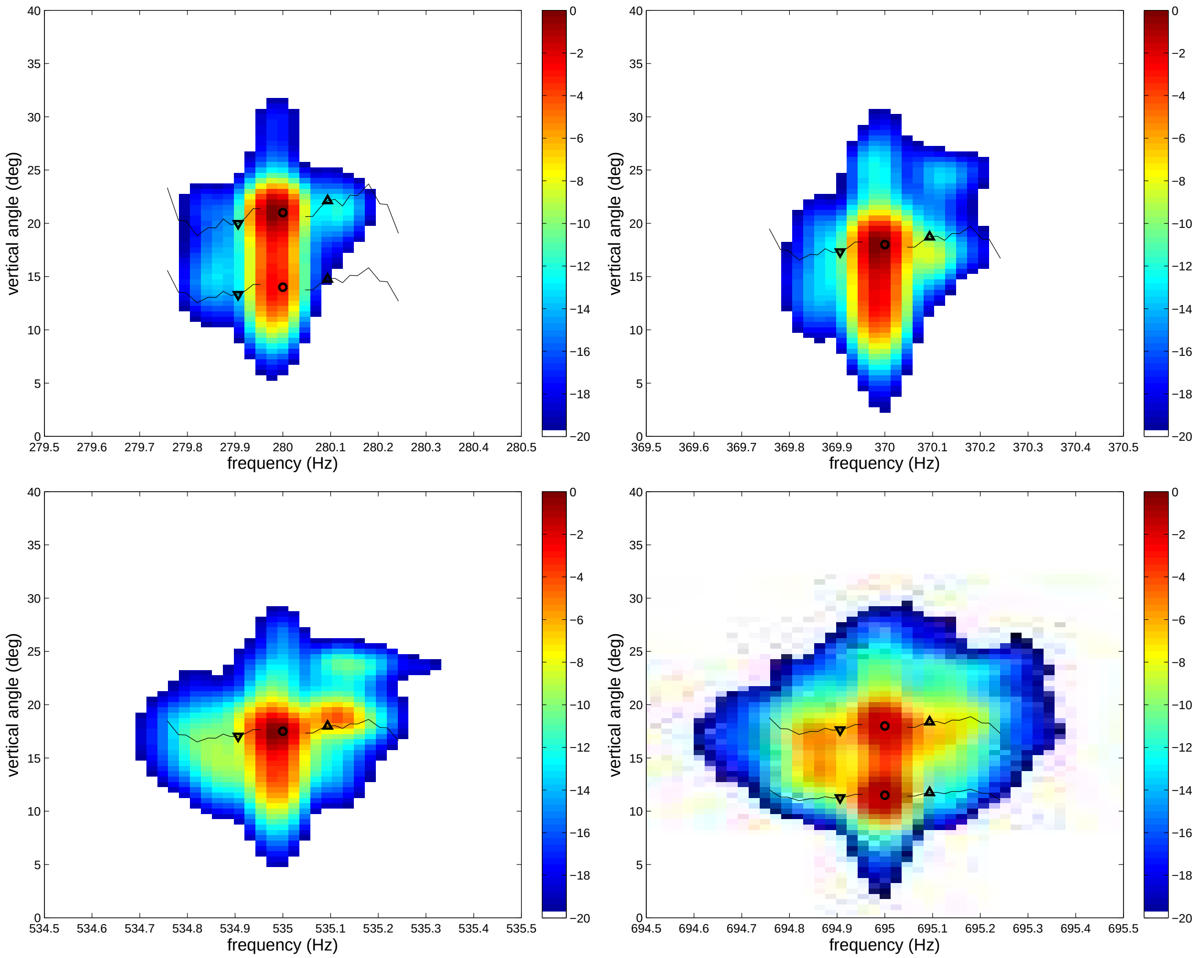

Figure 2.6: Plane-wave vertical beamformer showing Doppler shifting and Bragg scattering from ocean surface waves with peak frequency 0.09 Hz propagating from -142°. Black lines indicate the continuous directional surface wave spectrum. Circles (“○”) indicate measured modes. Triangles indicate predicted Bragg scattered arrivals (“▽” for $-\sigma$ Doppler shift and “△” for $+\sigma$ Doppler shift).

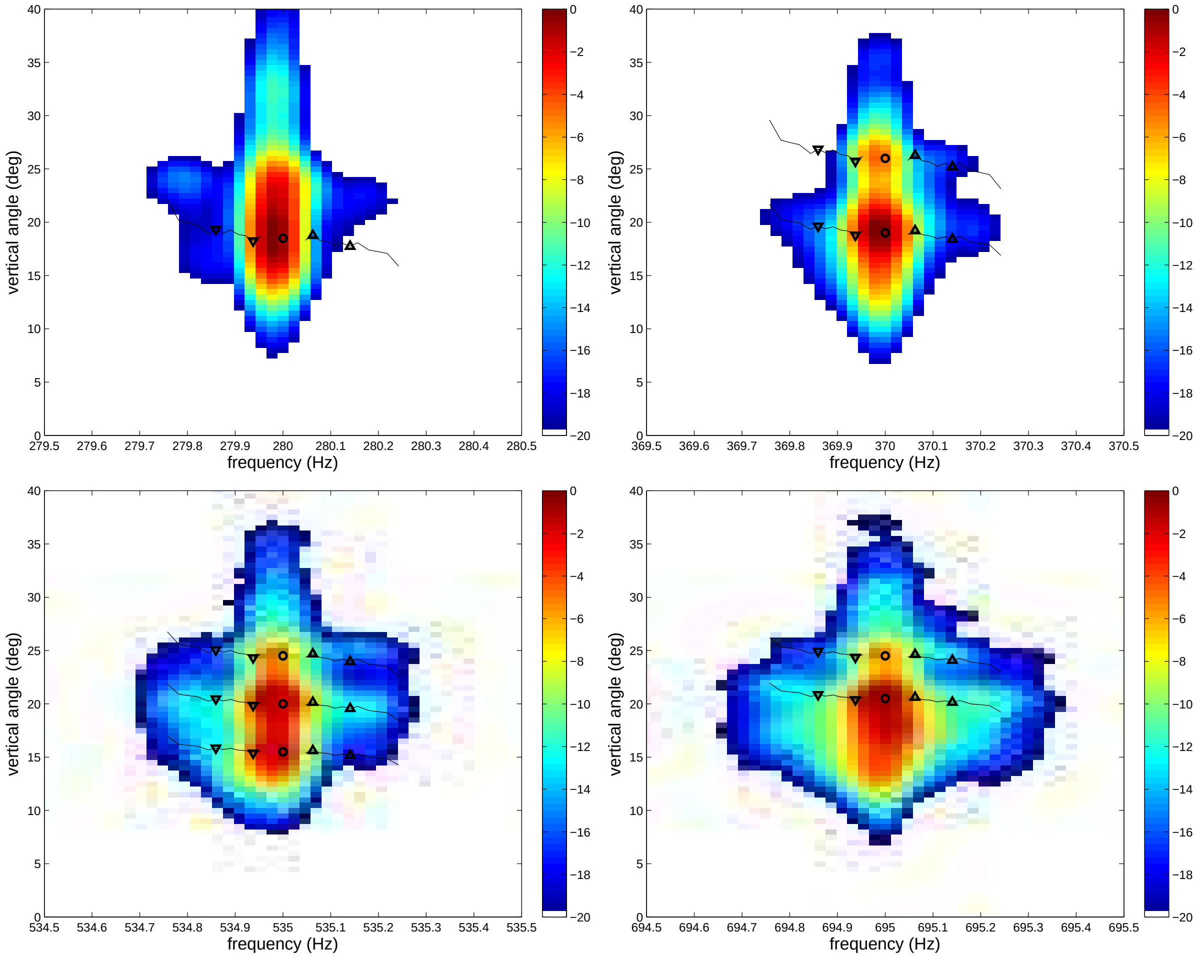

Figure 2.7: Plane-wave vertical beamformer showing Doppler shifting and Bragg scattering from ocean surface waves with peak frequencies of .06 Hz and .14 Hz, propagating from -91° and -38°, respectively. Black lines indicate the continuous directional surface wave spectrum. Circles (“$\circ$”) indicate measured modes. Triangles indicate predicted Bragg scattered arrivals (“$\bigtriangledown$” for $-\sigma$ Doppler shift and “$\bigtriangleup$” for $+\sigma$ Doppler shift).

Table 2.3: Vertical Bragg scattering: $f_w = .14$ Hz, $k_w = .10$ rad m^{-1}, $\phi_w = -38°$, $H_s = 0.56$ m, $D = 9.5$ m

$f_\circ$ (Hz)	k_{r_n} (m^{-1})	θ_n (°)	$k^+_{r_n}$ (m^{-1})	θ^+_n (°), "△"	$k^-_{r_n}$ (m^{-1})	θ^-_n (°), "▽"
280	1.105	18.5	1.156	17.7	1.054	19.3
370	1.456	19.0	1.507	18.4	1.405	19.6
	1.384	26.0	1.435	25.2	1.333	26.9
535	2.145	15.5	2.196	15.2	2.094	15.9
	2.092	20.0	2.143	19.6	2.041	20.5
	2.026	24.5	2.077	24.0	1.975	25.1
695	2.709	20.5	2.760	20.2	2.658	20.9
	2.632	24.5	2.682	24.1	2.581	24.9

and continuous parts. Singularities in this complex integral (Eq. 2.9) correspond to the propagating modes, and they appear as large peaks in the approximated spectrum. Section 2.4 further discusses of the relationship between spectral methods and mode theory, and their role in time-dependent scattering theory.

In this study the acoustic spatial spectrum is estimated by first implementing a temporal FFT of the pressure time series recorded by a set of hydrophone elements whose ranges from the source vary, and then numerically computing the integral in Eq. 2.9 at the frequencies transmitted by the acoustic source. While the limits of integration in Eq. 2.9 are 0 to ∞, in practice the integral must be truncated from r_{min} to r_{max}, the minimum and maximum distances, respectively, from the source to the hydrophone elements. As with the FFT, the snapshot length, or the total aperture in range of the array ($r_{max} - r_{min}$) determines the wavenumber resolution limit that can be obtained when computing the numerical Hankel transform using conventional computation methods. Since the waveguide where the experiment was conducted was iso-speed with known sound speed, measured horizontal wavenumbers associated with vertical acoustic modes are easily related to the vertical beam pattern of the non-Doppler-shifted signal through vertical angles of arrival:

$$\tan\theta_n = \frac{k_{z_n}}{k_{r_n}} \tag{2.10}$$

where each θ_n is a vertical angle of arrival, and the vertical and horizontal wavenumber components k_{z_n} and k_{r_n} (respectively) associated with θ_n are related to the acoustic wavenumber k through $k^2 = k^2_{z_n} + k^2_{r_n}$.

Horizontal mode numbers are also computed indirectly using the plane-wave vertical beamformer, where peaks in the output are θ_n. While it may seem that these two methods are identical, they are actually arriving at the same result from very different approaches. Equation 2.9 is a mathematical mapping of a function from one space into another, much like the temporal Fourier transform maps functions of time into functions of frequency. Thus, it is always true, and can always be computed when the locations of the hydrophones are known, and is not based on assumptions of propagation parameters. In order to infer arrival angles or full wavenumber vectors, however, information about the physical setting is required. The vertical beamformer, on the other hand, begins with assumptions of the environment, and matches data with replica vectors based on those assumptions. Discrepancies between the wavenumbers computed from Eq. 2.9 and those computed from the beamformer output may indicate mismatch between the assumed and actual propagation parameters.

In a shallow, iso-speed waveguide such as that where the experiment took place, water depth significantly influences the received acoustic field through its effect on the number and shape of propagating modes, as well as the excitation of them. Tidal changes stretch and compress the mode functions at a given acoustic frequency, and alter the horizontal mode numbers. In some cases tidal fluctuations can cause the number of propagating modes to change with time. With the source held in a fixed position, the changing water depth effectively moves the source vertically along the mode functions, thereby altering the excitation of each in time. Horizontal spatial spectra computed from pressure time series recorded on the endfire array show a temporal dependence of relative mode levels. While a normal mode model using inputs based on the measured acoustic properties of the experiment site might predict more propagating modes, the current study is restricted to those that were positively identified in the measured spatial spectra (Figs. 2.4 and 2.5) and vertical beamformer output. Horizontal mode numbers for each of the 4 transmitted frequencies inferred from the measured spatial spectra (Figs. 2.4 and 2.5) are listed in Tables 2.1, 2.2 and 2.3. In Figs. 2.6 and 2.7, a "$\circ$" marks the each of the angles corresponding to the modes identified at each of the four transmitted frequencies.

Given that the number of propagating acoustic modes increases with acoustic frequency, and higher order modes change more rapidly in space than do lower order modes, the sensitivity to depth changes of the received acoustic field likewise increases with frequency. During the first time period, when the depth was 9.7 m, two horizontal mode numbers were identified at 280 Hz with values of 1.131 and 1.088 rad m^{-1} (Figs 2.4 and 2.5), corresponding to vertical arrival angles of 14° and 21° (Figs. 2.6 upper left and 2.7 upper left). During the second time period, when the depth was 9.5 m, a single mode was identified at 280 Hz with a horizontal wavenumber of 1.105 rad m^{-1} (vertical arrival angle 18.5°). At 370 Hz, the opposite occured: one mode was identified during the first time period, with a value of 1.464 rad m^{-1}, and two were found during the second time period, with values of 1.456 and 1.384 rad m^{-1}. The vertical angles corresponding to these modes were 18° during the first time period and 19° and 26°.

The most drastic changes in mode excitation occur at 535 Hz. Though there are more propagating modes at this higher frequency than at 280 or 370 Hz, during the first time period only one was positively identified in both the horizontal spatial spectrum and the vertical beamformer output. The value of this single horizontal wavenumber during the first time period of 2.123 rad m^{-1} (vertical arrival angle 17.5°, Figs. 2.5 and 2.7, lower left) is lower than the highest value (2.145 rad m^{-1}, vertical arrival angle 15.5°) but higher than the second mode (2.092 rad m^{-1}, vertical arrival angle 20.0) during the second time period (Figs. 2.4 and 2.6, lower left). The third mode during the second time period had a horizontal wavenumber of 2.026 rad m^{-1} (vertical arrival angle 24.5°).

Two modes were positivley identified at 695 Hz during both the first and second time periods in both the spatial spectrum (Figs. 2.5 and 2.5) and the vertical beamformer output (Figs. 2.6, lower right and 2.7, lower right). The two horizontal mode numbers were 2.834 and 2.750 rad m^{-1} (vertical arrival angles 11.5° and 18.0°, respectively) during the first time period (Figs. 2.4 and 2.6, lower right), and 2.709 and 2.632 rad m^{-1} (vertical arrival angles 20.5° and 24.5°, respectively) during the second time period (Figs. 2.5 and 2.7, lower right).

2.3.3 Scattering in the vertical plane: measurements and predictions

A comparison of the directional acoustic spectrum for two time periods during the experiment clearly illustrates the dependence of the received, scattered acoustic signal's frequency and angles of arrival on the ocean surface wave spectrum through the Bragg and linear surface wave dispersion relations (Eqs. 2.7 and 2.1, respectively). Associated with all of these observed propagating modes are pairs of sidebands in the (± 1 Hz) vertical beamformer output, with variable frequency and angle offsets. Sidebands in the acoustic directional spectra are symmetric in frequency, and the peaks' offsets are equal to $\pm\sigma$, the dominant surface wave frequencies (Figs. 2.2, 2.6 and 2.7). This observation is consistent with first-order perturbation theory [HL75a, PW91], as well as phase modulation without scattering [LBD08, PN78]. Deviations in the vertical angles of arrival of the scattered sidebands obey Eq. 2.8, where the ocean surface wavenumber vectors are found using the linear dispersion relation (Eq. 2.1) and the measured directional surface wave spectrum (Fig. 2.2). The sizes of the angle deviations increase with lower acoustic carrier frequency, since at lower frequencies the magnitudes of the acoustic and ocean surface wavenumbers are more similar, and the relative changes in horizontal acoustic wavenumber resulting from scattering (Eq. 2.7) are larger at lower acoustic frequencies than at higher frequencies. The sign of the vertical angle deviation resulting from scattering from the rough, moving surface is determined by the direction of the parallel component of the surface waves relative to the acoustic propagation direction (Fig. 2.1). If $k_{r,i}$ and $\kappa_{\|}$ are the same sign (Eq. 2.7), then the $-\sigma$ Doppler-shifted sideband will correspond to the shallower angle of arrival θ^{-}, whereas if $k_{r,i}$ and $\kappa_{\|}$ are opposite sign, then the $-\sigma$ Doppler-shifted sideband will correspond to a steeper vertical angle of arrival, $\theta^{-} > \theta_{\circ}$. When the plane-wave beamformer output is viewed in $f-\theta$-space, horizontal wavenumber differences associated with the positively and negatively Doppler shifted sidebands are symmetrical about the horizontal modenumbers, the angle deviations associated with them are not symmetrical about the non-scattered, non-frequency-shifted arrival, due to the trigonometric relationship between the acoustic wavenumbers and measured vertical arrival angles (Eq. 2.10). The vertical angles of arrival θ are measured from the horizontal, positive upwards.

Tables 2.1, 2.2 and 2.3 contain the measured surface wave dominant frequencies σ, their respective wavenumbers κ, directions of origin ϕ_σ, and the associated vertical angles of arrival $\theta_n^\pm$ expected for each of the measured acoustic horizontal mode numbers k_{r_n}, where $\theta^\pm$ is the angle associated with the $\pm\sigma$-Doppler-shifted sideband. The expected angles of arrival θ_n of the propagating acoustic modes, and the expected angles $\theta_n^\pm$ of the scattered sidebands are marked on Figs. 2.6 and 2.7 ("$\circ$" for unperturbed arrivals, "$\bigtriangledown$" for $-\sigma$ Doppler shift and "$\triangle$" for $+\sigma$ Doppler shift).

During the earlier time period, when the dominant surface wave spectral component had a frequency of 0.09 Hz (11 s period) and was arriving from -142° from North, both positively and negatively frequency-shifted sidebands are visible in the directional acoustic spectrum around 695 Hz. Predictions from Eq. 2.8 of the angles of arrival for the scattered sidebands agree well with the measured sidebands for whole measured surface wave spectrum and the steeper non-shifted arrival (18°). The peaks of these sidebands (18.4° and 17.6°) coincide well with the dominant surface wave frequency, $\pm\sigma$. Though there is frequency spreading at the lower angled arrival (11.5°), there are no nearby, distinct peaks or patterns that can be attributed confidently to the Bragg condition associated with this mode.

The results observed at 535 Hz during the first time period are striking. While the negatively Doppler-shifted sideband lacks a distinct peak at the surface wave dominant frequency, its shape nonetheless echoes that predicted from the Bragg condition for the full directional ocean surface wave spectrum (Eq. 2.5). Meanwhile, the positively Doppler-shifted sideband clearly coincides in both frequency and angle deviation with the prediction of Eqs. 2.8 and 2.5 for the full surface wave spectrum and measured acoustic mode. Moreover, other frequency-shifted sidebands are visible in the beamformer output at 535 Hz that may be associated with an acoustic mode that was not fully resolved in the spatial spectrum measured during this time period.

From Eqs. 2.1, 2.5 and 2.7, it can be expected that the vertical angle deviations associated with Bragg scattering will be greater at lower acoustic frequencies. Predictions of angle deviations (0.7° for $+\sigma$ and $-0.7°$ for $-\sigma$) at 370 Hz for a main, unshifted arrival at 18° are greater than those predicted and observed (0.3°) at 695 Hz for an arrival of similar angle. While the peak of the negatively Doppler-shifted sideband is less distinct (Fig. 2.6, upper right), both sidebands roughly follow the shifts predicted by Eqs 2.5 and 2.8 for the continuous ocean surface wavenumber spectrum. As with the results at 535 Hz, at 370 Hz, while one mode is positively identified (Figs. 2.4 and 2.6, upper right), there are sidebands observed that seem to coincide with the predictions of Eqs. 2.7 and 2.5 for a higher-angled arrival not positively identified in the spatial spectrum or beamformer output.

Similar results are visible for both modes identified at 280 Hz, with the asymmetry in angle of arrival deviation arising from the trigonometric relationship in Eq. 2.8 made more clear at the lower acoustic frequency. There is a measured asymmetry in the level of the received, scattered sidebands for both of the identified modes. The level of the positively Doppler-shifted sideband at 21° is higher than that of the negatively shifted band, but the opposite is true for the 14° arrival (Fig. 2.6, upper left). Both these higher level peaks coincide well with predictions of scattered sidebands, though the other components of the surface wave spectrum have less effect on the received field at 280 Hz.

During the later time period there are multiple peaks in the surface wave spectrum, with dominant frequencies of 0.06 and 0.14 Hz, propagating from $-91°$ and $-38°$, respectively. Though the lower frequency ocean surface wave peak is much higher than that of the higher frequency component (Fig. 2.2), the scattering effects of that spectral component are not readily identifiable in the measured acoustic directional spectra. While a general broadening in frequency of the acoustic arrivals is observed (Figs. 2.6 and 2.7), the separation of the Doppler-shifted signals in angle and in frequency is too small to be discerned. The smaller, higher frequency wave component is visible in the beamformer output, however. In fact, for multiple modes at multiple of the transmitted acoustic frequencies, Doppler shifting and angle deviations are observed that coincide exactly with the predictions of the distortions resulting from the continuous surface wave spectrum. The projections of the dominant ocean surface wavenumber vectors into the vertical acoustic plane result in oppositely signed horizontal wavenumbers in the scattering Equations (2.7 and 2.8). Additionally, the higher peak frequency component measured during the later time period is both slightly higher frequency than the lone dominant component observed during the earlier time period, and the sign of the wavenumber projections are also opposite. Therefore, by Eq. 2.8, the expected vertical scattered angle deviations (Tables 2.2 and 2.3) will be of opposite sign as those seen in the earlier time period (Fig. 2.6), and the deviations are of different magnitude.

The scattered Doppler-shifted sidebands associated with both the modes identified at 695 Hz (vertical arrival angles 20.5° and 24.5°) coincide with the vertically scattered angles of arrival predicted by Eqs. 2.7 and 2.8 (Fig. 2.7, lower right) for the higher frequency of the two dominant surface wave components during the second time period. Moreover, the scattered sidebands, which extend in frequency well beyond the higher of the dominant surface wave frequencies, agree with predictions for frequency and wavenumber shift for the entire measured directional surface wave spectrum (Fig. 2.7, lower right).

Similar to the observations at 695 Hz, Doppler-shifted, Bragg scattered acoustic arrivals are observed corresponding to all 3 identified modes at 535 Hz. The correspondance between predictions from time-dependent, first order perturbation mode theory and the recorded acoustic field is most clear for the second mode (vertical angle 20.0°), as both the positively and negatively Doppler shifted sidebands show peaks at the higher of the two dominant surface wave frequencies. While the peaks of the scattered sidebands for the first and third modes (vertical angles 15.5° and 24.5°, respectively) are less distinct, the shape suggests the same pattern of Doppler-shifted Bragg scattering (Fig. 2.7). Predictions of Doppler shift and scattering for the whole of the continuous surface wave spectrum agree with observed sidebands for each of the three positively identified modes.

At 370 Hz, at the higher of the two dominant surface wave frequencies σ during the second time period, the observed scattered, $+\sigma$ Doppler-shifted sideband associated with the higher order propagating acoustic mode occurs as Eq. 2.8 predicts, while the negatively Doppler-shifted sideband cannot be identified above the noise background (Fig. 2.7, upper right). While the scattered sidebands associated with the lower order mode at 370 Hz are weaker in amplitude than the those observed at higher acoustic frequencies and during the first time period, their displacements in both frequency and vertical angle agree with those predicted by the time-dependent scattering theory (Eq. 2.7). During the second time period, while there are Doppler-shifted sidebands observed at 280 Hz, and while their breadth in frequency coincides with that predicted by time-dependent perturbational theory, they do not coincide exactly to the single mode identified in both the spatial spectrum (Fig. 2.5) and the beamformer output (Fig. 2.7, upper left). However, their width in frequency and their following the same directional trend as indicated by the predicted results for the positivley identified mode suggests that it is possible that these sidebands are the Bragg-scatttered version of some higher-order mode that could not be fully resolved.

2.4 Normal mode propagation and first-order perturbation

Data analyses such as those presented in Sect. 2.3.3 are much more instructive when guided by an analytical approach that describes the complicated scattered acoustic field. A perturbational approach to scattering acoustics begins with the premise that the total acoustic field is comprised of the original, unperturbed contribution that is the solution to the ideal case. The unperturbed solution is then corrected by a series of contributions of increasing order of some positive real expansion parameter (e.g. kh, where k is the acoustic wavenumber and h is the scale of ocean surface roughness). Each subsequent term or contribution decreases in relative importance: the size of the expansion parameter is defined as “small” ($kh \ll 1$). In this section one such expansion is computed for the purpose of illuminating the observed broadband scattering. The approach here is similar to that of Harper and Labianca[HL75a], in that it is a small wave height expansion based on a normal mode acoustic propagation model. Other approaches base the expansion on more generalized plane-wave fields [PW91], or use small slope [TB95], Kirchoff [McD92] approximations.

The range-independent acoustic wave equation with point-source forcing can be written as

$$[\rho(z)\bigtriangledown\cdot\frac{1}{\rho(z)}\bigtriangledown-\frac{1}{c^2(z)}\frac{\partial^2}{\partial t^2}]\psi(\mathbf{x},\mathbf{x_s},t)=S_\omega\delta(\mathbf{x}-\mathbf{x_s})e^{-i\omega_\circ t-i\gamma_\circ} \tag{2.11}$$

where $\omega_\circ$ is the source frequency, $\gamma_\circ$ is a constant, S_ω is the source amplitude, $c(z)$ is the sound speed, and $\rho(z)$ is the medium density. The scalar function ψ is a function of source and receiver locations $\mathbf{x}$ ($=[x,y,z]=[\mathbf{r},z]$) and $\mathbf{x_s}$ ($=[x_s,y_s,z_s]=[\mathbf{r_s},z_s]$), respectively, and time t.

The Fourier Transform pair is defined as

$$\begin{aligned}\widetilde{\psi}(\mathbf{x},\mathbf{x_s},\omega) &= \int_{-\infty}^{\infty}dt\,e^{-i\omega t}\psi(\mathbf{x},\mathbf{x_s},t)\\ \psi(\mathbf{x},\mathbf{x_s},t) &= \frac{1}{2\pi}\int_{-\infty}^{\infty}d\omega\,e^{i\omega t}\widetilde{\psi}(\mathbf{x},\mathbf{x_s},\omega)\end{aligned} \tag{2.12}$$

If a Fourier Transform with respect to the time variable is performed on the wave equation (Eq 2.11), the result is the inhomogeneous Helmholz equation:

$$[\rho(z)\bigtriangledown\cdot\frac{1}{\rho(z)}\bigtriangledown-k^2]\widetilde{\psi}(\mathbf{x},\mathbf{x_s},\omega)=S_\omega\delta(\mathbf{x}-\mathbf{x_s})\delta(\omega-\omega_\circ) \tag{2.13}$$

where $k(z)^2=\omega^2/c(z)^2$ is the square of the acoustic wavenumber. This equation can be rearranged to

$$[\rho(z)\frac{\partial}{\partial z}\frac{1}{\rho(z)}\frac{\partial}{\partial z}+\bigtriangledown_H^2+k(z)^2]\widetilde{\psi}(\mathbf{x},\mathbf{x_s},\omega)=-S_\omega\delta(\mathbf{x}-\mathbf{x_s})\delta(\omega-\omega_\circ) \tag{2.14}$$

Here $\bigtriangledown_H^2$ is the Laplacian operator in the horizontal coordinates.

Examining the homogeneous (unforced) version of Equation 2.14, it becomes apparent that each of the terms on the left-hand side is either strictly a function in horizontal coordinates or is strictly a function of depth.

$$\bigtriangledown_H^2\widetilde{\psi}(\mathbf{x},\mathbf{x_s},\omega)+[\rho(z)\frac{\partial}{\partial z}\frac{1}{\rho(z)}\frac{\partial}{\partial z}+k(z)^2]\widetilde{\psi}(\mathbf{x},\mathbf{x_s},\omega)=0 \tag{2.15}$$

Thus, in order for Eq. 2.15 to be true both terms must be a constant. This constant is designated k_{n_r} and it is clear from Eq. 2.15 that this corresponds to the horizontal component of the acoustic wavenumber:

$$k_{n_r}^2=\frac{\omega^2}{c^2}-k_{n_z}^2 \tag{2.16}$$

The solution to Eq. 2.15 takes the form

$$\widetilde{\psi}(\mathbf{x}, \mathbf{x_s}, \omega) = \sum_{n=1}^{N} \Phi_n(\mathbf{r}, z_s, \omega)\Psi_n(z, \omega) + \int_0^{\infty} d\zeta \, \bar{\Phi}(\mathbf{r}, z_s, \zeta, \omega)\bar{\Psi}(z, \zeta, \omega) \tag{2.17}$$

where $\mathbf{x} = [\mathbf{r}, z]$ and the coordinate base has been defined such that the source range is zero, $\mathbf{x_s} = [\mathbf{0}, z_s]$. The integral term in Eq. 2.17 represents the continuous spectrum of the received field, and the term of summed discrete components corresponds to the propagating modes of the waveguide. The functions Ψ_n and $\bar{\Psi}$ are orthonormal:

$$\begin{aligned} \int_{-\infty}^{\infty} dz \, \frac{1}{\rho}\Psi_n(z, z_s, \omega)\Psi_m(z, z_s, \omega) &= 1, \, n = m \\ &= 0, \, n \neq \\ \int_{-\infty}^{\infty} dz \, \frac{1}{\rho}\bar{\Psi}(z, z_s, \zeta, \omega), \bar{\Psi}(z, z_s, \zeta', \omega) &= 1, \, \zeta = \zeta' \\ &= 0, \, \zeta \neq \zeta' \end{aligned} \tag{2.18}$$

Substituting Eq. 2.17 into Eq. 2.14 yeilds

$$\sum_{n=0}^{N} \Phi_n \rho(z) \frac{\partial}{\partial z} \frac{1}{\rho(z)} \frac{\partial}{\partial z} \Psi_n + \Psi_n \bigtriangledown_H^2 \Phi_n + k^2 \Phi_n \Psi_n = -S_\omega \delta(\mathbf{x} - \mathbf{x_s})\delta(\omega - \omega_\circ) \tag{2.19}$$

where the continuous spectrum portions of the solution $\bar{\Psi}$ and $\bar{\Phi}$ have been neglected. Rearranging and using the homogeneous Helmholz equation (Eq. 2.15), and subsequently applying the orthonormality condition (Eq. 2.18) results in

$$[\bigtriangledown_H^2 - k_{n_r}]\Phi_n = -S_\omega \frac{\Psi_n(z_s)}{\rho(z_s)} \delta(\omega - \omega_\circ) \tag{2.20}$$

This equation has the solution

$$\Phi_n(\mathbf{r}, z_s, \omega) = \frac{i}{4\rho(z_s)} \Psi_n(z_s) H_0(k_{n_r} r) \delta(\omega - \omega_\circ) \tag{2.21}$$

where H_0 is the Hankel function of the first kind, order 0, and it has been assumed that as $r \to \infty$, there are only out-going waves. The normal modes $\Psi_n(z)$ in Eqn. 2.17 are subject to the boundary conditions of the full solution $\tilde{\psi}$. In ocean acoustics the upper ($z = 0$) boundary is a pressure release boundary:

$$\psi(\mathbf{x}, \mathbf{x_s}, t) = 0, \; z = 0 \tag{2.22}$$

The bottom boundary condition is in general more complicated. The full solution to Eq. 2.14 for the range-independent waveguide with a source at $\mathbf{r_s} = [\mathbf{0}, z_s]$ radiating at frequency $\omega_\circ$ is

$$\widetilde{\psi}(\mathbf{x}, z_s, \omega) = \sum_{n=0}^{\infty} \frac{iS_\omega}{4k_{n_z}} \Psi_n(k_{n_z} z_s)\Psi_n(k_{n_z} z) H_0(k_{n_r} r)\delta(\omega - \omega_\circ) \tag{2.23}$$

The mode functions Ψ_n individually satisfy the upper and lower boundary conditions of the waveguide. The field in Eq. 2.23 includes only the discrete portion of the total field (Eq. 2.17). Recalling the spatial spectrum discussed in Section 2.3.2, it is easy to see that a Hankel transform (Eq. 2.9) of $\widetilde{\psi}$ in Eq. 2.23 will result in a series of delta functions $\delta(k - k_{r_n})$. Thus it is a useful tool to find the mode numbers of the acoustic field using the measurements of a horizontal array. As it will soon be seen, it is the horizontal mode numbers k_{r_n} that are affected by scattering from ocean surface waves.

Departing now from ideal wave guides with perfectly flat boundaries, a solution is sought for a wave guide whose upper, pressure-release boundary is given some roughness and allowed to move, in order to begin to understand the effects that ocean surface waves have on shallow water acoustic propagation.

The surface wave field is assumed to be a linear superposition M of sinusoidal components, and is zero-mean in space and time:

$$\eta(\mathbf{r}, t) = \sum_{m=1}^{M} a_m \cos(\boldsymbol{\kappa}_m \cdot \mathbf{r} - \sigma_m t + \gamma_m) \tag{2.24}$$

$$\kappa_m = |\boldsymbol{\kappa}_m| = (\kappa_{m_x}^2 + \kappa_{m_y}^2)^{1/2} \tag{2.25}$$

where a_m is amplitude and γ_m is the phase offset of the m^{th} component. The wavenumbers $\boldsymbol{\kappa}_m$ have horizontal components κ_{m_x} and κ_{m_y}, and, with frequencies σ_m obey the linear wave dispersion relation (Eq. 2.1).

The scalar acoustic pressure field is expanded in a perturbation series in small parameter kh, where $k = \omega/c$ is the acoustic wavenumber:

$$\widetilde{\psi} = \sum_{n=0}^{\infty} \frac{(kh)^n}{n!} \widetilde{\psi^{(n)}} \tag{2.26}$$

With the surface allowed to deviate from flat, the upper, pressure-release boundary condition is maintained as a Taylor expansion about $z = 0$ of the pressure field.

$$\psi(\mathbf{x}, z_s, t) = \sum_{n=0}^{\infty} \frac{\eta^n(\mathbf{r}, t)}{n!} (\frac{\partial}{\partial z})^n \psi(\mathbf{x}, z_s, t) \,|_{z=0} \tag{2.27}$$

which, after transformation into the frequency domain via Eq. 2.12, becomes

$$\widetilde{\psi}(\mathbf{x}, z_s, \omega) = \sum_{n=0}^{\infty} \frac{\widetilde{\eta^n}(\mathbf{r}, \omega)}{n!} \otimes (\frac{\partial}{\partial z})^n \widetilde{\psi}(\mathbf{x}, z_s, \omega) \,|_{z=0} \tag{2.28}$$

where $\otimes$ denotes convolution in temporal frequency. It should be noted that $\widetilde{\eta^n}(\mathbf{r}, \omega)$ is the Fourier Transform of the n^{th} power of the surface wave height $\eta^n(\mathbf{r}, t)$,

$$\widetilde{\eta^n}(\mathbf{r}, \omega) = \int_{-\infty}^{\infty} d\omega \, e^{-i\omega t} \eta^n(\mathbf{r}, t) \tag{2.29}$$

and as such is the n^{th} convolution in frequency of the surface wave spectrum. Inserting Eq. 2.24 into Eq. 2.29 yields

$$\widetilde{\eta}(\mathbf{r}, \sigma) = \sum_{m=1}^{M} \frac{a_m}{2} [e^{i(\boldsymbol{\kappa}_m \cdot \mathbf{r} + \gamma_m)} \delta(\sigma - \sigma_m) + e^{-i(\boldsymbol{\kappa}_m \cdot \mathbf{r} + \gamma_m)} \delta(\sigma + \sigma_m)] \tag{2.30}$$

Equations 2.15 and 2.16 allow for grouping of terms by order of kh in expansions 2.26 and 2.28. The result is a series of boundary value problems describing the scattered and Doppler-shifted pressure field. The order $(kh)^0$ problem is

$$\begin{aligned} \nabla_H^2 \widetilde{\psi}^{(0)}(\mathbf{x}, z_s, \omega) + [\rho(z) \frac{\partial}{\partial z} \frac{1}{\rho(z)} \frac{\partial}{\partial z} - k^2] \times & \\ \widetilde{\psi}^{(0)}(\mathbf{x}, z_s, \omega) &= S_\omega \delta(\mathbf{x} - \mathbf{x_s}) e^{-i\omega_\circ t - i\gamma_\circ} && (2.31) \\ \widetilde{\psi}^{(0)}(\mathbf{x}, z_s, \omega) &= 0 \,|_{z=0} && (2.32) \end{aligned}$$

plus the appropriate bottom boundary condition. Equations 2.31 and 2.32 are identical to the unperturbed problem in Eqs. 2.14 and 2.22, and thus have the solution detailed in Eq. 2.23:

$$\begin{aligned} \widetilde{\psi}^{(0)}(\mathbf{x}, z_s, \omega) &= \sum_{n=1}^{\infty} \Psi_n^{(0)}(z, \omega) \Phi_n^{(0)}(r, z_s, \omega) && (2.33) \\ \Phi_n^{(0)}(z, z_s, \omega) &= \frac{iS_\omega}{\rho_\circ} \Psi_n(z_s, \omega) H_0(k_{n_r}^{(0)} r) \delta(\omega - \omega_\circ) && (2.34) \end{aligned}$$

where, as in the unperturbed problem, the horizontal and vertical wavenumber components are related geometrically, $k_{n_r}^{(0)\,2} = k^2 - k_{n_z}^{(0)\,2}$.

The set of boundary value problems for order $(kh)^n$ for all $n \geq 1$ take the form

$$\begin{aligned} \nabla_H^2 \widetilde{\psi}^{(n)} + [\rho \frac{\partial}{\partial z} \frac{1}{\rho} \frac{\partial}{\partial z} - k^2] \widetilde{\psi}^{(n)} &= 0 && (2.35) \\ \widetilde{\psi}^{(n)} &= \sum_{m=1}^{n} \frac{(kh)^{n-m}}{(n-m)!} \frac{\widetilde{\eta^m}}{m!} \otimes \frac{\partial^m}{\partial z^m} \widetilde{\psi}^{(n-m)} \,|_{\,z=0} && (2.36) \end{aligned}$$

plus the appropriate bottom boundary condition. Once again the $\otimes$ denotes convolution in temporal frequency, and D is the ocean wave guide depth, h is RMS surface wave height, and $k = \omega/c$ is acoustic wavenumber. These problems all submit a solution that takes the form of Eq.2.17 in that they can be separated into horizontal ($\mathbf{r}$) and vertical (z) parts.

$$\widetilde{\psi}^{(n)}(\mathbf{x}, z_s, \omega) = \sum_{m=1}^{M} \Phi_m^{(n)}(\mathbf{r}, z_s, \omega) \Psi_m^{(n)}(z, \omega) \,+\, \int_0^\infty d\zeta \bar{\Phi}^{(n)}(\mathbf{r}, z_s, \zeta, \omega) \bar{\Psi}^{(n)}(z, \zeta, \omega) \tag{2.37}$$

From Eq. 2.30, it is apparent that the n^{th} term of the perturbation expansion (Eqs. 2.26 and 2.27) introduces a scattered sideband whose width in temporal frequency is n-times the width of the surface wave spectrum, and whose peak is located $\pm n$-times the peak frequency of the surface wave spectrum from the acoustic carrier frequency. Harper and Labianca[HL75a] and Pourkaviani and Willemsen[PW91] showed that, when the full 3-dimensional problem is addressed, the width of the spatial spectrum of the received n^{th} contribution of the perturbational terms is n-times the width in wavenumber space as the ocean surface wavenumber spectrum. For the current work, however, only the 0^{th} and 1^{st} terms will be explored.

Some insight into the Doppler-shifted, scattered portion of the received spectrum arises form examining the order $(kh)^1$ terms of the expanded series. In perturbation theory, the surface waves' influence on the acoustic field enters through the upper boundary condition. Writing the upper boundary condition for the order $(kh)^1$ problem (Eq. 2.36) and inserting the random surface wave spectrum (Eq. 2.30), the first order contribution $\widetilde{\psi}^{(1)}$ of the scattered field to the total received acoustic pressure becomes

$$\begin{aligned}\widetilde{\psi}^{(1)}(\mathbf{x}, z_s, \sigma) = \sum_{m=1}^{M} \frac{a_m}{2}[e^{i(\boldsymbol{\kappa}_m\cdot\mathbf{r}+\gamma_m)}\delta(\sigma-\sigma_m)+ \\ e^{-i(\boldsymbol{\kappa}_m\cdot\mathbf{r}+\gamma_m)}\delta(\sigma+\sigma_m)] \otimes_\sigma \frac{\partial}{\partial z}\widetilde{\psi}^{(0)}(\mathbf{x}, z_s, \sigma)|_{z=0}\end{aligned} \tag{2.38}$$

Then, inserting Eqs. 2.33 and 2.34 and writing out the convolution integral, Eq. 2.38 becomes

$$\begin{aligned}\widetilde{\psi}^{(1)}(\mathbf{x}, z_s, \sigma) = \int_{-\infty}^{\infty} d\sigma' \sum_{m=1}^{M}\sum_{n=1}^{N} \frac{S_\omega a_m}{i8}[e^{i(\boldsymbol{\kappa}_m\cdot\mathbf{r}+\gamma_m)}\delta(\sigma'-\sigma_m)+ \\ e^{-i(\boldsymbol{\kappa}_m\cdot\mathbf{r}+\gamma_m)}\delta(\sigma'+\sigma_m)]\frac{\partial}{\partial z}\Psi_n^{(0)}(k_{n_z}^{(0)}z_s)H_0(k_{n_r}^{(0)}r)\delta(\omega_\circ-\sigma-\sigma')|_{z=0}\end{aligned} \tag{2.39}$$

It is apparent in Eq. 2.39 that the first order perterbation contribution to the total received pressure $\widetilde{\psi}$ gives rise to a Doppler-shifted version of the original acoustic signal. If the asymptotic form of the Hankel function $H_0(kr) \simeq \sqrt{\frac{2}{\pi kr}}e^{ikr-i\pi/4}$ is used, then the Bragg condition also becomes obvious in this setting.

$$\begin{aligned}\widetilde{\psi^{(1)}}(\mathbf{x}, z_s, \sigma) \simeq \sum_{m=1}^{M}\sum_{n=1}^{N}\frac{S_\omega a_m}{i8}\frac{\partial}{\partial z}\Psi_n^{(0)}(k_{n_z}^{(0)}z_s)e^{-i\pi/4}\times \\ \sqrt{\frac{2}{\pi k_{n_r}^{(0)}r}}[e^{i(\boldsymbol{\kappa}_m\cdot\mathbf{r}+k_{n_r}^{(0)}r+\gamma_m)}\delta(\sigma-\omega_\circ-\sigma_m)+ \\ e^{-i(\boldsymbol{\kappa}_m\cdot\mathbf{r}-k_{n_r}^{(0)}r+\gamma_m)}\delta(\sigma-\omega_\circ+\sigma_m)]|_{z=0}\end{aligned} \tag{2.40}$$

If the surface wavenumbers $\boldsymbol{\kappa}_m$ are decomposed into components parallel and perpendicular to the vertical plane of propagation between source and receiver, $\kappa_{m_\perp}$ and $\kappa_{m_\parallel}$, respectively, and the search for distorted signals is limited to within this vertical plane (thereby paralleling Sir Rayleigh's and others' work in this field[For70, WJ95]), then the Bragg condition becomes

$$\mathbf{k}_{n,m} = \mathbf{k}_n \pm \boldsymbol{\kappa}_m \tag{2.41}$$

where $\mathbf{k}_n$ is the wavenumber vector for the n^{th} propagating mode and $\boldsymbol{\kappa}_m$ is the m^{th} surface wave component. The in-plane component of Eq. 2.41 is

$$k_{\parallel n,m} = (k_{r_n} \pm \kappa_\parallel)\hat{r} + k_{n_z}\hat{z} \tag{2.42}$$

which is the origin of Eq. 2.7 and gives the basis for searching for Doppler-shifted, scattered sidebands in the vertical acoustic arrival structure. The Doppler shift associated with these wavenumbers will be $\pm\sigma_m$ (Eq. 2.40). In the vertical plane of acoustic propagation, scattering off surface waves will give rise to received acoustic signals whose horizontal wavenumber component has been offset from the original. Vertical beamformer output will reflect this as a vertical deviation in received angle of arrival. Of course, Eq. 2.40, taken in 3 spatial dimensions, predicts horizontal angle deviations associated with these Doppler shifted signals, and this has been previously demonstrated [LS04, LBD08]. In order to address the fully 3-dimensional problem at higher orders, transform techniques have been applied by some authors[HL75a]. Few observational or experimental studies have been done to verify these concepts, as the equipment and logistical demands to perform such work are prohibitively difficult.

It should be noted that perturbational theory relies on the premise that the perturbation parameter, which in this work is kh, is much less than 1. When kh becomes large enough that raising it to higher powers does not diminish, in effect the different ordered equations become coupled, and independent solution is not possible. This is important in scattering acoustics since surface wave heights are in general variable, and these changing conditions may lead to breakdown in the ability to predict or understand measurements.

2.5 Discussion

Examination of the plane-wave vertical beamformer during varying ocean surface wave conditions shows clear dependence of the Doppler-shifted Bragg scattered contributions to the total received acoustic field on the entire directional surface wave spectrum. Variation in directionality within a single surface wave spectrum gives rise to dramatically different scattering directions at the receiving array, given a fixed source position. Additionally, the received scattered field depends on each individual acoustic mode comprising the total received, non-scattered field. Difference in scattering angles are seen for different modes at the same frequency, at the same time. The ability to observe these phenomena requires instrumentation to record the full directional surface wave spectrum, since in open ocean experiments the local surface wave field is not just subject to local weather, but it is also influenced by distant swell systems.

In the theory summarized in Section 2.4 and in the measurements presented in Section 2.3.3 it is clear that the results of the Bragg condition (Eq. 2.6) become more pronounced when the horizontal acoustic and ocean surface wavenumber magnitudes are more comparable, when viewing the relationship as a function of angle, as in beamforming. In the shallow, iso-speed waveguide and with the surface wave fields observed during the experiment, this relationship is shown both through the dependence of scattering on acoustic frequency and on vertical angle of arrival. The horizontal acoustic wavenumber decreases with frequency, and with increased steepness of arrival, bringing its magnitude closer to that of the observed ocean surface waves, whose wavenumber magnitude is related to temporal frequency through the linear dispersion relation (Eq. 2.1). The net effect of decreasing the horizontal acoustic wavenumber in the context of the Bragg condition is an increase in the vertical angle deviations observed in the vertical beamformer output. The scattered angle's dependence on acoustic frequency would masked, had the data in Figs. 2.6 and 2.7 been presented as scattered intensity vs. frequency f and horizontal wavenumber k.

Observed amplitudes of the scattered sidebands do not follow any simple dependence on surface wave height or frequency, or acoustic frequency or arrival angle. Though perturbation theory predicts the sideband amplitudes (Eq. 2.39), the observed sideband amplitudes were inconsistent (Figs. 2.6 and 2.7). Similar discrepancies have been observed by previous authors[LS04, LBD08].

While the results of Section 2.3.3 show vertical beamformer output and Eq. 2.8 relates the observed sidebands to specific surface wave interactions, the ability to invert the results for the surface wave field still relies on the receiving array having horizontal aperture. While a vertical array could be used to perform similar analyses as have been shown in Sect. 2.3.2, a purely vertical array will be limited by its inability to resolve horizontal angles and the conical ambiguity will result in azimuthally integrated measurements of scattered acoustic energy. That being said, any array that can resolve vertical angles of arrival and whose beam can be confidently steered azimuthally towards a known, stationary source location can be used to unambiguously invert the received beam pattern for the ocean surface wave spectrum using Eqs. 2.8 and 2.1.

If the scattering is strong, and higher order terms in Expansions 2.26 and 2.27 become important in the full pressure field solution, or if multiple interactions with the surface lead to increased levels of higher order sidebands, then the ability to invert measured acoustic field for the surface waves becomes difficult, since the higher order $(kh)^n$ terms ($n \geq 2$) introduce multiple convolutions of the ocean surface wavenumber and temporal spectra into the total acoustic field. While there is the possibility to perform such an inversion using a full, 3-dimensional spatial search at known Doppler-shifted frequencies (for example using independent measurements of the surface wave temporal spectrum), previously explored methods[LS04, LBD08, WJ95, WJ93] may be insufficient in these circumstances.

Of considerable interest in scattering acoustics is the ability to perform the inverse problem: to deduce environmental parameters from acoustic measurements. Wild and Joyce[WJ95] proposed inverting received narrowband tones for the surface wave spectrum using a moving source or receiving array, and produced simulated results that showed promise. In a shallow environment, this ability is complicated somewhat by bottom roughness, unless the source and receiver are stationary, since bottom roughness can produce similar results as the surface waves when the acoustic system is moving [Mar63]. Results presented by Lebedev and Salin[LS04] and Lynch et al.[LBD08], as well as the results presented in Section 2.3.3, along with the predictions of Section 2.4 produce an opportunity accomplish an inversion of received narrowband transmissions using a fixed source and fixed receiving array by examining the beam output of the received signal. While Lebedev and Salin[LS04] showed that, with 2 measured, Doppler-shifted sidebands in the horizontal beamformer output, the surface wave peak frequency and direction could be measured. These results were dependent on both the positively and negatively Doppler shifted sidebands being visible. This is generally true, unless the search through acoustic wavenumber space of the Doppler shifted signal is performed in three dimensions. Otherwise, in a 2 dimensional search, a single sideband leaves an ambiguity in the Bragg condition where the surface wavenumber vector κ is sought. Nonetheless, the results presented in this paper demonstrate that the full surface wave spectrum can be deduced from observations of Doppler-shifted scattering from a rough, moving surface.

2.6 Conclusions

Plane-wave beamformer output in the vertical plane shows scattered sidebands whose frequency displacements coincide with frequencies of measured surface wave spectra. Measured vertical angle deviations from the vertical arrival angles of the measured non-Doppler-shifted propagating acoustic modes agree with predictions of Bragg scattering and Doppler shifting from first-order perturbation theory.

Chapter 3

First-order scattering in the horizontal plane, higher order scattering and multiple interactions with the surface

3.1 Abstract

During an experiment just outside the surf zone, a bottom-moored source transmitted eight low-frequency (< 700 Hz) tones to two nearly perpendicular, bottom-lying hydrophone arrays 1.25 km away. Surface gravity waves were measured using an on-site pressure sensor and a directional pressure sensor network deployed 40 km away and maintained by the Coastal Data Information Program (CDIP). Received omnidirectional spectra of the acoustic tones show dependence on the ocean surface wave spectra, exhibiting a broadening that is wider band than the surface wave spectra, with harmonic-like sidebands spaced at regular intervals equal to the peak frequency of the surface waves. Beamformer output shows Doppler-shifted sidebands asymmetrically offset from the direction of the sound source, suggestive of Bragg scattering by surface waves. Increased levels of higher order sidebands during smaller surface wave conditions suggest that higher order scattering does

not wholly explain the distortion mechanism behind the observed distortions. A simplified phase modulation model is developed that incorporates multiple surface interactions and reproduces some of the features of the observed omnidirectional spectra.

3.2 Introduction

Acoustic tones recorded during an experiment off the Southern California coast showed significant variability that depended heavily on the prevailing ocean surface wave activity (Fig. 3.1). Incoherently averaged acoustic spectra contained sidebands that very much mimicked the measured surface wave spectrum (Figs. 3.2 and 3.3). Moreover, additional sidebands, spaced evenly by integer multiples of the surface wave peak frequency, also were observed. Curiously, the sidebands' levels did not always decrease with decreasing ocean wave activity as might be expected from perturbation theory[PW91]. Rather, at times they persisted out to at least 3$^{\mathrm{rd}}$ order during quiescent wave conditions (Fig. 3.3), suggesting multiple interactions between the rough, moving surface and the perturbed acoustic field. Additionally, through the use of the horizontal array deployed on the ocean bottom, out-of-plane scattering of Doppler-shifted side lobes was observed, indicating Bragg scattering (Fig. 3.4). Clearly, the relatively long propagation (1.25 km) through this very shallow (10 m) waveguide results in extensive interaction of the acoustic field with the ocean surface, causing a variety of received signal variations as a function of ocean roughness conditions.

In this paper, a relationship is sought between this observed temporal and spatial frequency broadening of narrowband acoustic tones and the spectrum of ocean surface waves. The observed broadening in temporal frequency exceeds that expected from first-order pressure field perturbation theory[Chu78, Par71, HL75a], including Bragg scattering [LS04]. Higher order scattering[HL75b, PW91] can lead to broader distortion of received narrowband acoustic tones, and even harmonic-like sidebands, and this possibility is explored through the implementation of numerical models as an explanation of the data obtained from this very shallow water experiment. Additionally, a simplified model for higher order scattering including multiple interactions with the moving surface is proposed that can predict received omnidirectional field given any surface wave field by modeling the surface motions as a mechanism of acoustic path length modulation. The modulation of acoustic phase by a surface wave-induced time dependence of the acoustic path length (and therefore the travel time) results in a potentially complicated spectrum due to non-linear behavior (with respect to surface deviations), and can result in a frequency spectrum that is broader than that of the modulating phenomenon, and can easily incorporate multiple interactions with the moving ocean surface.

The ocean's dynamics impart fundamental performance limits on many acoustics-based systems, including passive synthetic aperture [DTC^{+}06] and communications [PD04] systems. Surface motions distort signals by randomizing propagation conditions, rendering impossible a deterministic characterization of these acoustic effects in most applications. A considerable body of work exists in the theoretical development and numerical modeling of the problem of acoustical interaction with a rough, moving surface. Previous efforts to map surface wave statistics into received acoustic spectra have employed various mathematical methods, mostly based on perturbation expansions of pressure field contributions [WJ95, Gra03], or small slope approximations[TB95]. Whereas some approaches begin with a perturbation of the total acoustic field[HL75a] and take into account the relative source and receiver configuration, others remain more general and examine the perturbation of a single, generic plane wave [PW91].

Some modeling methods have focused on broadband acoustic propagation [MHDC03], but many more methods center on modeling narrowband acoustics. Transmission of narrowband tones is a useful platform for the purpose of inversion for surface activity, in that the initial delta-function spectrum is convenient mathematically, especially when investigating a process such as the ocean surface, which can have such a wide range of spatial and temporal behavior. Other investigators have employed a more brute-force method of marching modified versions of existing, ideal waveguide propagation models through a series of frozen, rough surfaces[Ros99].

Wild and Joyce [WJ95] propose using received acoustic signals to invert for surface wave spectra, and they construct a series of experimental scenarios with varying motion of the receivers relative to the wind and dominant surface wave direction as input for their model . Their approach is based on first-order perturbation. Gragg[Gra03] carries the perturbation to 2^{nd} order in order to derive analytically the influence of the surface wave field on the cross-spectral density matrix (CSDM) for beamforming and other related analysis algorithms. Rosenberg[Ros99] takes a different approach of modifying a parabolic equation propagation model to account for a rough surface, and introducing surface motions directly into modeled acoustic data by way of a series of frozen surface approximations. This approach reproduces some interesting aspects of their recorded data, namely harmonic-like sidebands centered at integer multiples of the surface wave frequency.

Much of the work on observation of forward scattering from a moving boundary has concentrated on high acoustic frequencies ($>$ 1000 Hz)[McD92, Dah96, Uri83]. Lower frequency investigations have either concentrated on incoherent effects[Chu78], or have depended on very specific source-receiver geometries with respect to the ocean surface wave field[LS04]. While considerable progress has been made in developing favorable comparisons between models of acoustic interaction with surface waves and measurements in controlled laboratory settings[TD05], much work remains to be done in examining open ocean observations. Several authors have shown in observations that interaction of acoustic waves with the moving ocean surface affects the received narrowband acoustic transmissions such that the received acoustic spectrum includes a replication of the moving surface's spectrum in the form of side-bands [HL75b, Chu78, LS04, Wil73], or, equivalently, that the received acoustic spectrum is a convolution of the transmitted acoustic spectrum with the ocean surface waves' spectrum [Par71]. Commonly, these results are related to the surface wave spectrum by applying first-order perturbation theories. In some instances, the acoustic sidebands are narrower band than the ocean wave spectrum [Chu78, LS04]. Azimuthal scattering with Doppler shift also has been modeled successfully[WJ95] using first order perturbation techniques, and has been observed by other authors[LS04].

The present work's analytical approach is similar to those previously mentioned in that a small ocean surface wave approximation is made, but differs in that, in general, no redirection of acoustic energy occurs in the mechanism of Doppler shift. A simplification is presented here that approximates all higher order acoustic scattering as arriving in the specular direction. This approach admits to a ray solution, with a flat surface approximation: all ocean surface wavenumbers are approximated as zero while surface wave frequencies remain finite, so that the flat, pressure-release upper boundary moves as the ocean surface wave temporal spectrum. The modeling of phase modulation in this paper is similar to the modeling effort of Rosenberg[Ros99] in the use of a series of frozen surfaces to introduce surface motions into the waveguide. However, whereas a parabolic equation solver was used before, a ray-based propagation model is used in the model here. Also, whereas other authors have often successfully employed analytically derived expressions for surface wave fields based on wind speeds in their studies of acoustical interaction with a rough, moving surface, the measurement of surface wave conditions over the course of the experiment reported here shows clearly that these analytically derived surface wave spectra are not applicable. In particular, the experiment setting and surface wave fields do not fit several of the assumptions that these derivations require, such as fully developed seas or uniqueness of surface wave-generating systems. Therefore only measured surface wave spectra are included in the modeling efforts presented in this paper.

Some of the features of these data have not been otherwise observed. For example, while the multiple, harmonic-like sidebands observed in the experiment here are similar to those observed by other authors[Ros99], they are different in their persistence during times when the surface waves were smaller and lower frequency (Fig. 3.3). In addition, the number of sidebands is higher than previously observed. Instrumentation deployed in this experiment and measurement over an extended period where ocean surface conditions varied dramatically lend themselves to further insight into the dependence of received low-frequency acoustic fields on oceanographic conditions.

The goal of this paper is to develop a mapping of the statistics of the ocean's surface dynamics into the received underwater acoustic spectrum in shallow water environments, given limited environmental measurement, and to compare predictions from physical models of this mapping with recorded data from a real ocean setting. Presented in this paper are data obtained from an ocean experiment showing multiple manifestations of frequency spreading by interaction with surface waves. An acoustic model incorporating higher order scattering and multipath propagation including multiple interactions with the moving surface is developed in order to explain some of the more curious features of the observations. In Sect. 3.3, a general derivation for spectral broadening of received acoustic fields by interaction with ocean surface waves in single path and multi-path environments is given. Following this derivation is an overview of perturbational scattering theory. Numerical models are introduced using these concepts. In Sect. 3.4, the experiment during which the measurements were made for this study is described, followed by presentation of data analysis results in Sect. 3.5. In Sect. 3.6, results from this experiment are compared to predictions of numerical models based on those spectrum-broadening mechanisms presented in Sect. 3.3. Section 3.7 is a comparative discussion of the theories explored here, in relation to the preceding experimental and numerical observations. Finally, a summary of the conclusions from this work is discussed in Sect. 3.8.

3.3 Analytical Approach

The commonly understood idea of Doppler shift, in which a received signal's frequency is shifted due to either a moving source or moving receiver, is extended to include any frequency shift that results from time dependence of the acoustic path. This generalized formulation of Doppler shift is then used as the basis for a simplified model of higher order acoustic scattering in an environment with multipath propagation. A general mathematical construct is sought to explain Doppler broadening of acoustic tones by the motion from surface gravity waves, in particular, when higher order sidebands' levels remain high in small surface wave conditions.

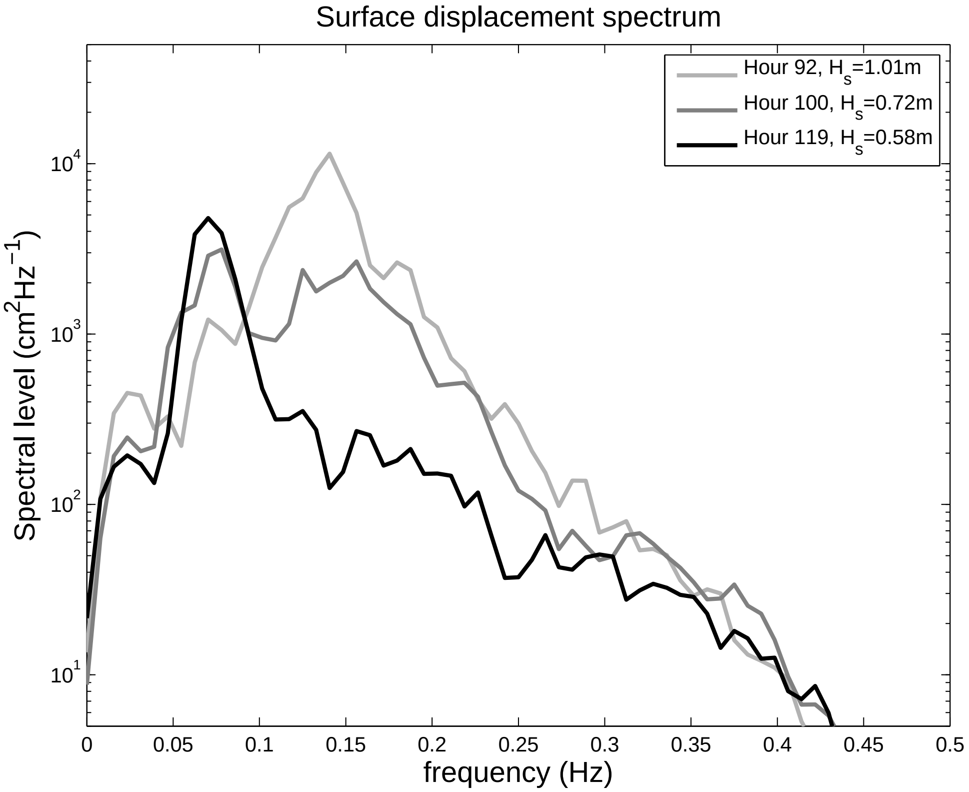

Figure 3.1: Ocean surface wave height (vertical displacement, cm) spectra at three different times during the experiment.

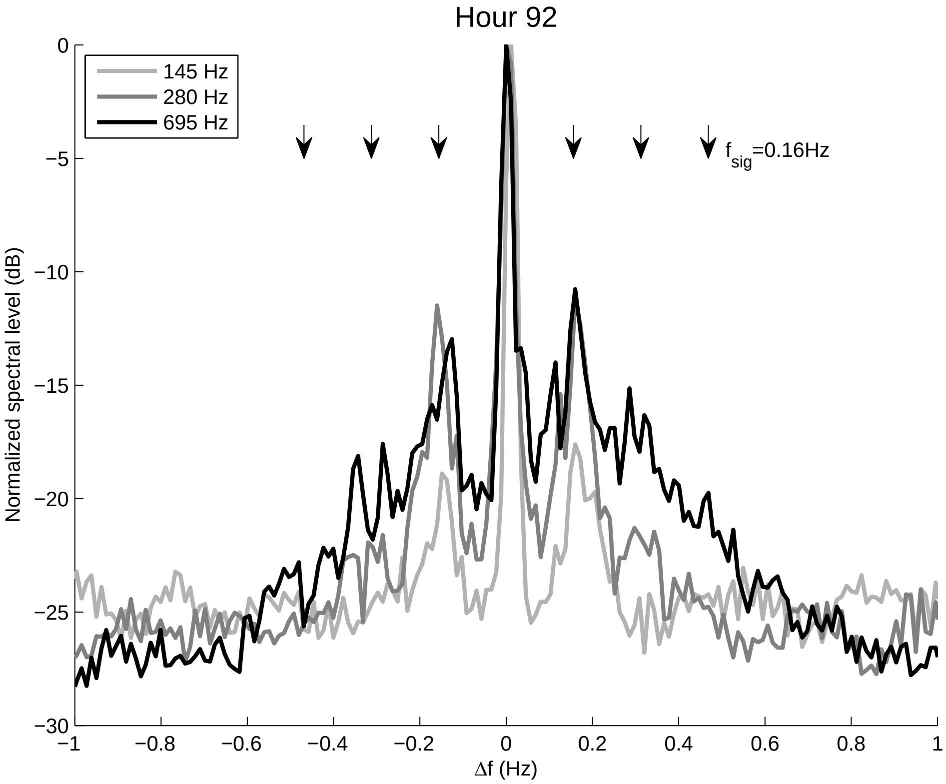

Figure 3.2: The measured omnidirectional acoustic spectra at three different frequencies during a large wind-wave event. The horizontal axis quantity Δf is the offset from the acoustic tone frequency $f_\circ$. The peak period of the ocean surface waves at this time was approximately 7 seconds (f_{sig} ∼.16 Hz) with a significant wave height H_s of approximately 1.0 m (re: Fig. 3.1, light gray trace). Arrows indicate locations of integer-multiples of the peak surface wave frequency.

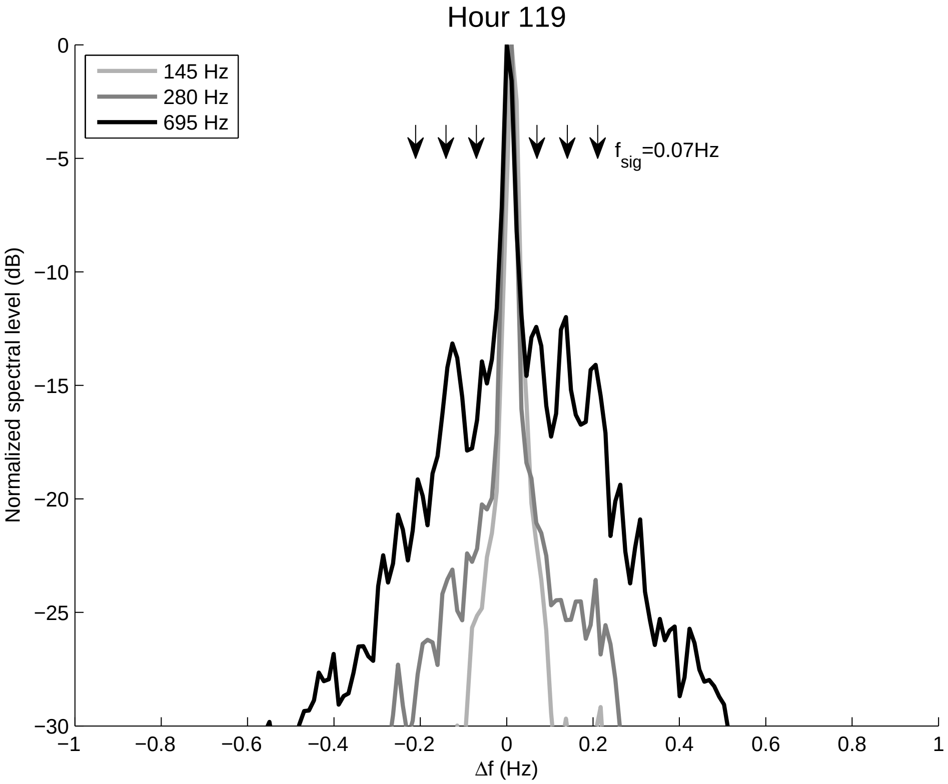

Figure 3.3: The measured omnidirectional acoustic spectra from a period when only a small, long-period swell ($H_s \sim .6m$) was present (re: Fig. 3.1, black trace). Arrows indicate locations of integer-multiples of the peak surface wave frequency.

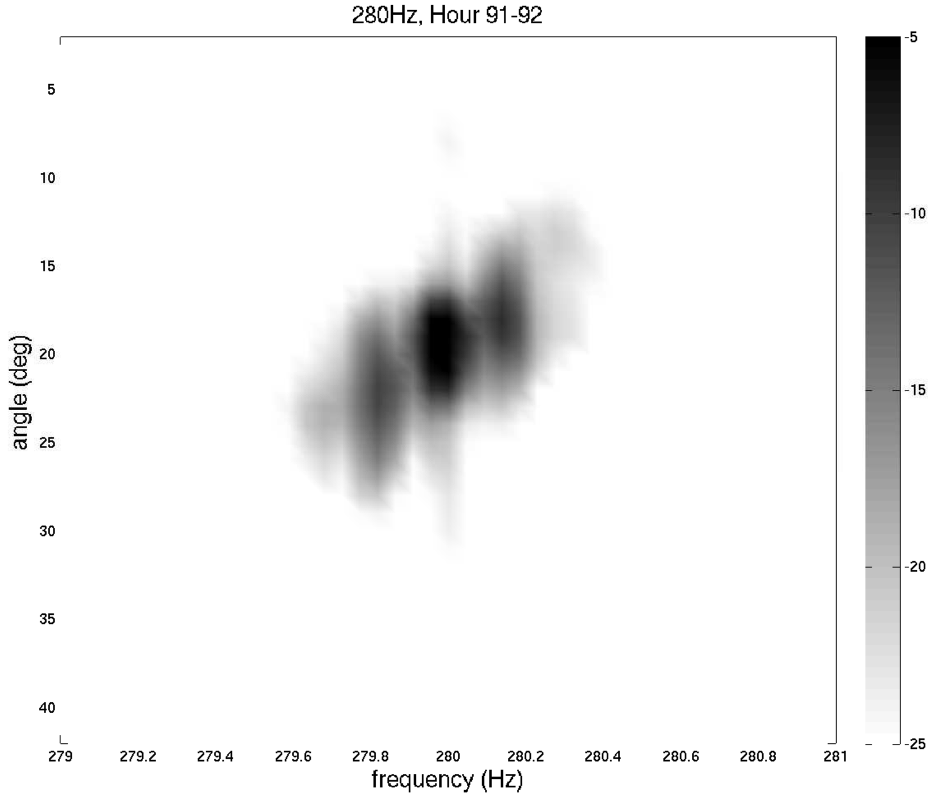

Figure 3.4: Horizontal angle dependence of Doppler-shifted acoustic spectrum at 280 Hz suggests Bragg scattering. The directional spectra (dB) are computed using data from the broadside array, and are normalized to the peak located in the direction of the source, with zero frequency offset.

3.3.1 First order perturbation and Bragg scattering

First order perturbation[Chu78, Par71, HL75b] of the acoustic field by surface waves results in the scaled convolution of the surface wave spectrum with the narrowband acoustic spectrum, and is equivalent to an amplitude (linear) modulation of the pressure field by the surface waves. Then perturbed modes' amplitudes are a function of the surface displacement, a time-dependent function, and the result is an incoherent, Doppler-shifted contribution to the received spectrum. It should be noted that, without the motion of the surface – if the surface could be frozen – no frequency shift would occur, though out-of-plane and/or non-specular scattering is still would be present.

There is also a component of the horizontally deflected, surface-scattered contribution to the received pressure field resulting from Bragg scattering. Scattering from a moving corrugated surface within an area that is located such that constructive interference occurs at the receiver array will result in a relatively large arrival with a Doppler shift, and can appear in beamformer output as a pair of signals shifted symmetrically in frequency, but generally asymmetric in amplitude and in deviation in angle from the original source. The additional phase evolution of the scattered acoustic signal from adjacent peaks and/or troughs in the ocean surface wave field results in constructive or destructive interference, depending on the scattering site and the wavelength of the sound. Only certain regions will result in a Doppler shifted signal at the receiver. The incident and scattering angles associated with these regions are related by

$$\boldsymbol{k_s} = \boldsymbol{k_i} \pm \boldsymbol{\kappa} \tag{3.1}$$

where $\boldsymbol{k_s}$ and $\boldsymbol{k_i}$ are the scattered and incident horizontal acoustic wavenumber vectors, respectively, and $\boldsymbol{\kappa}$ is the wavenumber vector of the dominant ocean wave, whose magnitude and associated frequency are related through the dispersion relation

$$\sigma^2 = g\kappa \tanh(\kappa H). \tag{3.2}$$

Here σ is the frequency of the ocean wave in radians per second, g is the gravitational acceleration (~ 9.8 m s^{-2}), H is the depth (m) of the ocean in the region of interest, and $\kappa = |\boldsymbol{\kappa}|$ (rad m^{-1}). From Eq. 3.1 the dependence of the scattered wavenumber on acoustic frequency and geometry (via the acoustic wavenumber, $\omega = c|\boldsymbol{k}|$) is apparent.

Equation 3.1 in the x- (EW) and y- (NS) components of the horizontal wavenumbers can be rewritten in terms of the magnitudes k and directions θ of the acoustic wavenumbers. These equations are transcendental in ϕ_w, the direction of propagation of the surface wave, unless they can be simplified by some assumptions relating the relative sizes or directions of the constituent wavenumbers $\boldsymbol{k_s}$, $\boldsymbol{k_i}$, or $\boldsymbol{\kappa}$. Assuming low surface grazing angles [LS04], where $|\boldsymbol{k_s}| \sim |\boldsymbol{k_i}| \sim k = \frac{2\pi}{\lambda}$ (λ is the acoustic wave length), the angle of surface wave propagation ϕ_w can be found using the measured offset angles $\theta_s^{\pm}$ of the acoustic sidebands (the + and - signs correspond to up-shift and down-shift in frequency, respectively):

$$\phi_w = \frac{\pi}{2}\,\mathrm{sgn}(\theta_s^{+}) + \frac{\theta_s^{+} + \theta_s^{-}}{2}. \qquad (3.3)$$

The amplitude of the scattered signal relative to the transmitted signal amplitude is determined by the size of the first Fresnel zones. The magnitude of the acoustic sidebands created by Bragg scattering depends on several geometric components, including the depth H of the acoustic waveguide, the source-to-receiver distance, the size of the resonant scattering area, the acoustic wavelength λ, and the distances from the scattering area to the source and receiver. Acoustic frequency impacts the amplitude of the Bragg-scattered sidebands through the interference pattern it creates. The sizes of the Fresnel zones also depend on the geometry of the experimental set-up through the horizontal distances from source to the scattering patch and from the scattering patch to the receiver. The locations of the scattering patches will change with the direction of propagation of the ocean surface waves. The reader is referred to Lebedev and Salin[LS04] for a complete treatment of the Bragg scattering amplitude and angle.

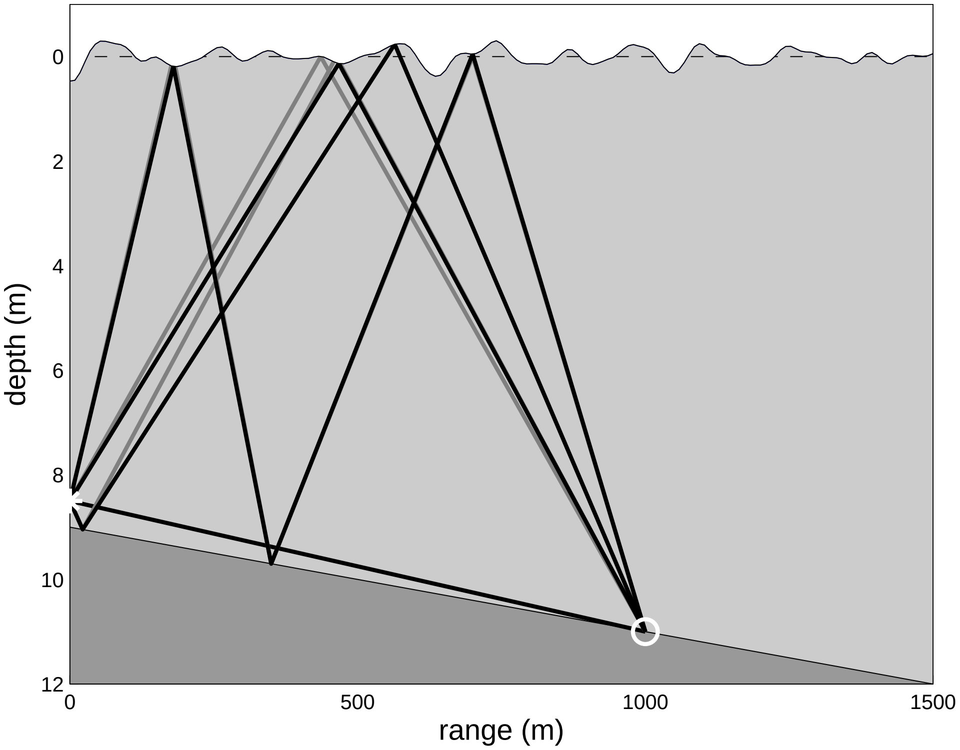

Figure 3.5: Ray paths from a near-bottom source to a bottom receiver in a range-dependent waveguide that approximates the conditions of the experiment. In this study, the ocean surface is modeled as a moving reflector.

3.3.2 Phase modulation by acoustic path length fluctuation

In the high frequency limit, the received acoustic signal on a single hydrophone $p_{\text{rcv}}(t)$ can be written as the sum of pressure contributions traveling along rays connecting the hydrophone to the source.

$$p_{\text{rcv}}(t) = \sum_{k=1}^{N_{\text{rays}}} A_k p_{\text{src}}(t - \tau_k) \tag{3.4}$$

Here the travel time for k^{th}eigenray is τ_k, and A_k is its amplitude that takes into account reflection coefficients, geometric spreading, and attenuation, and it has been assumed that the ocean surface is flat and perfectly reflecting. The phase $\Theta_\circ$ of an acoustic source that creates a sinusoidal signal at temporal frequency $\omega_\circ$ is

$$\Theta_{\text{src}}(t) = \omega_\circ t + \Theta_\circ(\omega_\circ) \tag{3.5}$$

where $\Theta_\circ(\omega_\circ)$ is the phase at time $t = 0$ of the signal with frequency $\omega_\circ$. Assuming propagation in a homogenous waveguide with a flat pressure-release surface and a rigid bottom, the phase at the hydrophone receiving this signal propagating along ray path k will be

$$\Theta_{\text{rcv},k}(t) = \omega_\circ(t - \tau_k) + \Theta_\circ(\omega_\circ) + m_k\pi \tag{3.6}$$

Here the initial phase is $\Theta_\circ$, m_k is the number of reflections off the pressure-release surface and time is t. In a shallow water waveguide, rays connecting a source and receiver can interact with the surface and bottom several times (Fig. 3.5). The travel time τ_k that it takes for the signal to travel along ray path k from the source to the receiver is dependent on the separation of the source and receiver, as well as the medium sound speed along the path.

$$\tau_k = \int_{s_1}^{s_2} \frac{ds}{\boldsymbol{v}(s)\cdot \hat{\boldsymbol{s}}(s) + c(s)} \tag{3.7}$$

The positions of the source and receiver along the ray path are s_1 and s_2, respectively, the sound speed is c, the velocity of the fluid at points along the ray path is $\boldsymbol{v}$ and the direction of the ray path (i.e. acoustic propagation direction) is given by the unit vector $\hat{\boldsymbol{s}}$. If s_1, s_2 and the medium motion $\boldsymbol{v}(s)$ are all time-dependent, then the travel time τ_k that an acoustic signal takes to propagate from the source to the hydrophone along ray path k also becomes time-dependent:

$$\tau_k(t) = \int_{s_1(t)}^{s_2(t)} \frac{ds}{\boldsymbol{v}(s,t)\cdot\hat{\boldsymbol{s}}(s) + c(s)} \tag{3.8}$$

where s is the path length parameter, or distance along the ray path.

Time dependence of the positions of the source or receiver (s_1 or s_2), or time dependence of the motion of the medium ($\boldsymbol{v}$) leads to time dependence in the acoustic travel time, and ultimately leads to a variation in the received signal's phase. The receiving hydrophone records this variation as a shift in the frequency ω_k from the frequency $\omega_\circ$ emitted by the source.

$$\begin{aligned} \omega_k(t) &= \frac{\partial}{\partial t}\Theta_{\mathrm{rcv},k}(t) \\ &= \frac{\partial}{\partial t}[\omega_\circ\,(t-\tau_k(t)) + \Theta_\circ + m_k\pi] \\ \omega_k(t) &= \omega_\circ\,(1-\frac{\partial\tau_k}{\partial t}(t)) \end{aligned} \tag{3.9}$$

Inserting the path integral[JKPS94] for travel time (Eq. 3.8) into the equation for the time-dependent received frequency $\omega_k(t)$ (Eq. 3.9), a modified acoustic dispersion relation is obtained:

$$\omega_k(t) = \omega_\circ\,(1 - \frac{\partial}{\partial t}\int_{s_1(t)}^{s_2(t)} \frac{ds}{\boldsymbol{v}(s,t)\cdot\hat{\boldsymbol{s}}(s) + c(s)}) \tag{3.10}$$

which, when the fundamental theorem of calculus and the chain rule for derivatives are employed, becomes

$$\begin{aligned} \omega_k(t) = \omega_\circ\,[1 - (&\frac{ds_2(t)}{dt}\frac{1}{\boldsymbol{v}(s_2(t),t)\cdot\hat{\boldsymbol{s}}(s_2(t)) + c(s_2(t))} - \\ &\frac{ds_1(t)}{dt}\frac{1}{\boldsymbol{v}(s_1(t),t)\cdot\hat{\boldsymbol{s}}(s_1(t)) + c(s_1(t))}) + O(c^{-2}(s))\,] \end{aligned} \tag{3.11}$$

If the wave-perturbed surface is treated as a secondary source (Huygen's principle), and the surface is approximated as perfectly flat and heaving vertically, then s_1 and s_2 become functions of the zero-mean surface vertical displacement $\eta(t)$ (Fig. 3.5, gray ray path trace).

$$s_j(t) \sim \bar{s}_j + \eta(t)\,\sin(\alpha);\; j = 1,2 \tag{3.12}$$

where $\bar{s}_j$ is the mean or unperturbed coordinate and α is the angle (from horizontal) of incidence of the ray path on the moving surface. The above relation (Eq. 3.12) assumes purely vertical motion of the purely horizontal surface, and low grazing angles. Realistic surface gravity waves have finite slope. Thus, this model omits any redirection of the acoustic waves by interaction with a rough surface.

For a ray that interacts with the surface multiple times, the integral in Eq. 3.8 can be split into multiple path segments, where each reflection off the surface is treated as a separate secondary source (Fig. 3.5), and the integral in Eq. 3.10 is computed over each segment between surface reflections.

It is well known, for example in the field of frequency modulated (FM) communications [Zie95], that the spectrum of a sinusoid at carrier frequency ω_c that is modulated in phase by a sinusoidal function with amplitude β and frequency ω_m can be written as a sum of Bessel functions[MF53].

$$\begin{aligned} p_k(t) &= A_k Re[e^{i\omega_c t + i\beta\sin(\omega_m t)}] && (3.13) \\ &= A_k Re[e^{i\omega_c t} \sum_{n=-\infty}^{\infty} J_n(\beta) e^{in\omega_m t}] && (3.14) \end{aligned}$$

If the modulating function has more than one frequency component, the resulting spectrum is the product of the sum of Bessel functions of the first kind for each frequency.

$$\begin{aligned} p_k(t) &= A_k Re[e^{i\omega_c t} \sum_{l=-\infty}^{\infty} J_l(\beta_1) e^{il\omega_{m1} t} \sum_{n=-\infty}^{\infty} J_n(\beta_2) e^{in\omega_{m2} t} ... && (3.15) \\ &= A_k Re[e^{i\omega_c t} \sum_{l=-\infty}^{\infty} \sum_{n=-\infty}^{\infty} J_n(\beta_1) J_l(\beta_2) ... e^{in\omega_{m1} t + il\omega_{m2} t + ...}] && (3.16) \end{aligned}$$

The form of the phase modulation in Eq. 3.13 might lead to the expectation that the distribution of frequency of the received signal $p_k(t)$ is confined to within the range $\omega_c \pm \beta\omega_m$. It is perhaps surprising, then, that the spectrum of the received signal $p_k(t)$ will have frequency components at integer multiples of ω_m – potentially much wider than $\beta\omega_m$ (re: Eq. 3.14). Moreover, the presence of multiple modulating frequencies can lead to non-linear (with respect to surface waves) effects, with every integer-multiple combination of modulating frequencies present in the modulating time series (i.e. the vertical surface motions).

If the reflective surface of an ocean acoustic waveguide heaves up and down at the surface reflection point of a single eigenray connecting source and receiver, thereby lengthening and shortening the acoustic travel times, then the travel time τ_k can be written as the sum of two integrals of similar form to Eq. 3.8, each one corresponding to one segment of the path: source to moving surface and moving surface to receiver. The appearance of $\eta(t)$ in both these integrals is the cause for the factor of 2 in the frequency shift associated with the canonical bistatic Doppler shift problem[Uri83]. In general, the displacement $\eta(t)$ at the ray's point of reflection can be written as a Fourier series

$$\eta(t) = \sum_{n=1}^{N} S_n \sin(\omega_n t + \gamma_n), \tag{3.17}$$

In Eq. 3.17, S_n is the amplitude and γ_n is the phase of the n^{th} frequency component. The amplitudes S_n are inferred from the measured surface height spectrum $P(\sigma_n)$:

$$S_n = (\Delta\sigma_n P(\sigma_n))^{1/2} \tag{3.18}$$

where $\Delta\sigma_n/2\pi$ is the width of the n^{th} surface wave frequency band. Equations 3.16 and 3.17 result in a received acoustic field consisting of the original acoustic frequency ω_c, plus information about the surface waves.

$$p_{\mathrm{rcv}}(t) = Re[\sum_{k}^{N_{\mathrm{rays}}} A_k e^{i\omega_c t} \prod_n \sum_{l=-\infty}^{\infty} J_l(\beta_{k,n}) e^{il\omega_n t}] \tag{3.19}$$

The terms $\beta_{k,n}$ individually are analogous to β in Eq. 3.14, and contain information about the grazing angles of the k^{th} eigenray, as well as the amplitude of the n^{th} surface wave component.

The sinusoidal nature of the modulation leads to positive and negative Doppler shift, and if the argument β is small, then the linear behavior of the first few Bessel functions (Fig. 3.6) will result in 'copies' of the surface wave spectrum whose levels relative to that of the unshifted center frequency will increase with an increase in surface wave height. If β is larger (~ 1.5), then the modulation will result in a more complicated relationship of the sideband levels. Through its relation to the travel time for eigenray k (in its influence on 'source' and 'receiver' positions s_1

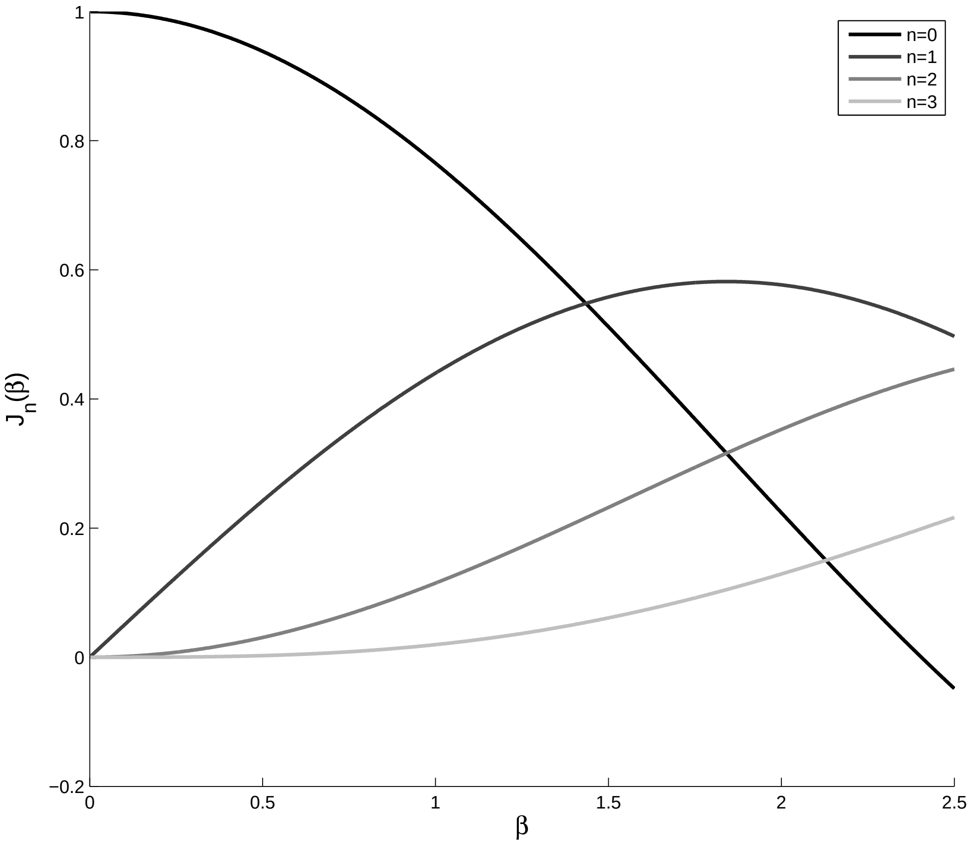

Figure 3.6: Bessel functions of the first kind $J_n(\beta)$ for $n = 0, 1, 2, 3$ and $0 < \beta < 2.5$. The range of β arises from the relevant values of sound speed, waveguide depth and receiver range, ocean wave height, and carrier frequency for the experiment in this paper.

and s_2 in Eq. 3.12), the argument of the Bessel function $\beta_{k,n}$ for the n^{th} component of the surface wave spectrum contains information about the angle of incidence α of the acoustic wave fronts on the surface, and the number of surface interactions m_k, the average speed of sound in the waveguide c, the carrier frequency ω_c (in $rad\, s^{-1}$), and amplitude S_n of the surface wave:

$$\beta_{n,k} = \frac{m_k}{c} S_n \omega_c \sin(\alpha_k) \tag{3.20}$$

It is worth noting that, for this model of frequency spreading, the modulated acoustic spectrum is independent of the direction of propagation of the surface waves relative to the acoustic source and receiver positions. Only the acoustic path's dependence on surface height affects the phase and frequency of the acoustic signal.

Spectral broadening by phase modulation can occur even in a setting where there is only one surface-interacting eigenray connecting the source and receiver. The magnitude of the distortions depends on several factors, including the steepness of the angle of incidence between the ray and the reflective surface, and the height of the surface waves. Therefore, in an environment with multiple eigenrays interacting with the surface, the resulting total received acoustic spectrum will depend on each arrival. Because the Doppler-shifted sidebands' levels depend not only on the ray amplitudes, but also on the acoustic-surface wave interaction of each eigenray, a relatively weak (i.e. small amplitude A_k) eigenray that reflects off the surface multiple times may cause a greater distortion in the received signal than a stronger eigenray that interacts with the surface only a few times. As will be seen in Sect. 3.5, the conditions during the experiment were, for the most part, such that the value of β fell into the region where the first several sidebands' levels will increase in level with steepness of intersection of the acoustic ray paths with the surface (Fig. 3.6). These insights become clearer through the use of numerical models.

3.3.3 Higher order perturbation

A considerable body of work treats the problem of acoustic interaction with a rough, moving surface through perturbational expansion[Chu78, HL75b, PW91, WJ95]. The basic premise of such approaches is that the deviations of a solution from the ideal case are small enough to allow grouping of terms by order and treatment of each ordered problem independent of the ideal case. When a perturbational problem is set up, terms in equations are grouped by power of some expansion parameter that is assumed to be small (i.e. $\ll 1$), so that no term can affect the problem involving terms of lower order than it. The order 0 (unperturbed) problem is independent for all problems of order ≥ 1. In the problem of scattering in ocean acoustics, the parameter most often chosen naturally involves the surface wave field, such as the RMS surface wave height, and is scaled by some characteristic length of the acoustic field, such as the acoustic wavenumber. For example, for the acoustic pressure ψ,

$$\psi(\boldsymbol{x}, t) = \sum_{n=0}^{\infty} \frac{(kh)^n}{n!} \psi_n(\boldsymbol{x}, t) \tag{3.21}$$

where k is the acoustic wavenumber and h is the RMS wave height. Closely related to this is the Rayleigh parameter, $kh \sin\alpha$, which takes into account the angle of incidence α of the incident acoustic field with the mean surface plane.

As has been implied in the Introduction (Sect. 3.2), it is easy to show using first order perturbation theory with time dependence that interaction of a narrowband acoustic signal with a rough, moving ocean surface will result in a received signal that contains the surface wave spectrum as sidebands to the transmitted tones[HL75a]. The above terms ψ_n are solutions to the wave equation, with their own forcing and boundary conditions. The upper boundary condition for ψ_1, for example, introduces a frequency-dependence of the received acoustic field on the surface waves:

$$\widetilde{\psi}_1(\boldsymbol{r}, z = 0, \omega) = -\widetilde{\eta}(\boldsymbol{r}, \omega) \otimes \frac{\partial}{\partial z} \widetilde{\psi}_0(\boldsymbol{r}, z, \omega)|_{z=0} \tag{3.22}$$

Here the convolution in frequency arises from a Fourier transform of the perturbed wave equation, the tilde denotes the Fourier transform in time, and the position vector $\boldsymbol{x} = [\boldsymbol{r}, z]$.

In the context of the observations of multiple, harmonic-like sidebands in Figs. 3.2, 3.3 and 3.4, however, it makes sense to seek an extension to this expression that results in a received spectrum whose broadening exceeds that predicted by the first order theory, and can lead to harmonic-like sidebands. To this end, higher order perturbation theory is explored here. The treatment follows that of Pourkaviani and Willemsen[PW91] for a pressure field that is comprised of incident and scattered plane waves with wavenumber vector $[\boldsymbol{k}_r, k_z; \omega]$, where $|\boldsymbol{k}_r|^2 + k_z^2 = \omega^2/c^2$ and amplitude described by $f_{(i,s)}(\boldsymbol{k}_{(r,s_r)}, \omega)$.

$$p_{(i,s)}(\boldsymbol{r}, t) = \iint d\boldsymbol{k}_r \int d\omega\, e^{i\boldsymbol{k}_r\cdot\boldsymbol{r}} e^{-i\omega t} e^{\mp i k_z z} f_{(i,s)}(\boldsymbol{k}_r, \omega) \tag{3.23}$$

The "T-matrix" is defined as the mapping of incident radiation $f_i(\boldsymbol{k}_r, \omega)$ into the scattered field $f_s(\boldsymbol{k}_{s_r}, \omega_s)$:

$$f_s(\boldsymbol{k}_{s_r}, \omega_s) = \iint d\boldsymbol{k}_r \int d\omega\, T(\boldsymbol{k}_{s_r}, \omega_s; \boldsymbol{k}_r, \omega) f_i(\boldsymbol{k}_r, \omega) \tag{3.24}$$

where ω_s and $\boldsymbol{k}_{s_r}$ are the frequency and horizontal component of the scattered acoustic wavenumber vector, respectively. For an incident field consisting of delta functions in frequency and spatial wavenumber, the scattered field is then the T-matrix.

By expanding the T-matrix asymptotically into a series of components T_n as in Eq. 3.21, and expanding the plane wave expression (Eq. 3.23) in a Taylor series about $z = 0$, and grouping terms by order of kh, a series of equations relating T_m to all T_n for all $0 \leq n \leq m$ is found.

$$\begin{aligned} T_m(\boldsymbol{k}_{s_r}, \omega_s; \boldsymbol{k}_{i_r}, \omega_i) = \iint d\boldsymbol{r} \int dt\, e^{i\boldsymbol{r}\cdot(\boldsymbol{k}_{s_r} - \boldsymbol{k}_{i_r})} e^{-it(\omega_s - \omega_i)} [-ik_z \eta(\boldsymbol{r}, t)]^m \\ \times \sum_{n=0}^{m-1} \binom{m}{n} [ik_z \eta(\boldsymbol{r}, t)]^{m-n} T_n(\boldsymbol{k}_r, \omega; \boldsymbol{k}_{i_r}, \omega_i) \end{aligned} \tag{3.25}$$

where η is the surface wave field, and $\omega_{(i,s)}$ and $\boldsymbol{k}_{(i,s)_r}$ are, respectively, the temporal frequency and horizontal part of the wavenumber vector of the scattered (subscript s) and incident (subscript i) acoustic wave contributions. The spatial and temporal Fourier Transform in the expression for the m^{th} term of the T-matrix results in the convolution of the incident acoustic field with the Fourier Transform of the

m^{th} power of the surface wave field, $\eta^m(\boldsymbol{r}, t)$. This gives rise to a contribution to the received pressure field that is m-times the width of the surface wave field. In temporal frequency, these terms predict the Doppler shift induced by scattering from a moving, rough surface, while in spatial frequency (or wavenumber), they lead to the Bragg condition for integer multiples of surface wavenumber finds its way into the higher order perturbation terms[HL75a, PW91].

Thus, higher order ($(kh)^n$, $n \geq 2$) perturbation can lead to evenly spaced peaks in the received acoustic spectrum, so long as the width of the surface wave spectrum is smaller than the dominant surface wave frequency. In this regard it is similar to frequency distortion by phase modulation (Eq. 3.19), as the sum-and-difference frequencies resulting from the product of sums will tend to broaden the higher order sidebands in that mechanism, as well.

Both these expressions (Eqs. 3.19 and 3.25) are based on certain assumptions.

Neither expression addresses the issue of caustics or surface wave focalization of sound, as discussed by Preisig and Deane[PD04]. The solution of a wave equation with perturbational expansions requires that the expansion term kh be small enough that the equation's left- and right-hand sides can be grouped by order, and each order can be solved independently. However, if the expansion parameter is too large, then there is coupling between orders and this solution is no longer valid. In scattering in ocean acoustics, the expansion parameter can become too large when the surface wave amplitudes become too large with respect to the surface wavelength (i.e., the surface wave slopes become too steep). In contrast, the phase modulation model is constructed so that any eigenray connecting (without disruption) the source and receiver that sees surface motion will impart information about that motion into the acoustic spectrum.

3.3.4 Numerical modeling

To test Eq. 3.19 as a model of spectral broadening for shallow ocean acoustic waveguides, a model is developed that integrates the pressure field computed from rays with a random realization of surface waves. For each computed eigenray (Eq. 3.4), the effective travel time fluctuations that result from the lengthening and

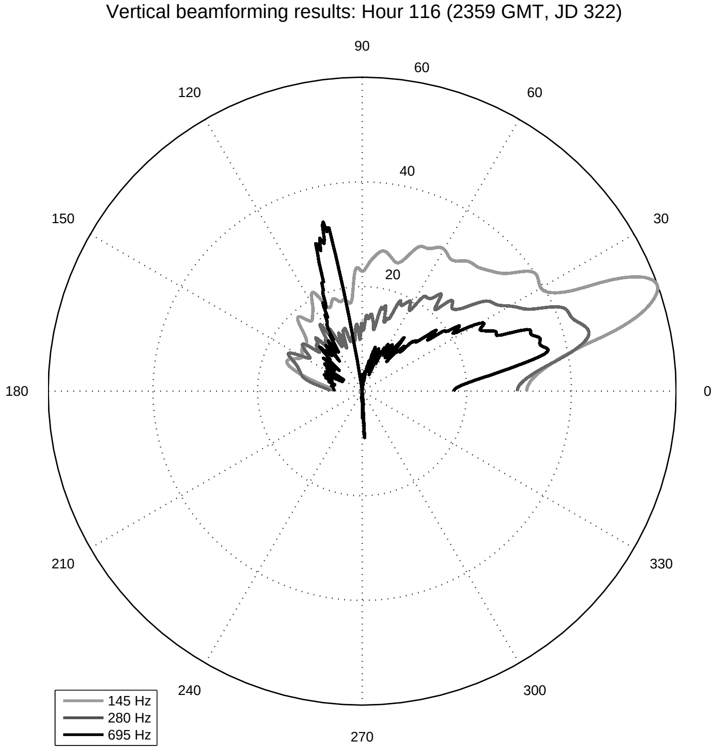

Figure 3.7: Beamforming results sweeping through vertical with azimuth fixed in the direction of the source (20°) using the endfire array. The strong arrival at 100° at 695 Hz (black trace) is a grating lobe.

shortening of the acoustic path by the motions of the surface are computed from the measured surface wave spectrum, scaled by the sine of angle(s) of incidence for each surface interaction. An acoustic signal is constructed consisting of the carrier frequencies transmitted during an experiment, with the phase evolution governed by the time-dependent travel time. The surface is modeled here as perfectly flat, meaning rays are only specularly reflected. The contributions to the total pressure field at the receiver from each eigenray are added coherently, scaled according to the eigenray amplitudes A_k (Eq. 3.4) inferred from vertical beamformer output (Fig. 3.7). In order to maintain independence of the modulating functions for each eigenray and maintain surface waves as a random process, each individual surface wave frequency component's phase is randomized for each reflection on each path. Single realizations of the surface waves in which the randomized phase offsets are similar will give rise to unlikely phase distortions, which in turn will cause unlikely sideband amplitudes. To mitigate against this likelihood, the received field in this model is computed repeatedly, and an ensemble average of the spectrum is computed. While their relative level may be lower due to the attenuation associated with multiple interactions with the waveguide bottom, the resulting Doppler shifted received contribution associated with the steeper eigenrays may be just as significant in their effects on the received spectrum sidebands as those associated with the more direct paths. The analytical representation of the spectrum resulting from this harmonic modulation lends itself to easy computation (or even look-up) of results for relevant values of the magnitude β of the modulating function.

It is beneficial to plot Bessel functions $J_n(\beta)$ over the relevant range of values of β to predict the magnitudes of the sidebands introduced by the surface waves (Eqs. 3.14 and 3.20) because of the non-linear effect that the surface wave amplitude term in the phase modulation (Eq. 3.20) has on the acoustic spectrum (Fig. 3.6). The sound speed c during the experiment is estimated at $1510\,\mathrm{m\,s^{-1}}$, and the tone frequencies range between 70 and 700 Hz. Significant wave height η_s varies from 0.5 to 1.6 m during the experiment. With a critical angle of around 30° [McA02] and a propagation distance of 1.25 km, the maximum number of reflections off the surface that an eigenray could undergo without having a significant part of its energy transmitted into the bottom for the experiment geometry described in the next section is 100. However, losses from interactions with the bottom and geometrical spreading further limit the range of vertical arrival angles that warrants inspection. Vertical beamformer output shows that dominant acoustic arrival angles range between 10° and 20° above horizontal, depending on the acoustic frequency and the waveguide depth. The waveguide depth fluctuates with the tides. These steep dominant eigenrays connecting source and receiver intersect the ocean surface at steeper angles, and interact more times with the ocean surface. In terms of mode theory, the depths of the source and receivers determine the modal excitation and reception. If the source or receiver depth is near one mode's node and another's anti-node, then the first mode will be strongly represented while the other will have little presence in the received signal. Tidal fluctuations influence the arrival structure at the array by stretching and compressing the vertical mode functions. The static source and receivers are effectively moved along these mode functions, and their moving positions relative to nodes and anti-nodes of the modal functions emphasizes and de-emphasizes different modes (and therefore eigenrays) over the course of the experiment.

The model just described is compared to results from a model based on Eq. 3.25 for scattering terms up to $O[(kh)^4]$ for a monochromatic, unidirectional surface wave spectrum with the direction of propagation lying directly along the direction of the vertical plane of acoustic propagation. Predictions of received spectra produced by higher order perturbation and phase modulation by surface waves are compared for two sets of surface wave conditions mimicking the variety of waves observed during the shallow water experiment.

The two surface wave frequencies chosen are 0.07 and 0.16 Hz, corresponding to surface wavelengths of 135 and 50 m, respectively. The amplitudes for these narrowband surface wave trains are likewise chosen to reflect observed surface wave RMS heights, 0.15 m for the lower frequency waves and 0.4 m for the higher frequency waves. Perturbation computations are carried out to 4^{th} order, and modulations are simulated for a single reflection and also for a series of reflections where the surface wave phase is randomized for each one. The results show that

Eqs. 3.19 and 3.25 can predict quite different sideband levels, as discussed in Sect. 3.6.

3.4 Very shallow water experiment

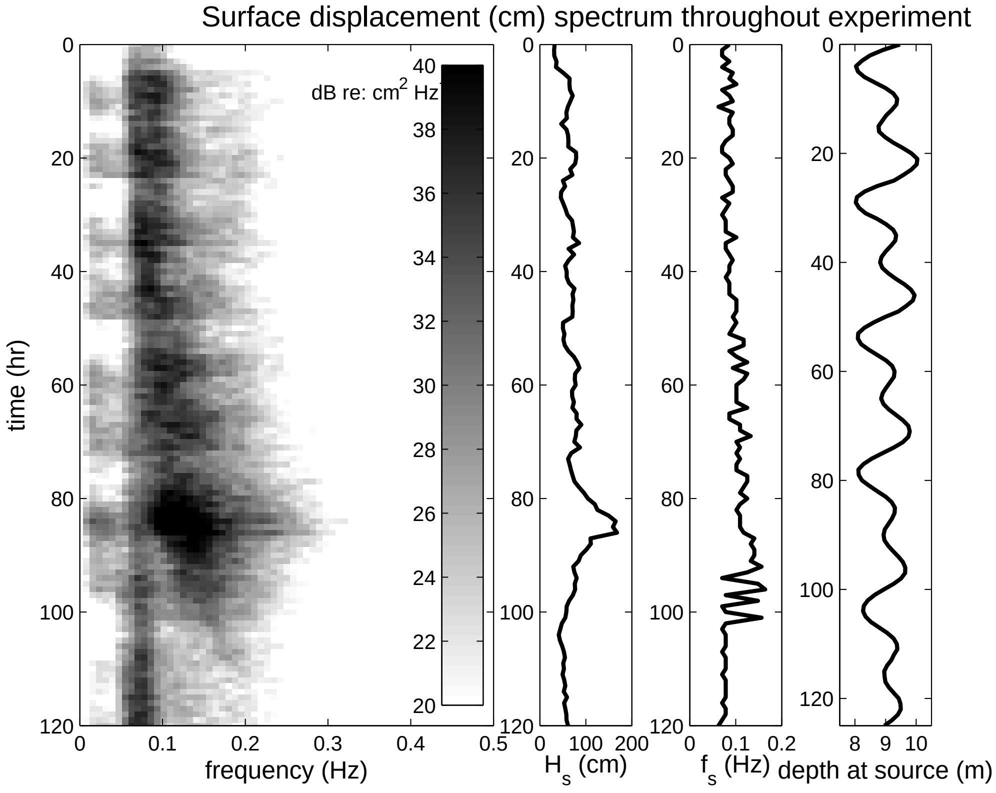

Figure 3.8: A spectrogram computed from the ocean surface displacement time series measured by the pressure sensor deployed on site (leftmost panel). Significant wave height vs. time (second plot from left), significant frequency vs. time (second plot from right), and water depth at the acoustic source location vs. time (rightmost plot). The three time segments of focus in this paper occur at approximately hours 92, 100 and 119.

The data presented in this paper were collected during an experiment conducted in the autumn time period immediately off the coast of Camp Pendleton Marine Base in southern California. Located between San Diego County and San Clemente, Camp Pendleton protects tens of miles of uniquely pristine coastline from development, and provides an excellent site for study. Over the course of the experiment, ocean surface wave spectra varied significantly (Figs. 3.1 and 3.8), due in large part to the distance from the wave-generating systems to the experiment site and the dispersive nature of ocean surface waves (Eq. 3.2), with longer period (lower frequency) waves traveling faster. At times during the five days the CW transmissions were conducted, long period swell from distant systems ("ground swell") constituted the only surface wave activity, while larger, more broadband surface waves with higher peak frequency ("wind swell") originating from systems closer to the experiment site contributed at other times. In addition, a period of overlap when these two types of surface waves (Fig. 3.1) were present simultaneously (See Fig. 3.8, hours 85-105, and Fig. 3.1, medium-gray trace).

3.4.1 Acoustic receivers and source

Two acoustic arrays, each consisting of 64 equally spaced hydrophones, were deployed horizontally on the ocean bottom during the experiment. The spacing of the elements in the arrays was 1.875 m, and each channel was digitized at 1500 samples/sec. The sampled data were cabled back to shore by fiber-optic cable, where they were recorded continuously on hard disk and tape. The two arrays were deployed in approximately 12 m of water 1.5 km offshore, with one parallel to the beach (the "broadside" array) and the other mostly perpendicular to the beach (the "endfire" array) (Fig. 3.9).

Over the first few days of the experiment, variable wave and current conditions resulted in both hydrophone arrays being buried by a thin (less than a few cm) layer of sand. This layer of sediment proved insufficient to affect the received acoustic levels significantly, and was beneficial in securing the array into place. Because of this partial burial, it is believed that the motions of the hydrophones were zero. Thus, any frequency shift observed in the acoustic spectra can be confidently attributed to motions of the other than those of the receiving array.

The orientations of the two arrays (Fig. 3.9) offer the opportunity to obtain direction-of-arrival information for the acoustic field in both the horizontal plane (azimuthal angle) and the vertical plane. Beamforming in the vertical plane provides information about the dominant acoustic modes involved in the propagation (Figs. 3.5, 3.7), while the horizontal directionality offer insights into the surface waves' impact on the out-of-plane scattering (Figs. 3.4, 3.10).

The acoustic source used in this experiment was a J-15 source[Det], deployed in approximately 9 m deep water, 500 m closer to shore and about 1 km up the coast from the arrays. Over the course of the experiment, transmissions of 5-minute duration consisting of 8 narrowband tones were made every half hour (hours 92 and 119) or every hour (hour 100) during the daylight hours. The frequencies of the tones transmitted were 70, 95, 145, 195, 280, 370, 535 and 695 Hz, though the noise field was such that lower of these tones were often indistinguishable. Unlike the hydrophone arrays, the source was moored above the bottom and so was not buried by shifting sediments. Moreover, the source mooring apparatus was designed to hold the transducer firmly in place. Its mass and footing were easily sufficient to keep the source from moving under forces of the surface waves, and any frequency shifts in the acoustic spectrum therefore are not due to source motions.

3.4.2 Environmental instrumentation

For measuring the ocean surface waves, a PUV (Pressure and 2 horizontal water velocity components) sensor was deployed near the source over the course of the experiment. Additionally, a 4-pressure-sensor system capable of directional surface wave spectrum measurements was deployed and maintained at the San Clemente Pier (approximately 40 km up the coast) by the Coastal Data Information Program (CDIP) at Scripps Institution of Oceanography. These data are freely available on the CDIP web site, http://cdip.ucsd.edu/. The PUV sensor sampled continuously for 20 minutes every hour, with a sampling frequency of 2 Hz. The CDIP platform was sampled at 1 Hz continuously, over the total duration of the experiment. Given that the system was approximately 40 km up the coast from the experiment site, the CDIP data are primarily used for an estimation of the arrival direction of the dominant period. The pressure data of the PUV time series are used for computation of the mean water column height, the tides, and the surface displacement spectra (Fig. 3.8), while the directionality of the surface waves is obtained from the CDIP data archives. The horizontal flow velocity components of the PUV data set are not used. For this study, definitions and methods pertaining to surface wave data analysis are adapted from CDIP. Significant wave height, for example, is 4 times the root-mean-square wave height: it is the minimum full wave height (2 times amplitude) of the largest 32% of observed waves. Significant (or dominant) wave frequency – or equivalently, period – is the frequency at which the maximum in the surface wave spectrum occurs. This definition allows for the identification of multiple wave-generating systems in one set of measurements. Significant wave direction is the direction in which the waves at the peak in the spectrum propagate. CDIP's online analysis does not provide identification of multiple significant wave frequencies or directions.

Conductivity, temperature and depth (CTD) profiles were taken during the experiment, and are used for characterizing the water column sound speed profile. Geoacoustic properties at the experiment site were derived by McArthur[McA02]. The waveguide consists of a roughly iso-speed water duct ($c = 1510$ m s^{-1}), with a thin ($\sim$1 m) sediment bottom ($c_s = 1575$ m s^{-1}, $\alpha_s = 0.9$ dB λ^{-1}) overlying a hard basement ($c_b = 1680$ m s^{-1}, $\alpha_b = 0.3$ dB λ^{-1}) [McA02].

3.5 Measurement results

In the experimental data set, the arrangement of the hydrophones (Fig. 3.9) allows for high resolution beamforming in both the vertical (using the end-fire array's aperture) and horizontal (using the broadside array's aperture) angles especially given the large, two-dimensional spatial aperture. In addition, the large number of hydrophone elements provides a large number of degrees of freedom in computing incoherently averaged spectra. Relating these ocean acoustic spectra to surface wave activity is made possible by the presence of both the onsite pressure sensor, and data from CDIP. Precise, fixed positioning of the instrumentation and prior, in-depth study of the local propagation characteristics[McA02] are also crucial to be able to perform this study. In this section results from the analyses of these data are presented.

3.5.1 Omnidirectional spectra

Omnidirectional acoustic spectra are estimated from 50%-overlapping temporal snapshots spanning one complete 5-minute transmission, and then incoherently averaged over most of the elements of one of the two acoustic arrays (approximately 60 elements). One remarkable feature of the acoustic data can be seen when the spectrum is computed using long (2^{17} points, $\delta f \sim .01$ Hz) Fast Fourier Transforms (FFT's). Comparison of the omni-directional acoustic pressure spectra for 3 time periods during the experiment with dramatically different surface wave conditions (Fig. 3.1) indicates a complicated dependence of the spectral distortion on significant wave height and spectral content of the surface waves (Figs. 3.2, 3.3 and 3.11).

The first noticeable features of incoherently averaged, long FFT's of the acoustic recordings (Figs. 3.2 and 3.3) are sidebands that occur at frequencies $f_\circ \pm f_s$, the sum-and-difference frequencies of the acoustic carrier frequency $f_\circ$ and the dominant surface wave frequency f_s. The levels of these first sidebands show clear dependence on acoustic carrier frequency, with higher frequencies exhibiting higher sideband levels. This dependence, which is visible throughout the experiment and is true at all frequencies, is consistent with first-order perturbation through the expansion parameter kh (Eq. 3.21, $k = \omega/c$) and the simplified phase modulation model through the argument β (Eq. 3.20). To a lesser extent, the levels of these first sidebands also show dependence on surface wave height, which is most pronounced comparing the received spectra at 145 Hz and 280 Hz (light and medium gray traces, respectively) in the Figs. 3.2 ($H_s = 1.01$ m), 3.3 ($H_s = .58$ m) and 3.11 ($H_s = .72$ m). The sidebands' location in frequency and level dependences on acoustic frequency and surface wave height are consistent with first-order perturbational scattering (Eq. 3.25) and the simplified phase modulation model (Eq. 3.20 and Fig. 3.6).

Even more curious than the behavior of the first sideband in acoustic frequency redistribution is the regular, harmonic-like spacing of multiple spectral sidebands at frequency intervals equal to the dominant surface wave frequency. Arrows noting integer multiples of the dominant surface wave frequency f_s centered about the acoustic carrier frequency align quite well with sidebands in the spectra (Figs. 3.2, 3.3, and 3.11). This spectral structure suggests phase modulation, such as that in Eq. 3.14, or higher order perturbation, as in Eq. 3.25, of the initial narrowband signal, especially where multiple interactions of the acoustic signal with the moving surface have occurred. Both higher order scattering and the simplified phase modulation model are non-linear with respect to the surface deviations (see Section 3.3).

The higher order sidebands do not behave as predictably in the variety of ocean surface wave conditions as the first sidebands do. Though the surface waves were smaller in amplitude during the period near the end of the experiment (Fig. 3.8), the sidebands are easily discerned at multiples of the surface wave peak frequency, in part due to lack of noise contamination (Fig. 3.3). It is striking that the higher order sidebands are at least as high in level when the surface waves – and therefore the expansion parameter kh – are small amplitude and low frequency as when the waves are larger amplitude and more broadband with higher peak frequency. At hour 119 (Fig. 3.3), kh is approximately 0.4 at an acoustic frequency of 695 Hz. If higher order scattering with only a single surface interaction leads to the 2nd, 3rd and higher ordered sidebands, it would be expected that the sidebands would fall off faster in the smaller surface wave conditions than in conditions where kh is larger, such as in Fig. 3.2. While similar decrease in level can be expected for sidebands arising from scattering involving a single surface incidence (Eq. 3.19), if coherence exists between reflections along a ray path, then the phase modulation by surface waves could be additive. Such a cumulative phase deviation would lead to raised levels of the higher order sidebands.

Further examination of the results in Figure 3.11 reveals additional interesting aspects of the received acoustic field's dependence on the ocean surface waves. Spectra of received narrowband acoustic tones can become quite complicated when more than one frequency of surface wave is significant (Eq. 3.16). Sidebands occur at integer multiples of each of the dominant surface wave frequencies, as well as at other frequencies that may be integer combinations of these frequencies. Higher-order scattering also can lead to such a complicated received acoustic spectrum as shown in Fig. 3.11 through the convolution of the transmitted acoustic spectrum with the Fourier Transform of the n^{th} power of the surface deviations (Eq. 3.25). Equation 3.19 predicts the occurrence of sidebands at every integer multiple combination of frequencies in the surface wave field when the surface wave field is written as a Fourier sum, for example if amplitudes S_n and phases γ_n in Eq. 3.17 are specified in terms of the measured surface wave spectrum.

One final outstanding feature of Fig. 3.11 is the first sidebands' levels relative to the center peak at the transmitted frequency. At this time during the experiment (approximately hour 100, Fig. 3.8), the first acoustic sidebands at 695 Hz reach levels approaching that of the un-shifted, center frequency bin. It is worth noting that, over the range of argument β of the Bessel functions that pertains to the conditions of this experiment (Fig. 3.6), a value of β exists at which the 0^{th} and 1^{st} Bessel functions $J_0(\beta)$ and $J_1(\beta)$ are equal. Under these conditions, which can be created by the right combination of acoustic carrier frequency, surface wave amplitude and frequency, and number of phase-coherent interactions (Eq. 3.20), the first sidebands will be the same amplitude as the center peak. If, in Fig. 3.11, these conditions have been approached, the negatively shifted sideband's level within 2 dB of the center peak would suggest β is approximately 1.5. Alternatively, this high-level sideband could be in part due to the presence of surface waves with more than one dominant frequency, as could happen with two independent ocean surface wave systems present. In this case, sidebands would occur at integer multiples of each of the dominant surface wave frequencies, as well as at other frequencies that may be integer combinations of these frequencies (Eq. 3.19). Thus, the high sideband during the time when multiple surface wave systems were present could be the coincidence of multiple sidebands whose locations in the spectrum are too close to discern given the limits of temporal frequency resolution, as shown by the roses, diamonds and arrows in Fig. 3.11.

3.5.2 Beamformer output

While omnidirectional data processing is a powerful method for investigating the influence of surface gravity waves on received acoustic tones, it has the obvious shortfall that it discards any directional information. Narrowband beamforming, including over a range of frequencies centered on those of the transmitted tones, of the acoustic array data reveal additional important physics of spectral distortion of narrowband acoustic tones by surface gravity waves. The beamforming algorithm used is the white-noise-constrained algorithm, which is a data-adaptive technique[CZO87]. In order to guarantee stability in the adaptive beamformer algorithm, at least as many snapshots as there are hydrophones must be used to compute the covariance matrices – these matrices must be full rank. The constraint was set to a value of 3 dB below ten times the logarithm (base ten) of the number of array elements. To achieve the spatial aperture required to resolve the directional differences of various arrivals of sometimes less than 1 degree, nearly the entire hydrophone array was employed for computing the directional spectrum. Thus, in order to maintain sufficient temporal resolution of the beamformer (FFT length = 2^{15} points) to discern surface wave frequencies, consecutive 5-minute data recording periods were spliced together when conditions remained stationary.

A search through vertical angle of arrival using the endfire array indicates that lower mode numbers (small grazing angle rays), while present, do not represent a majority of the incident acoustic energy (Fig. 3.7). Rather, near-horizontal energy conspicuously absent in the measured data the received spectrum is dominated by steeper angled arrivals that interact more often with a heaving reflective surface. A steeper grazing angle at the ocean surface will result in a greater Doppler shift of the propagating signal by the surface waves. In terms of the simplified phase modulation model, an increase in surface interaction angle will increase β (Eq. 3.20), which will increase sideband levels in general if β is small ($\beta < 2$, see Fig. 3.6). In terms of perturbational scattering, a steeper interaction with the surface increases k_z in Eq. 3.25, and in general all sideband levels will increase. Figures 3.4 and 3.10 show the results for the horizontal beamfomer output at 280 Hz for two different times in the experiment, hours 92 (Fig. 3.4 and 119 (Fig. 3.10). Plane wave beamformer output from the broadside array as a function of azimuthal angle (vertical angle is fixed at 15° above the horizontal) at each of the 8 transmitted frequencies shows a strong arrival originating from the known direction of the moored source (approximately 20° E from true North, Fig. 3.9).

Horizontal angle beamformer output as a function of both azimuthal angle and acoustic frequency also shows sidebands that are offset asymmetrically in direction of arrival relative to the observed signal peak corresponding to the acoustic source, but they are symmetrical about the center frequency, thus indicating Doppler shifting by Bragg scattering of the surface waves. In the beamformer output for the data recorded at hour 92, when a large ocean wind-wave event was occurring, the Bragg-scattered sidebands are easily deciphered for most of the 8 transmitted frequencies (poor signal-to-noise ratio at 70 Hz rendered identification of sidebands impossible), and computed directions of ocean wave propagation (69.5° true North propagation, or 249.5° origination) according to Eq. 3.3 are consistent with the direction of the peak frequency waves as measured by the CDIP sensor system (Fig. 3.4). The Doppler-shifted side lobes in Fig. 3.4 are clear evidence of first order scattering (Eq. 3.25) and the Bragg condition (Eq. 3.1).

The weaker, longer period surface waves at hour 119 did not lead to such easily identifiable features in the directional spectrum (Fig. 3.10). The lack of scattered sidebands in the beamformer output later in the experiment could be the result of the longer period (lower frequency) of the ocean waves, which would require longer FFT's to resolve small frequency deviations, and therefore longer time series to achieve good statistics. Horizontal beamforming was performed such that frequency of the longer period swell lies at the limit of the temporal frequency resolution of the directional spectra in Figs. 3.4 and 3.10. Ocean wave and tidal conditions proved too variable to allow more consecutive acoustic recordings to be combined to allow for longer FFT's that would yield the desirable level of temporal frequency resolution.

A calculation of the scattering parameter kh using values reflecting the conditions measured at hour 119 during the experiment offers another explanation for the lack of two identifiable sidebands in Fig. 3.10, that less scattering may have occurred at 280 Hz than observed earlier in the experiment. That is, the surface wave spectrum computed during this time shows a peak frequency of 0.07 Hz, with a significant wave height of 0.58 m, and the concurrent spectrum measured by CDIP placed the origin of this swell at 231°. With an RMS wave height of about 15 cm, kh was 0.18 at acoustic frequency 280 Hz and 0.4 at acoustic frequency 695 Hz. Scattering at this time was much weaker than earlier in the experiment when the data in Fig. 3.4 were recorded, when kh was 0.3 and 0.7 at 280 and 695 Hz, respectively.

Considerable evidence exists that Bragg scattering contributes to the data in Fig. 3.4, and first order scattering approximations do well to explain these observations. However, other results (Fig. 3.3) are not fully explained by first order scattering, nor higher order scattering where only a single incidence of the acoustic signal on the rough surface is involved. While it is clear from all these results that a scattering mechanism that is non-linear with respect to the surface waves contributes to the received acoustic spectra, understanding the behavior of this mechanism in a variety of surface wave conditions is in general very difficult, and would require at the very least very long acoustic recordings in sustained conditions supporting the assumption of ergodicity. Additional insights come from comparing these measured results to those of numerical models based on the previously mathematical constructs, as presented in the next section.

3.6 Modeling results

Numerical models are employed in an effort to better understand the physics giving rise to multiple sidebands in the received acoustic spectra that are clearly related to the ocean surface waves, particularly for any mechanisms in which the relationship between the ocean surface wave field and the underwater acoustic field is non-linear in nature. Figures 3.12, 3.13 and 3.14 show predictions from a computational model prescribed by Eq. 3.19, using surface wave spectra recorded by the PUV sensor (Fig. 3.1) to determine the values of $\beta_{n,k}$. The predictions of this model prescribed exhibit several features consistent with the experiment data shown in Figs. 3.2, 3.3 and 3.11. First, the modeled results show the presence of sidebands offset from acoustic center frequencies $f_\circ$ centered at the significant wave frequency $\pm f_s$, as measured by the on-site PUV sensor. Second, especially with larger ocean waves, multiple side-bands spaced integer multiples of f_s from the center frequency (Figs. 3.12 and 3.14) are predicted by the model, as seen in the data. All sideband amplitudes exhibit a dependence on acoustic frequency, with higher carrier frequency giving rise to higher sideband amplitudes. Third, the peaks observed in both the data and the model are symmetric in level about the center frequency. The model of phase modulation in Sect.3.3.2 results in symmetric sidebands, regardless of the propagation environment, whereas Bragg scattering can result in asymmetry in frequency spreading, due to blockage of one of the scattering surface patches by land, for example [LS04]. Results from the simplified modulation model presented in Sect. 3.3.2 (Figs. 3.12, 3.13 and 3.14), when employed as a sum of pressure ray contributions as in Eq. 3.19 and using ray paths computed using CASS/GRAB[WK96] combined with amplitudes inferred from measured vertical angle of arrival structure (Fig. 3.7), reproduce several features seen in the data recorded throughout the experiment (Figs. 3.2, 3.3 and 3.11).

Although many features of the data are reproduced by the model, there are some differences, as well. Direct comparison of the results of the phase modulated model summed over the computed ray paths to the measured acoustic spectra shows that the modeled Doppler shifted sidebands' amplitudes are too small. Examination of sideband patterns of the model for individual ray paths lends insight to this discrepancy. Figures 3.15 and 3.16 show the contribution to the total field for the four most dominant arrivals for hours 92 and 119, respectively. These results suggest that the sideband amplitude discrepancy between model and measurement can largely be attributed to lack of coherence in the sidebands. That is, because of the randomization in the phase modulation model, the sidebands are not reinforced in the summation over ray paths the way the non-randomized, center peak in frequency is.

When the modeled modulated spectrum associated with each individual arrival is examined, it is easily seen that the steeper-angled (with respect to horizontal) eigenrays result in higher level sidebands, especially for the higher orders of side-band (Figs. 3.15 and 3.16). More direct incidence on the heaving surface by the acoustic wave results in a larger value of β, the argument of the Bessel functions describing the spectrum of the phase-modulated signal (Eq. 3.16), in Eqs. 3.14 and 3.16. In Fig. 3.15, the direct and single-surface bounce paths contribute little to the observed side-bands due to their low (or non-existent) surface grazing angle and low number of reflections. In contrast, the paths that bounce 7 times or more start to yield the multiple harmonic-like sidebands containing surface wave information, with peaks spaced at integer-multiples of the significant ocean surface wave frequency. Also at the steeper angles and at higher acoustic carrier frequencies the 3^{rd} and 4^{th} sidebands begin to blur, becoming noticeably more broadband than the surface wave spectrum due to the sum-and-difference frequency terms (Eq. 3.16). In Fig. 3.16, it is clear that smaller surface waves result in lower level sidebands, which can also be expected from Bragg scattering and first order perturbation.

A higher order surface scattering model (Eq. 3.25) produces omnidirectional acoustic spectra identical to those of the phase modulation model when each is implemented with the same, narrowband surface waves with frequencies and amplitudes comparable to those observed during the experiment. Phase modulation, as described in 3.3.2, does not involve any redirection of the sound wave, and distorts the frequency spectrum of the received signal through time dependence of the acoustic propagation path. Scattering by a rough, moving surface can also lead to redistribution of narrrow-band acoustic tones (Eq. 3.25), including harmonic-like sidebands in measured spectra, and its performance against the above modulation model warrants testing. The conditions for which these models are run are outlined at the end of Sect. 3.3.4. Acoustic waves are incident on the mean surface at an angle of 15° for all these test cases. Higher order scattering (to 4^{th} order) predicts exactly the same results as the modulation model for a single reflection for 2 sets of simplified conditions mimicking those measured during the experiment (Fig. 3.17). While the treatment uses plane wave propagation, much like the treatment given by Pourkaviani and Willemsen[PW91], similar spectral predictions arise from the approach by Harper and Labianca[HL75a], where the source/receiver configuration are included explicitly.

Modeling the received field and allowing the acoustic field to interact multiple times with the rough moving surface in the modualation model causes the falloff of the sidebands to deviate quickly from the behavior the higher order perturbed field with only a single interaction (Fig. 3.17). The distance between the source and receiver during the shallow water experiment was approximately 30 times the horizontal length of one complete bottom-surface-bottom ray path segment for an eigenray whose angle of incidence with the mean surface is $\sim 15°$ (Fig. 3.5). With the phase of the surface waves randomized at each interaction, the argument β of the Bessel functions is realistic, and the sideband levels begin to overtake those predicted by higher order perturbation in terms of relative sideband amplitude. If the phase deviations remain coherent from reflection to reflection for one particular ray path in the phase modulation model, then the value of β for that ray path would increase considerably, and the total received signal would contain higher order sidebands accordingly. The similarity of predictions of the higher order perturbation and simplified phase modulation model, along with the observation that, when the acoustic field interacts with the moving surface multiple times in the phase modulation model the sidebands' levels increase accordingly, suggest that the simplified phase modulation model developed in Sect. 3.3.2 can be useful for predicting features of received narrowband acoustic tones in an environment where the acoustic field will interact multiple times with the rough, moving surface. It is important to remember in each of these models that the total received signal will be the sum of several arrivals, depending on the acoustic waveguide.

3.7 Discussion

Both the phase modulation model presented in Sect. 3.3.2 and the scattering models formulated by previous authors (and summarized in Sect. 3.3.3 represent intuitive ways to explain the observed character of spectral broadening that exceeds the measured surface wave spectrum. The phase modulation model presented here bears similarity in its approach to Rosenberg's[Ros99] method using a modified parabolic equation solver, in that they both step through series of frozen surface approximations in order to simulate surface deviation time dependence, though the work here is based on a ray-based propagation model. Accordingly, both these approaches similarly reproduce harmonic-like, Doppler-shifted sidebands as observed in received spectra of narrowband acoustic tones propagating through shallow waveguides with surface waves. It is believed here that these two models illustrate the physics of phase modulation through path length time dependence.

It is not surprising that higher order plane wave scattering (Eq. 3.25) and travel time modulation (Eq. 3.19) yield identical omnidirectional spectra for the cases tested here when the following is considered: for monochromatic acoustic plane waves scattered from a frozen, monochromatic surface ($kh \sin\theta \ll 1$), the scattered acoustic field is spatially phase-modulated. For a perfectly sinusoidal surface then, amplitudes of the scattered wave fronts can be expected to take a form similar to the sideband amplitudes in Eq. 3.14. Thus, when linear dispersion of ocean surface waves (Eq. 3.2) and time dependence are submitted in this simple test case, the omnidirectional spectrum, which will include plane waves at all spatially scattered angles, will be identical to that of a signal whose phase is modulated temporally as in Eq. 3.19. The obvious difference between these two models then is that, whereas spatial scattering predicts Doppler shift only in the non-specular contributions to the total pressure field, temporal phase modulation predicts no redirection of acoustic energy in space. So while the simplified phase modulation model is useful for replicating many of the features observed in the received narrowband acoustic field, it clearly does not capture all of the physics of higher order scattering.

While the phase modulation model outlined in Sect. 3.3.2 has been used with some success in reproducing some features of observed spectra (e.g. Figs. 3.2 and 3.12), the implementation here is quite basic, and there are several possible modifications that could render it more accurate and efficient. The results in Fig. 3.17 demonstrate that phase modulation due to multiple surface interactions gives rise to significant frequency-shifted sidebands in the received spectrum, despite randomization of phase of the surface wave at each surface reflection site. The results in Fig. 3.17 (gray dashed trace) were computed as an ensemble average. The phase modulation model described in Sect. 3.3.2 might be implemented in ways other than the ray-based approach presented here. A normal mode-based model, which allows for acoustic full wave field effects to be included, rather than the ray-based approach used here, might be used, where compression and elongation of eigenrays (Eq. 3.8) translates to time-dependent fluctuations of the horizontal eigennumber associated with the normal modes. This modification would be an extension to a perturbational approach such one following Harper and Labianca[HL75a], thereby incorporating both scattering and reflecting mechanisms into the surface wave Doppler shifted acoustic field. However, the ray-based approach has the advantage of providing a simple, intuitive picture of the propagation of an acoustic wavetrain through a changing ocean waveguide. Difficulties arise in any of these modeling approaches for waves that are sufficiently large to introduce caustics, as seen by Preisig and Deane [PD04] and Tindle and Deane [TD05].

Since the Doppler shift is a velocity-dependent phenomenon, it is somewhat surprising not to see some functional dependence on surface wave frequency in the formulation for the amplitude parameter β (Eq. 3.20), given that linear surface wave orbital velocities are a function of surface wave amplitude and frequency. Since higher frequency waves result in higher velocity amplitudes of the harmonic motions at the surface, one could expect a larger frequency shift, or a broader frequency smearing from a higher frequency wave than a lower frequency wave, if the two wave components are of the same amplitude in height. Had shorter FFT's been used to compute the acoustic spectra, the low-frequency surface waves would not be resolved from the narrow peak of the carrier frequency. In effect, a frequency "smearing" would be observed. So the redistribution of the received tone's energy into sidebands is consistent in that the larger separation of the well resolved, high frequency surface wave in the modulated acoustic spectrum would result in a broader convolved main peak, especially since large surface waves (higher amplitude modulation) lead to higher levels in the higher order sidebands. These traits arise from the formulations of harmonic surface waves' influence on received acoustic tones – the phenomena here differ from the Doppler shift arising from a ship-towed source in the functional formulation of the motions, as well as the data processing treatment.

On a final note, the waveguide in this study is modeled as iso-speed, in accordance with CTD measurements (see Sect. 3.4). In general, the propagation environment has a large influence on the measure of phase modulation's effect on the received signal. In a downward refracting environment, for example, the angles of incidence of those rays interacting with the surface would be shallower, which would result in a smaller value of β, and would likely bring it into a range where the first several Bessel functions are quite small. Some rays may not interact with the surface at all, if the vertical sound speed gradient is sufficiently large. In effect, downward refraction would decrease the impact of phase modulation by reflection off the wavy surface. However, from Eqs. 3.9 and 3.11, it is possible for ocean surface waves (or other time-dependent currents) to induce a Doppler shift on a propagating acoustic signal without any interaction with the upper boundary or any other scattering or reflecting. Time dependence of the flow of the medium (and therefore the effective sound speed) results in a non-zero $O(\frac{1}{c^2})$ term in the definition of temporal frequency (Eq. 3.11). Thus, if eigenray endpoints s_1 and s_2 are stationary (in this work, if no surface wave exists, or no interaction with the surface, and source and receivers remain stationary), then the $\frac{ds_{(1,2)}}{dt}$ terms in Eq. 3.11 are zero, but time-varying motions of the medium along the path ($\frac{\partial \boldsymbol{v}}{\partial t}$ in Eq. 3.10) still result in a temporal phase-dependence, i.e. a frequency shift. Since this effect is second order with respect to the slowness c_{snd}^{-1} (Eq. 3.11), the result will be approximately 32 dB below any other motion effects (for a sound speed of $1500\,\mathrm{m\,s^{-1}}$), and so it has been neglected here. It could however prove relevant for deep water, where no interaction with the heaving, pressure-release surface occurs, but where signals propagate for hundreds or thousands of kilometers through a dynamic medium, or with atmospheric studies, where the ratio of the magnitude of flow velocity to sound speed (the Mach number) can be much larger. A laboratory setting where source and receiver configuration could be more easily manipulated would be quite useful for investigating the ideas explored in this paper, particularly with respect to distinguishing the Doppler shift in the scattered and non-scattered field contributions, and with respect to volumetric phase distortions caused by time-dependent flows such as surface gravity waves.

3.8 Conclusions

Measurements of acoustic tones transmitted through a waveguide with a rough, moving surface show clear evidence of Bragg-scattered, Doppler-shifted sidebands as predicted by first order perturbational theory. Surface waves are also seen to lead to higher order sidebands in received spectra of narrowband acoustic tones. While higher order perturbation theory can predict such sidebands, the prevailing surface wave conditions and measured directional spectra suggest that multiple interactions of the acoustic field with the moving surface are also an important part of the distortion mechanism. Phase modulation by specular reflection off a heaving, pressure-release boundary is explored as a simplification of this mechanism, and implemented as a model to explain these measurements. This model shows good agreement with the measured data. The phase modulation model is compared to a development of higher order perturbation theory, and it is found that they agree identically for a simple test case. Phase modulation then helps explain the observations in smaller surface wave conditions, where scattering by a rough surface is less prevalent, and multiple interactions with the surface likely play a much larger role in the distortion of the propagating signals.

This chapter was submitted for publication in the Journal of the Acoustical Society of America in July 2008. The title of the submitted manuscript is “Temporal variability of narrowband tones in a very shallow coastal waveguide”, and the authors are Stephen D. Lynch, Gerald L. D’Spain and Michael J. Buckingham.

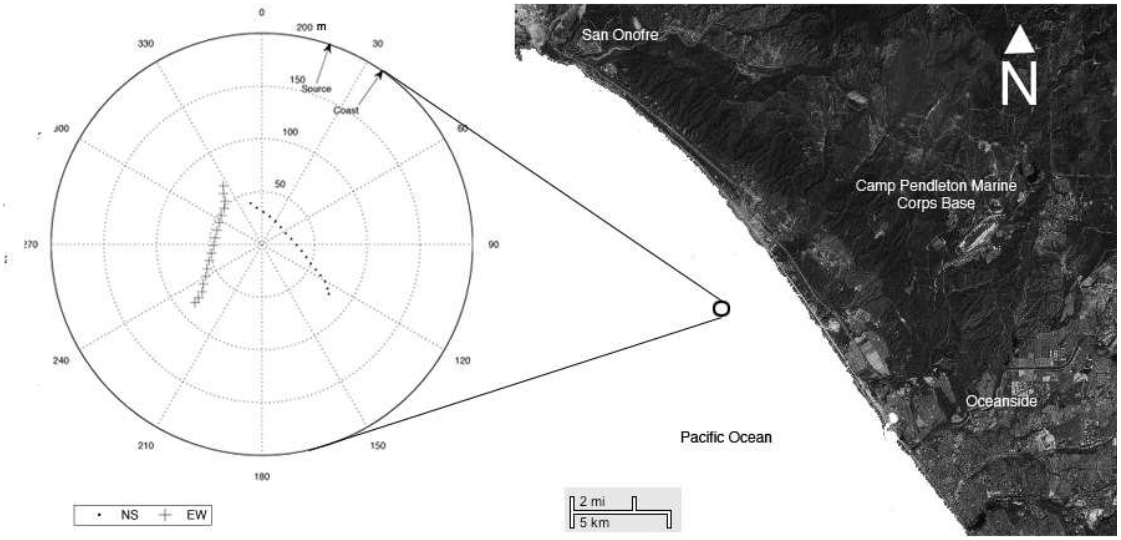

Figure 3.9: The coast at Camp Pendleton where the experiment (marked by the small circle) was conducted. The "broadside" (.) and "endfire" (+) arrays (sparsely illustrated) were deployed nearly orthogonal to each other on the sea bottom just outside the surf zone. The San Clemente Pier, where the directional surface wave measurement network maintained by the Coastal Data Information Program was located, is just off the upper left edge of the photograph.

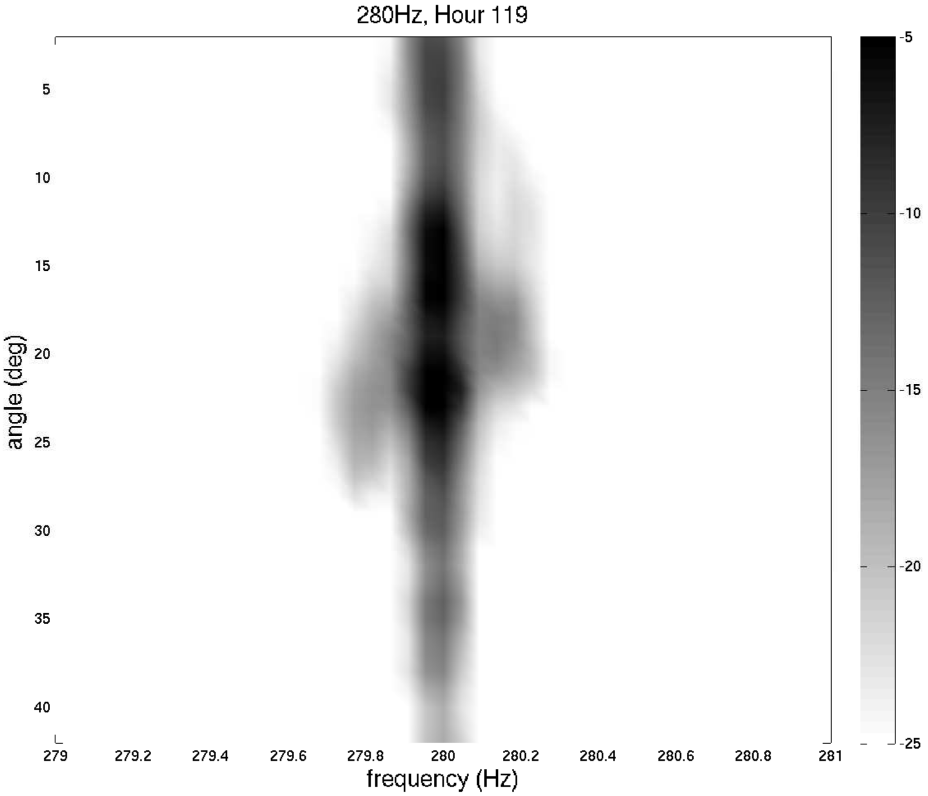

Figure 3.10: Azimuthal dependence of Doppler-shifted acoustic spectrum suggesting Bragg scattering at 280 Hz. The directional spectra (dB) are computed using data from the broadside array, and are normalized to the peak located in the direction of the source.

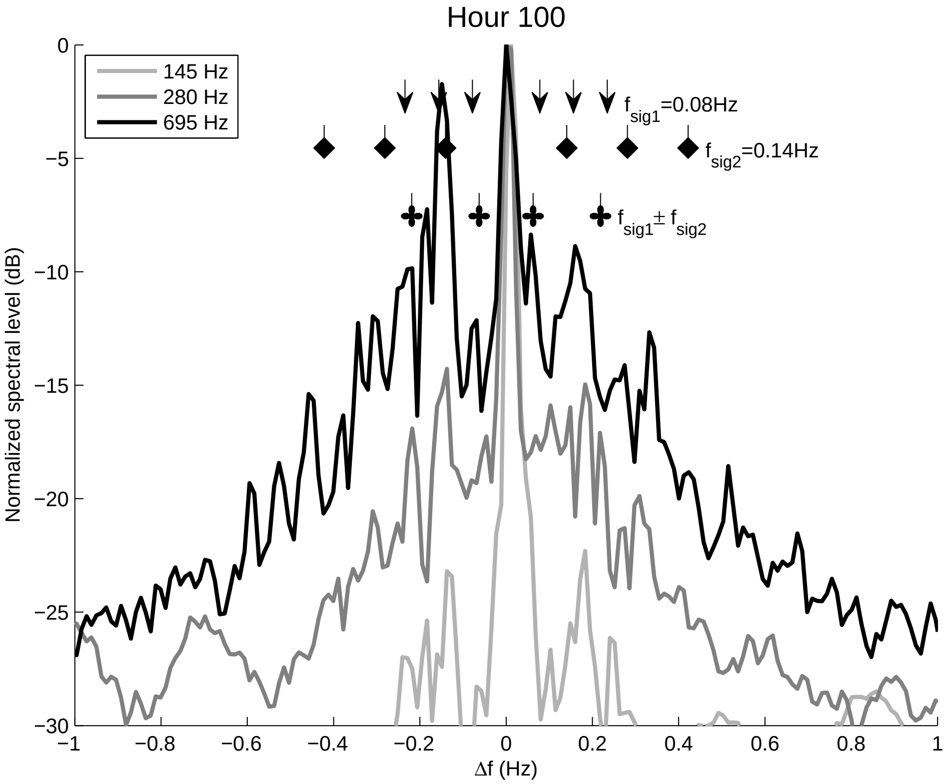

Figure 3.11: Omnidirectional acoustic spectrum measured while two distinct ocean surface wave systems ($H_s = 0.7$m) were present. Arrows and diamonds show locations of the individual peak frequencies along the frequency displacement (horizontal) axis, and roses indicate the sum and difference frequencies centered about the carrier frequencies of the CW transmissions.

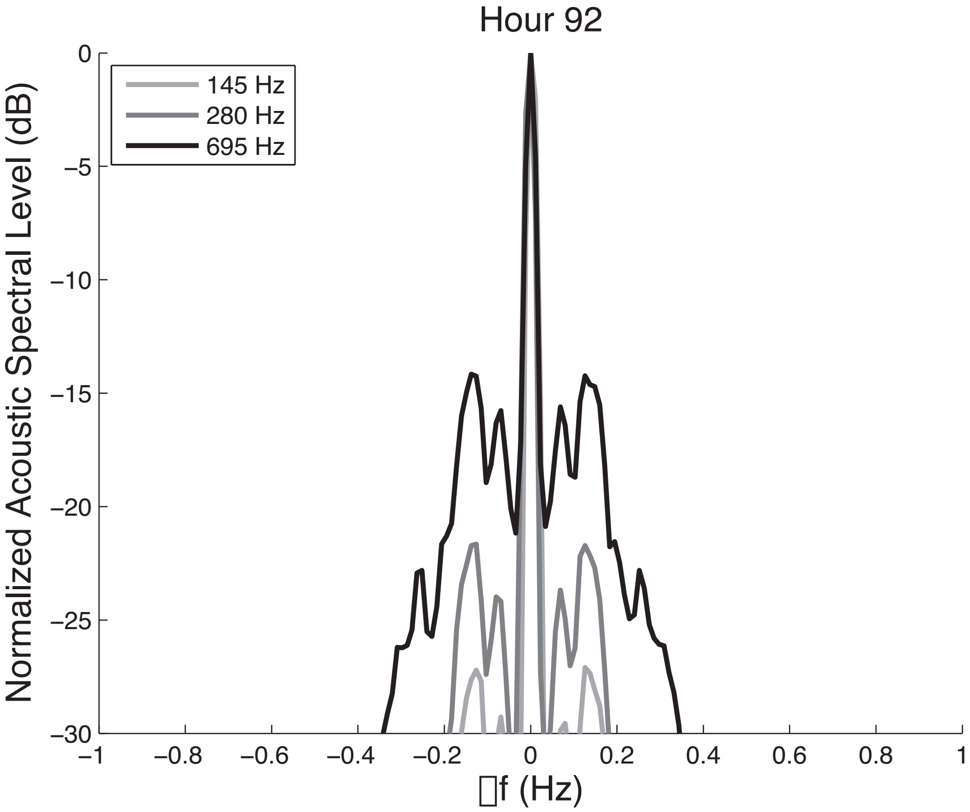

Figure 3.12: Results of the path length modulation model, using the surface waves recorded at hour 92 dominated by wind swell (Fig. 3.1, light gray trace) as the modulating function and a multi-path acoustic environment based on the experiment setting.

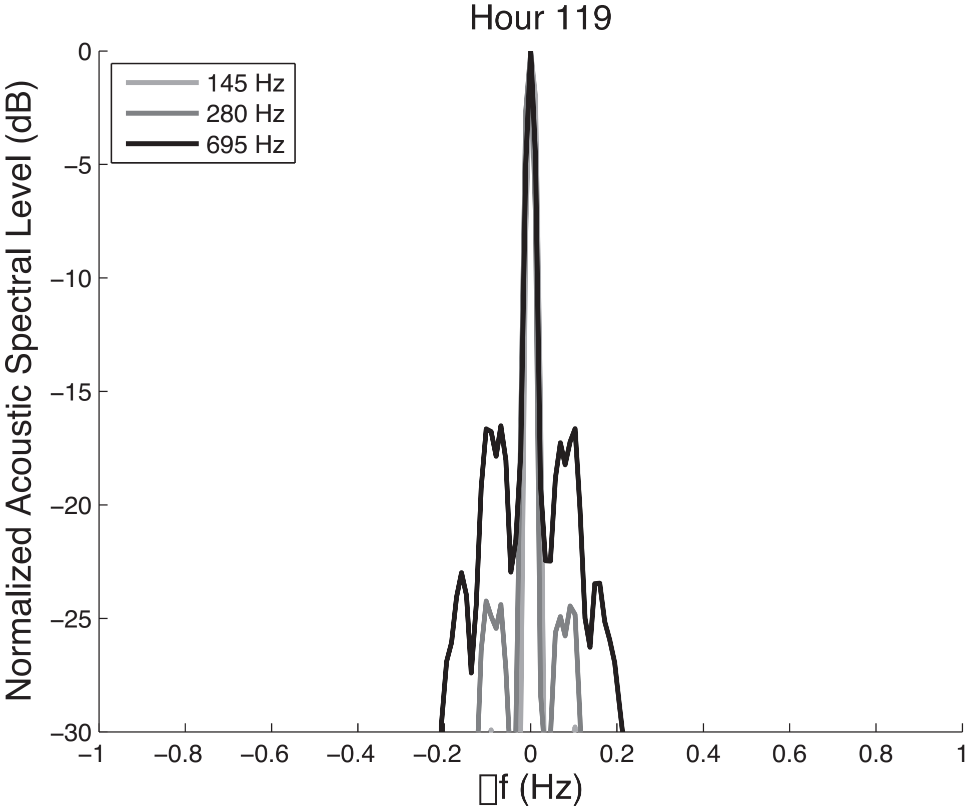

Figure 3.13: Results of the path length modulation model, using the surface waves recorded at hour 119 with only groundswell present (Fig. 3.1, black trace) as the modulating function and a multi-path acoustic environment based on the experiment setting.

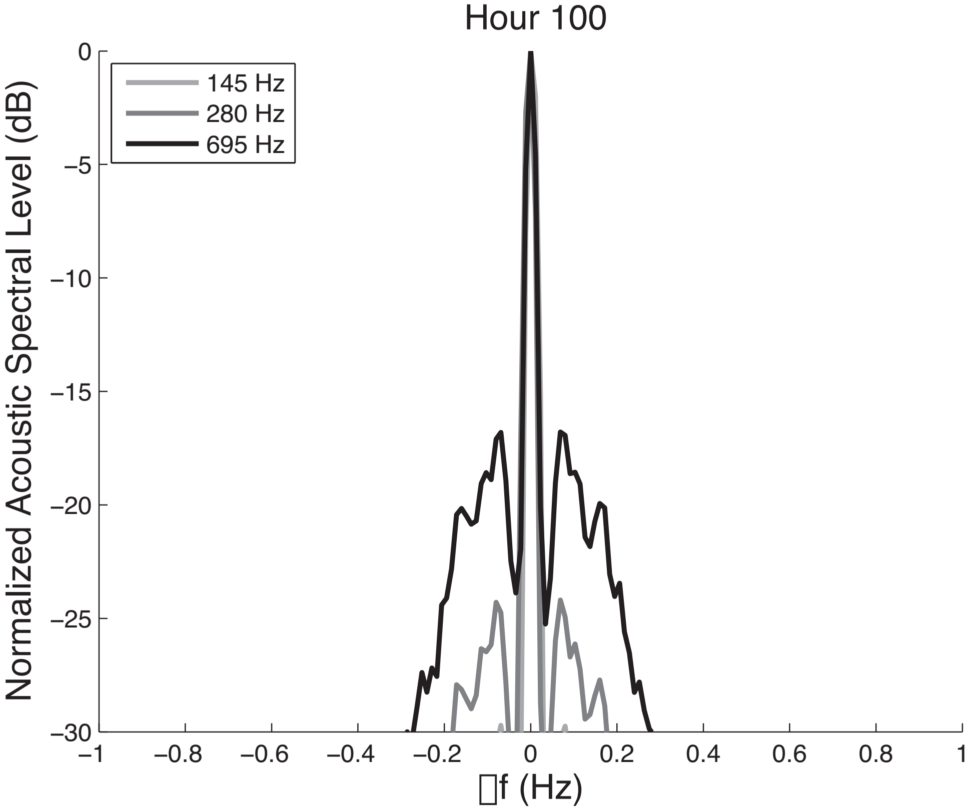

Figure 3.14: Results of the path length modulation model, using the surface waves recorded at hour 100 with both wind swell and groundswell present (Fig. 3.1, medium-gray trace) and a multi-path acoustic environment based on the experiment setting.

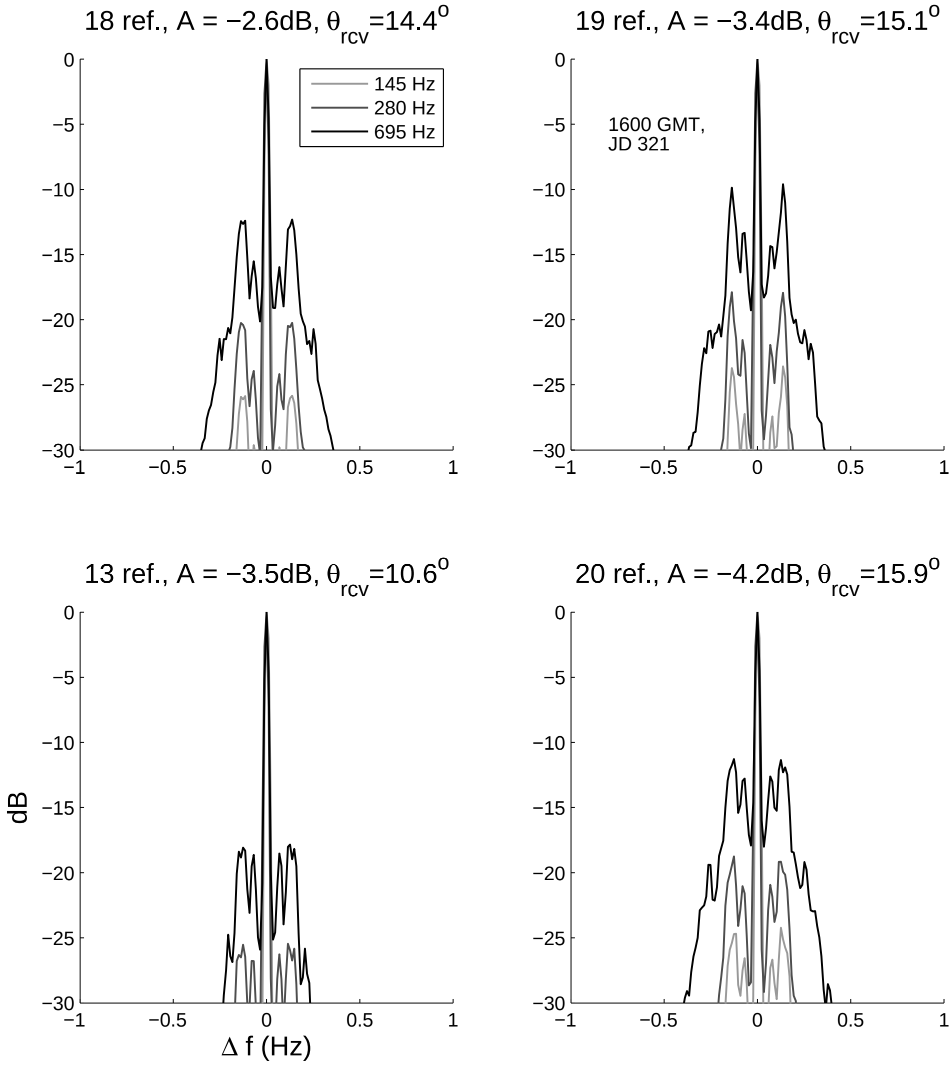

Figure 3.15: Modeled modulation results for individual eigenrays using the surface wave spectrum at hour 92 during the experiment.

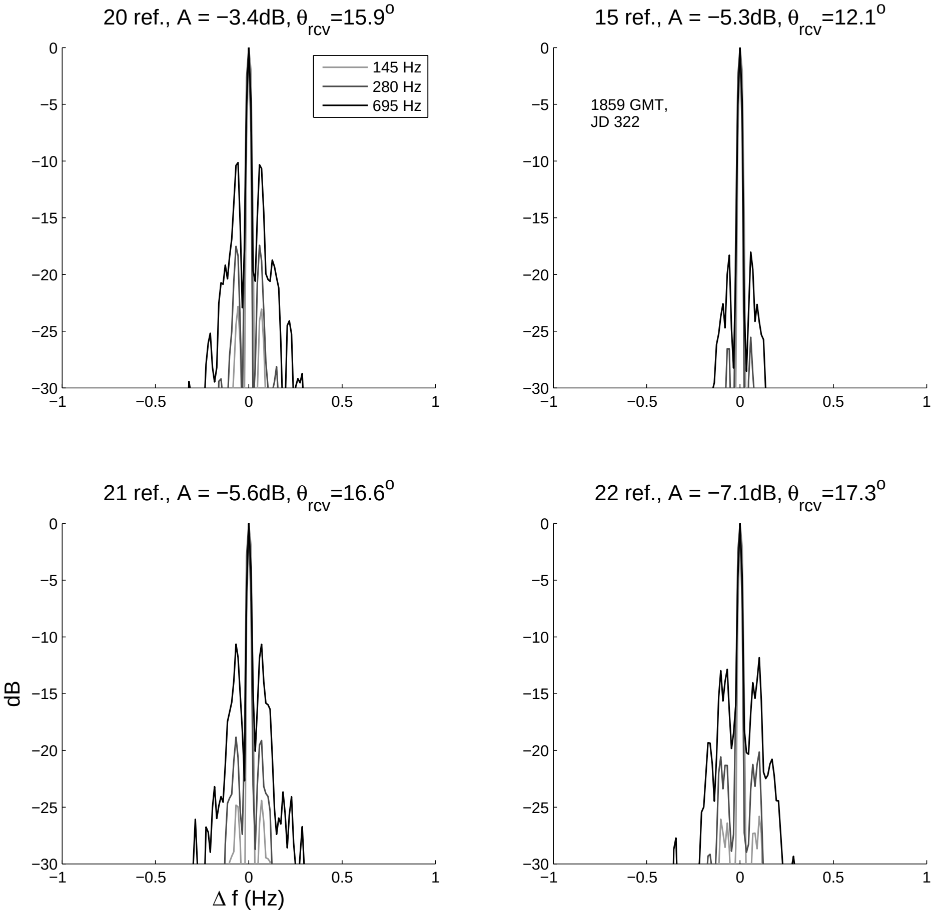

Figure 3.16: Modeled modulation results for individual eigenrays using the surface wave spectrum at hour 119 during the experiment.

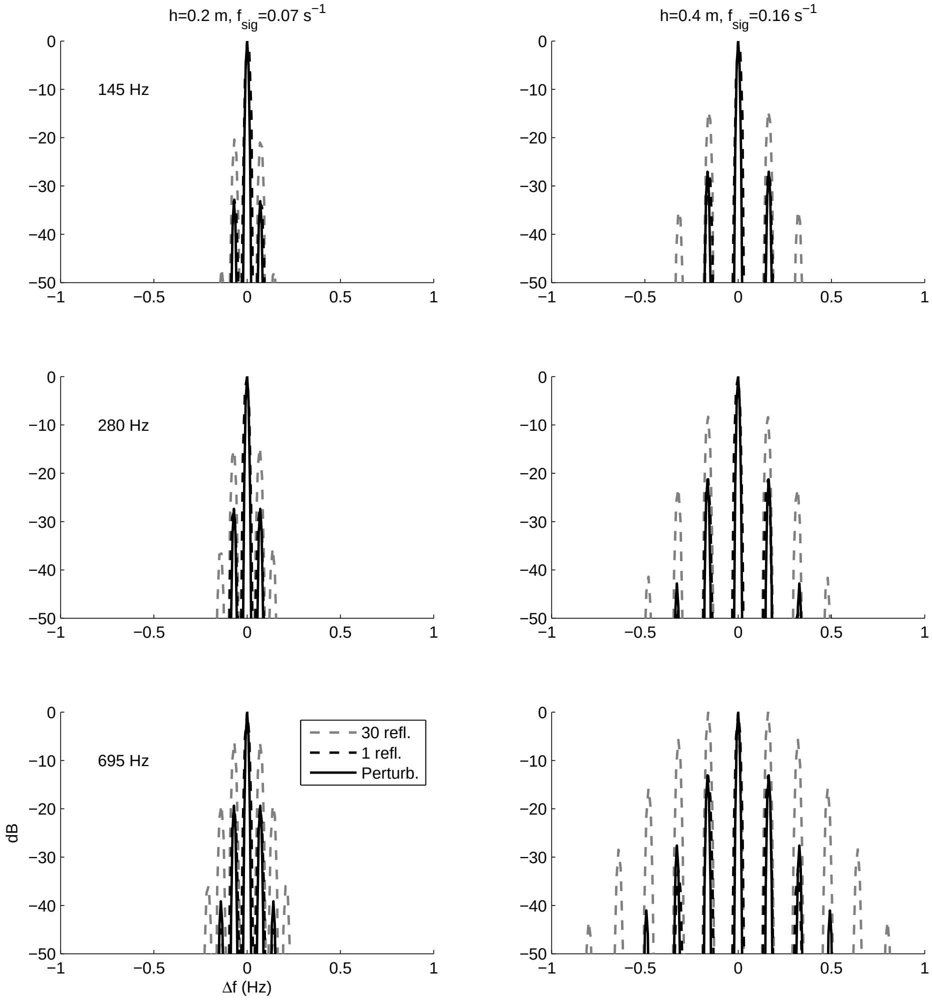

Figure 3.17: Phase modulation is compared to higher order ($(kh)^n$, $0 \leq n \leq 4$) perturbational scattering for two cases of narrowband surface waves with RMS wave heights and frequencies similar to those observed during the experiment. The three rows of plots correspond to the same three frequencies used in other models and in the data produced in this paper.

Chapter 4

Conclusions

Measurement of low-frequency, narrowband acoustic tones propagating through a shallow ocean waveguide show strong dependence on the prevailing surface wave conditions. Examination of the Doppler-shifted Bragg scattering in the vertical plane connecting the source and receiving array clearly illustrates acoustic mode-dependence of the scattered field. Angle and frequency deviations of the scattered acoustic arrivals depend on all spectral and directional components of the measured directional surface wave spectrum. Predictions of angles of arrival for scattered acoustic modes given a directional surface wave spectrum from a physics-based model agree well with measurements.

Evidence of Doppler-shifted Bragg scattering also is seen in the horizontal plane, with angle and frequency deviations corresponding to those predicted by first-order perturbation theory, given the measured directional surface wave field. The frequency offsets, and measured angles of arrival of these azimuthally scattered sidebands agree with predictions from perturbation theory. In addition, when omnidirectional spectra are examined carefully, higher-order, Doppler-shifted sidebands are observed, indicating higher order scattering. However, higher order sidebands persisted at times when the ocean surface waves weakened, contradicting predictions of higher order perturbation theory with a single surface interaction. Thus, multiple interactions with the rough moving surface are shown to have a strong influence on the received acoustic field, resulting in higher order sidebands in omnidirectional spectra. A simplification of higher order scattering with multiple surface interactions agrees well with measured omnidirectional spectra.

The studies in this thesis quantitatively compare experimental observations with model predictions of spatial and temporal frequency deviations caused by acoustic interaction with a rough moving ocean surface. The results are presented in a manner that coincides with the 2-dimensional numerical and theoretical approaches that appear in the literature, while also showcasing the effect of multipath acoustic interaction with an ocean surface wave field that is diverse in both frequency and directional content. The data results presented herein show clear and remarkable dependence of received acoustic spectra on surface wave conditions. Possibilities are opened to allow for the inversion of surface wave conditions, including the directional spectrum, from low frequency acoustic measurements.

4.1 Future work

In the development of this work several topics arose that warrant considerable attention and effort but that did not fit within the scope of this study. During the effort to model narrowband vertical beamformer output, the question of mode correlation arises. In an ideal multi-path environment, individual modes remain correlated, since they are all created by the same source. However, this is not what is observed in this study. Thus, in order to model the mutlipath, a model covariance matrix is computed as the sum of individual covariance matrices corresponding to the individual modes, such that the rank of the covariance matrix is equal to the number of modes (before noise is added). This practice is often employed in beamforming simulations involving source(s) and uncorrelated interferers. An interesting area to pursue would then be an investigation, supported by oceanographic and acoustic data, of the dependence of mode correlation on various ocean parameters.

When confidence intervals are assigned to an estimate from measured quantities, assumptions are often implicitly made about the nature of the data being recorded and analyzed, and about the underlying processes sampled in those recordings. For example, when acoustic spectral estimates are computed, it is most often assumed that the spectral density is a χ^2-distributed random variable, and the variance of the estimate of that quantity will depend on the number of degrees of freedom. However, given the strong influence of ocean surface waves on received spectra of narrowband acoustic tones, it may be also that the statistics of the resulting spectrum deviate from the assumed Gaussian distribution. In fact, in this study, it was observed that the variance of the Doppler-shifted sidebands of the received narrowband tones, when computed numerically from individual the contributions to the incoherently averaged spectra, exhibited strong dependence on the prevailing ocean surface waves. An investigation into the dependence of the statistics of spectral estimation on oceanographic conditions would be a worthwhile pursuit.

While this study has served to strengthen the connection between observed phenomena in the ocean and numerical and theoretical predictions in acoustical interaction with a rough, moving surface, there is still much more to be investigated, for which new experiments may be necessary. Especially in shallow water environments where a propagating field interacts with the surface extensively, it is not clear what higher order effects multiple interactions of an acoustic field with a rough moving surface may have on the directional character of the received acoustic field. Also, it may not always be clear when higher order perturbation theory alone will suffice to describe the received acoustic field, particularly when the effects of multiple interactions on higher order pertrubation theory predictions are included. While this work has made progress in identifying these situations, primarily by developing and testing new modeling approaches with real ocean data, some of the aspects of the waveguide environment that create this type of higher sideband variability in the received field still must be studied before these phenomena can be quantitatively and reliably predicted. An experiment similar to the 1996 shallow water experiment previously discussed, but with some key additions, would be an excellent platform for pursuing these questions further. Use of hydrophone arrays with broad aperture in two spatial dimensions would be a necessary component in further study. However, one important way in which a future study should differ would be to record the data on the arrays using a single computer, or otherwise sample all hydrophone elements simultaneously. In order to help distinguish higher order scattering from multiple interactions with the rough surface, a decomposition of the measured acoustic field into frequency and 3-dimensional wavenumber vector space would lend insight into the differences between these two effects, and a hydrophone array that has large spatial aperture in two dimensions and whose data are recorded simultaneously everywhere will greatly facilitate endeavor.

Additionally, in order to distinguish higher order perturbation with a single interaction from multiple interactions of the propagating acoustic field with the rough, moving ocean surface, further ocean surface wave measurements will be of central importance. Because of the apparent dependence of the relative importance of these effects on the received acoustic field on the spatial coherence of the surface roughness, multiple measurements of the directional surface wave field in the vicinity of the acoustic source and hydrophones will be necessary for further understanding of the phenomena observed in this study and discussed in Chapter 3. While the type of measurements offered by a PADS system (Chapter 1) over the entire experiment vicinity would be ideal, such dense coverage on the spatial scales (~ 1 km) an ocean experiment would require is far from practical. However, a PUV sensor located both near the acoustic source and hydrophone arrays would be an improvement, and any additional such measurements in the area would only further enhance the investigation.

It was also observed in the course of this study that ocean conditions changed rapidly enough that 5-minute recordings that were more than an hour apart could not be used together in data processing, and it is for this reason that temporal resolution was sacrificed for spatial resolution – the assumption of ergodicity was not valid in these cases. Thus, another important difference between the 1996 experiment and one implemented for future study should be transmission of narrowband tones for longer durations, or continuously throughout the period of study. Continuous transmission of narrowband tones would allow for data processing that is truly high resolution and smooth in time, without worry of algorithm instabilities, and indeed the dependence of received, scattered and non-scattered acoustic fields on ocean conditions can be observed as those conditions evolve.

Bibliography

[BGSH02] Michael J. Buckingham, Eric M. Giddens, Fernando Simonet, and Thomas R. Hahn. Propeller noise from a light aircraft for low-frequency measurements of the speed of sound in a marine sediment. *Journal of Computational Acoustics*, 10:445 – 464, 2002.

[BT97] Shira Lynn Broschat and Eric I. Thorsos. An investigation of the small slope approximation for scattering from rough surfaces. part ii. numerical studies. *Journal of the Acoustical Society of America*, 101:2615 – 2625, 1997.

[Chu78] S.D. Chuprov. Relationship between the spectrum of a signal reflected from a rough sea surface and the sea-wave spectrum in the case of small surface roughness. *Soviet Physics Acoustics*, 24:62–67, Jan-Feb 1978.

[Col78] William A. Coles. Interplanetary scintillation. *Space Science Reviews*, 21:411–425, 1978.

[CZO87] Henry Cox, Robert M. Zeskind, and Mark M. Owen. Robust adaptive beamforming. *IEEE Transactions on Acoustics, Speech and Signal Processing*, ASSP-35:1365 – 1376, 1987.

[Dah96] Peter H. Dahl. On the spatial coherence and angular spreading of sound forward scattered from the sea surface: Measurements and interpretive model. *Journal of the Acoustical Society of America*, 100:748–758, Aug 1996.

[Det] Naval Research Laboratory Underwater Sound Reference Detachment. Usrd transducer catalog.

[DF98] Daniela DiIorio and David M. Farmer. Separation of current and sound speed in the effective refractive index for a turbulent environment using reciprocal acoustic transmission. *Journal of the Acoustical Society of America*, 103:321 – 329, 1998.

[DTC+06] Gerald L. D'Spain, Eric Terrill, C. David Chadwell, Jerome A. Smith, and Stephen D. Lynch. Active control of passive acoustic fields: Passive synthetic aperture/doppler beamforming with data from an autonomous vehicle. *Journal of the Acoustical Society of America*, 120(6):3635–3654, Dec 2006.

[EG04] Tano Mikhael Elfouhaily and Charles-Antoine Guerin. A critical survey of approximate scatering wave theories from random rough surfaces. *Waves in Random and Complex Media*, 14:R1 – R40, 2004.

[FDV01] D.M. Farmer, Grant B. Deane, and S. Vagle. The influence of bubble clouds on acoustic propagation in the surfzone. *IEEE Journal of Ocean Engineering*, 26:113 – 124, 2001.

[For70] Leonard Fortuin. Survey of literature on reflection and scattering of sound waves at the sea surface. *Journal of the Acoustical Society of America*, 47:1209–1228, 1970.

[Gra03] Robert F. Gragg. Doppler sidebands in the crosss-spectral density of narrow-band reverberation from a dynamic sea surface. *Journal of the Acoustical Society of America*, 114:1387–1394, 2003.

[Har78] Fredric J. Harris. On the use of windows for harmonic analysis with the discrete fourier transform. *Proceedings of the IEEE*, 66:51 – 83, 1978.

[Hay96] Simon Haykin. *Adaptive Filter Theory*. Prentice-Hall, Inc., Upper Saddle River, NJ 07458, 1996.

[HHK01] Paul Hursky, William S. Hodgkiss, and William A. Kuperman. Matched field processing with data-derived modes. *Journal of the Acoustical Society of America*, 109:1355 – 1366, 2001.

[HL75a] E.Y. Harper and F.M. Labianca. Perturbation theory for scattering of sound from a point source by a moving rough surface in the presence of refraction. *Journal of the Acoustical Society of America*, 57:1044–1051, 1975.

[HL75b] E.Y. Harper and F.M. Labianca. Scattering of sound from a point source by a rough surface progressing over an isovelocity ocean. *Journal of the Acoustical Society of America*, 58:349–364, Aug 1975.

[JD90] Johnson and Dudgeon. *Array Signal Processing*. ???, 1990.

[JKPS94] Finn B. Jensen, William A. Kuperman, Michael B. Porter, and Henrik Schmidt. *Computational Ocean Acoustics*. AIP Press, Woodbury, NY, 1994.

[Kor53] E.T. Kornhauser. Ray theory for moving fluids. *Journal of the Acoustical Society of America*, 25:945 – 949, 1953.

[LBD08] Stephen D. Lynch, Michael J. Buckingham, and Gerald L. D'Spain. Temporal variability of narrowband tones in a very shallow coastal waveguide. *Journal of the Acoustical Society of America*, page submitted, 2008.

[Lig78] James Lighthill. *Waves in Fluids*. Cambridge University Press, Cambridge, UK, 1978.

[LS96] Kevin LePage and Henrik Schmidt. Analysis of spatial reverberation statistics in the central arctic. *Journal of the Acoustical Society of America*, 99:2033 – 2047, 1996.

[LS04] A.V. Lebedev and B.M. Salin. Effects of localization of the areas of sound scattering by surface wind waves. *Acoustical Physics*, 50(6):704–716, Oct 2004.

[Mar63] H.W. Marsh. 'doppler' of boundary reverberation. *Journal of the Acoustical Society of America*, 35:1836, 1963.

[McA02] Katherine Megan McArthur. *Geoacoustic inversion in a very shallow water environment.* PhD thesis, Scripps Institution of Oceanography, UCSD La Jolla, CA 92093, 2002.

[McD92] Susanne T. McDaniel. High frequency forward scattering in a refracting ocean. *Journal of the Acoustical Society of America*, 92:324–331, Jul 1992.

[MF53] Philip M. Morse and Herman Feshbach. *Methods of Theoretical Physics, Part I.* McGraw-Hill, New York, 1953.

[MHDC03] David A. Miles, Robin N. Hewitt, Marcus K. Donnelly, and Timothy Clarke. Forward scattering of pulses from a rough sea surface by fourier synthesis of parabolic equation solutions. *Journal of the Acoustical Society of America*, 114:1266–1280, 2003.

[MWW95] Walter Munk, Peter Worcester, and Carl Wunsch. *Ocean Acoustic Tomography.* Cambridge University Press, Cambridge, 1995.

[Ogi87] J.A. Ogilvy. Wave scattering from rough surfaces. *Reports on Progress in Physics*, 50:1553 – 1608, 1987.

[OS99] Alan V. Ooppenheim and Ronald W. Schafer. *Discrete-Time Signal Processing.* Prentice Hall, Upper Saddle River, New Jersey 07458, 1999.

[Par71] B.E. Parkins. Reflection and scattering from a time-varying rough surface – the nearly complete lloyd's morror effect. *Journal of the Acoustical Society of America*, 49:1484–1490, May 1971.

[PD04] James C. Preisig and Grant B. Deane. Surface wave focusing and acoustic communications in the surf zone. *Journal of the Acoustical Society of America*, 116:2067–2080, Oct 2004.

[Pin08] Robert Pinkel. Advection, phase distortion, and the frequency spectrum of finescale fields in the sea. *Journal of Physical Oceanography*, 38:291 – 313, 2008.

[PN78] John Preston and Richard Nisley. Simple frequency modulation model for surface reflection of a cw tone. *Journal of the Acoustical Society of America*, 64:601 – 604, 1978.

[PW91] M. Pourkaviani and J.F. Willemsen. Perturbative corrections to acoustic doppler backscattering i.: Ocean surface gravity waves. *Journal of the Acoustical Society of America*, 90:426–432, 1991.

[Ros99] Allan P. Rosenberg. A new rough surface parabolic equation program for computing low-frequency acoustic forward scattering from the ocean surface. *Journal of the Acoustical Society of America*, 105:144–153, 1999.

[Sal98] Richard Salmon. *Lectures on Geophysical Fluid Dynamics*. Oxford University Press, New York, NY, 1998.

[SK94] Henrik Schmidt and William A. Kuperman. Spectral and modal representations of the doppler-shifted field in ocean waveguides. *Journal of the Acoustical Society of America*, 96:386 – 395, 1994.

[Smi02] Jerome A. Smith. Continuous time-space sampling of near-surface velocities using sound. *Journal of Atmospheric and Oceanic Technologies*, 19:1860–1872, 2002.

[Smi08] Jerome A. Smith. Vorticity and divergence of surface velocities near shore. *Journal of Physical Oceanography*, 38:1450–1468, 2008.

[TB95] Eric I. Thorsos and Shira Lynn Broschat. An investigation of the small slope approximation for scattering from rough surfaces. part i. theory. *Journal of the Acoustical Society of America*, 97:2082–2093, 1995.

[TD05] Chris T. Tindle and Grant B. Deane. Shallow water sound propagation with surface waves. *Journal of the Acoustical Society of America*, pages 2783–2794, May 2005.

[Uri83] Robert J. Urick. *Principles of Underwater Sound.* McGraw-Hill, 1983.

[VT98] G. Voulgaris and J.H. Trowbridge. Evaluation of acoustic doppler velocimeter (adv) for turbulence measurements. *Journal of Atmospheric and Oceanic Technology*, 15:272 – 289, 1998.

[Wil73] Robert G. Williams. Estimating ocean wind wave spectra by means of underwater sound. *Journal of the Acoustical Society of America*, 53:910–920, Mar 1973.

[WJ93] Michael Wild and Robert Joyce. Three-dimensional modeling of narrow-band pulse spreading using normal modes. *Journal of the Acoustical Society of America*, 94:2303–2306, 1993.

[WJ95] Michael Wild and Robert Joyce. Modeling the spatial and frequency distribution of narrow-band acoustic signals scattering from the ocean surface. *Journal of the Acoustical Society of America*, 97:1559–1565, 1995.

[WK96] Henry Weinberg and Ruth Eta Keenan. Gaussian ray bundles for modeling high-frequency propagation loss under shallow-water conditions. *Journal of the Acoustical Society of America*, 100:1421–1431, 1996.

[WRK07] Shane Walker, Phillipe Roux, and William A. Kuperman. Modal doppler theory of an arbitrarily accelerating continuous-wave source applied to mode extraction in the oceanic waveguide. *Journal of the Acoustical Society of America*, 122:1426 – 1439, 2007.

[WYS99] L. Whitcomb, D. Yoerger, and H. Singh. Advances in doppler-based navigation of underwater robotic vehicles. *Proceedings of the 1999 IEEE International Conference on Robotics & Automation*, pages 399 – 406, May 1999.

[Zie95] Rodger E. Ziemer. *Principles of communications : systems, modulation, and noise.* John Wiley and Sons, New York, NY, 1995.